Intracavity Spatial Filtering in Broad Area Semiconductor Laser

---

A thesis submitted for the degree of Doctor of Philosophy in Computational and Applied Physics of

Sandeep Babu Gawali

Directors

Dr. Kestutis Staliunas

Dr. Jose Trull

Departament de Física

Terrassa, October 2020

Acknowledgments

First, I would like to express my sincere appreciation to my PhD supervisors Prof. Kestutis Staliunas and Prof. Jose Trull for their guidance and support throughout my entire PhD journey. I got constant encouragement from both of them. Their valuable ideas and suggestions lead to successful completion of this thesis.

I am also grateful to Prof. Ramon Herrero, Crina Cojocaru, Muriel Botey, Cristina Masoller, Antonio Pons, and Ramon Vilaseca from the DONLL group for their valuable suggestions and support.

I would like to also thank my co-worker Jordi, Carlos, Dario, Maria, Pablo, Judith, Hossam, Donatus, Ricardo, Laura, Salim, and Tetsu from DONLL group. We shared good memories during lunchtime and all other events of the group.

I am also thankful to Guillermo and Joan from Monocrom for providing me the laser diode and necessary help during this PhD thesis.

I appreciate the efforts of Darius and Vytautas from Femtika, Lithuania for fabricating the photonic crystal samples and providing me on time. I am grateful to them.

I would like to express my gratitude to my parents and my sisters for their love and encouragement during these years.

I express deep gratitude to my wife Swati for her endless support, love, and patience. This thesis would not have been possible without her support.

Finally, I acknowledge the funding through EUROSTARS project HIP Lasers (E-10524).

Table of Contents

Preface

The first theoretical foundation of LASER was laid by Albert Einstein in the year 1916 in his paper “On the Quantum Theory of Radiation” and the first device operating in the optical range was technically realized, almost after 50 years, by Theodore Maiman using a ruby crystal pumped by flash lamps. Soon after this successful demonstration, people recognized the potential of this tool, leading to a rapid growth of this field. In 1962 Robert Hall invented the semiconductor injection laser and, in the same year, the first GaAs laser was demonstrated. After that, many researchers reported lasing action in different materials at near infrared wavelengths.

Since the first semiconductor laser demonstration, the field has changed considerably over the years and new laser devices have been developed. Laser diodes are electrically pumped devices having high wall-plug efficiencies of more than 50%, the highest available in the market. Other advantages include their smaller size and cheapest price in terms of watt per dollar. All these advantages make semiconductor lasers a competitive source for many applications. Laser diodes are mainly used in telecommunications, optical storage, material processing, medical, military & defense applications, instrumentation & sensing and for the pumping of solid-state gain media. The laser diode market is dynamic and rapidly developing, with new applications emerging continuously.

One of the first developed semiconductor lasers was the edge-emitting laser in which radiation is coupled out from the cleaved edge of semiconductor junction. The lasers based on GaAs are widely used in the NIR region. Arrays made up of edge emitting broad area laser (BAS) shows a high electro-optical efficiency, high reliability, and can generate high output power. Due to their advantages, this laser has become promising building block for the implementation of high-power diode lasers. However, in high power regime, the broad area edge emitting lasers suffers from low beam quality due to multimode emission along the junction plane. Since the beam quality is a crucial factor for many applications such as fine processing of metal, medical surgery or coupling into low numerical aperture optical fibers, its improvement is a challenging task that is always of potential interest and would open new areas of application using high-power micro-lasers.

Typical emitting apertures of edge emitting broad area lasers have rectangular dimensions of 1 µm in vertical direction (fast axis) and between 50-400 µm in horizontal direction (slow axis). The thickness of the active region layers in the vertical direction is very small and the beam is tightly confined along this direction, diffracting strongly when it emerges from the active region. Typical divergence angles are around 40° (FWHM), but the emission is single mode along this axis and can be efficiently collimated using cylindrical lens. However, in the horizontal axis (slow axis), the beam is dominated by the existence of higher-order transverse modes with complex beam profile. The beam divergence angle is 6-8° (FWHM) but, contrary to fast axis case,

collimation along this direction becomes problematic. Because of unequal emitter dimensions, the beam spreads unequally in both directions and in the far field, the beam quality is degraded with elliptical shape. This fact limits the use of such beam for diffraction-limited applications or when coupling the radiation into single mode optical fiber is required. In high power semiconductor lasers, the beam quality factor along slow axis (M_x^2) can be 100 or even more due to broad area radiation and large divergence angle. The poor beam quality of the emitted radiation is due to the absence of a natural angular selection mechanism in the large aspect ratio cavity of such device.

A lot of work has been done to improve beam quality in edge-emitting broad area lasers. High spatial quality single transverse mode can be obtained by reducing the width of the active region [1], but with reduced output power. The spatial filtering technique in particular for broad-area semiconductor (BAS) laser has been demonstrated in external cavity configuration. The beam quality improvement in diode laser bar with 49 emitters was demonstrated using intracavity slit with off-axis feedback. Using this technique, the beam parameter product improved by factor of 8 [2]. A symmetric double feedback configuration was used to improve the beam quality of broad area laser. In this configuration, the M^2 factor was improved by factor of 12 [3]. In a similar configuration, improvement in the spatial and temporal coherence of broad area laser was achieved using double grating feedback in external cavity design [4]. The beam quality factor (M^2) is improved by factor of 6 using Bragg grating in AR coated laser diode in external cavity configuration [5]. In another study, suppression of the slow-axis divergence angle by factor of 4 was achieved in high-power diode laser bar with external feedback [6]. Numerically, the beam quality improvement was demonstrated by evanescent spatial filtering technique [7]. The beam quality of tapered high-power semiconductor laser diodes is improved by an order of magnitude due to epitaxial layer structures with low modal gain with output power more than 3 W [8]. Numerically, it was also shown that an improvement in the beam quality can be obtained by spatial gain modulation of the active medium[9].

All these methods can improve the beam quality, but each has its own limitations. For example, the external cavity configuration occupies large size and, certainly is not suitable for micro-laser. The ridge waveguide has diffraction-limited beam quality, but with reduced output power. The tapered diode laser demonstrates higher output power with good beam quality, but it suffers from astigmatism. The implementation of spatial gain modulation of the active medium will be technologically challenging. None of these methods is suitable for compact micro-lasers. A high power micro-laser would require compact spatial filter directly integrated between the output facet and the cavity mirror.

In this thesis, we propose a new approach for improving the beam quality for high power BAS lasers. The idea is to use photonic crystals (PhCs) as spatial filters, which will help to miniaturize the size of the device. For high-power lasers, spatial filtering using conventional filter will be problematic due to the large fluence achieved in the

tightly focused beam and the difficulty in placing the bulky lenses in intracavity configuration. The PhC, due to their small size will be attractive solution for a compact system and can fit into the micro optical device or inside the resonator of micro-laser. Compared to conventional spatial filter, PhC will avoid the need of extra space to affect the beam in the far field. In addition, the PhC filter has no physical aperture limitation and no absorption makes it very attractive for high power laser system.

The main objective of the thesis is to demonstrate spatial filtering and improve the beam quality in a BAS laser using PhC. The successful demonstration of such filtering will pave the way for monolithic integration in which the PhC could be integrated directly between the front facet and cavity mirror. The PhC works in the near-field plane, acting as a spatial filter by selectively deflecting the higher angular components of the light beam. We provide in this work the first proof of principle demonstration of spatial filtering in broad area laser using PhC in intracavity configuration. The improvement of the beam spatial quality will be demonstrated, through a reduction of the M^2 factor and an increase of the spatial brightness of the semiconductor laser.

The PhD thesis is organized in seven chapters. First chapter presents an introduction, background, and overview of the basic concepts of semiconductor laser, introducing basic ideas about the lasing action in laser diodes, their structure and emitter types. We also introduce the definitions for beam quality and brightness of a laser beam.

In the second chapter, we discuss about the general properties of photonic crystals (PhC), discussing the basic 1D, 2D and 3D PhC structures and their potential use for frequency or spatial filtering. To outline the motivation of this thesis we will center this introduction mostly to spatial filtering, introducing the difference between Bragg and Laue configurations for the design and fabrication of our PhCs. Finally, we will introduce shortly some concepts about the different types of fabrication processes used to inscribe PhCs.

In the third chapter, we discuss the different methods and measurement techniques used for this thesis, organized in four different independent sections: the fabrication technique used to inscribe the PhC on glass substrate using Bessel beams; the numerical results of single-pass measurement through PhC and its optimization; the numerical model of edge emitting broad area laser developed for comparison with the experimental results and the characterization of the laser beam through the measurement of its beam quality factor (M^2).

In the fourth chapter, we discuss in detail the experimental setup developed for our work, based on an extended cavity configuration, and present the details on the filtering by conventional spatial filtering and in the integrated PhC filtering scheme. The experimental setup of extended cavity and its characterization will be explained and the enhancement of the brightness of the beam using spatial filtering with intracavity slit and PhC will be discussed in the last part of the chapter.

In the fifth chapter, the results of spatial filtering using the intracavity slit and the PhC will be extended by considering the effect of increasing the pump current and the reflectivity of feedback mirror. The results obtained in our experiments will be compared with the numerical model developed in order to check the validity of the model. The numerical model will then be used to search for the numerical optimization of the filtering function to enhance the brightness of the beam allowing to find an optimal configuration of the filtering geometry.

The sixth chapter presents the results obtained used longer cavity length broad area laser. We include some results of the characterization of the system, and present the experimental results of spatial filtering using the intracavity slit and the PhC.

The last chapter summarizes and concludes all the results introducing some discussion on the possible future work.

Chapter 1

Introduction to High Power Diode Laser

The search for new laser types and configurations arises as the demand for high power laser in scientific and industrial applications increases. The first demonstration of lasing action in semiconductors [10-12] took place in 1962 just after 2 years from the invention of the first solid-state laser in ruby crystal pumped by flash lamp [13]. The first semiconductor laser had limited usage, as it could not be operated in continuous wave regime due to thermal issues. Over many years of research in semiconductor field, the performance of this laser was improved in terms of output power and efficiency, leading to a volume production of semiconductor lasers. Actually, there are many lasers available in the high-power regime such as carbon dioxide laser, Nd:YAG or Fiber laser. All these lasers have their own advantages and limitations. The diode lasers offer advantages over other lasers in terms of its small size, low cost and high wall plug efficiency. Due to their advantages, this laser finds application in material processing [14], biomedical applications [15], telecom [16], and pumping solid-state laser [17]. It is also been used in military, surveillance and lighting. In this chapter, we will discuss the physical principles behind the lasing operation in the semiconductor laser, types of emitter configurations, and the determination of beam quality.

1.1 Band structure of Semiconductor laser

When atoms combine to form a solid the sharply defined energy states that we associate with free atoms, such as in a gas, broaden considerably because of the large number of interactions between an atom and its neighbors. The result is a series of broad energy states, called bands. At absolute zero temperature, the empty conduction band and the completely filled valence band are separated by an energy gap, a region of forbidden electronic states of energy E_g.

Those semiconductor materials for which the energy levels at the maximum of the valence band and at the minimum of the conduction band occur at the same value of k, k=0, are called direct band gap semiconductors [18-19]. Figure 1.1 below shows a direct band gap semiconductor with the valence and conduction bands separated by the energy gap (E_g). $E_c(k)$ and $E_v(k)$ represent the electron energies in the conduction band and the valence band respectively.

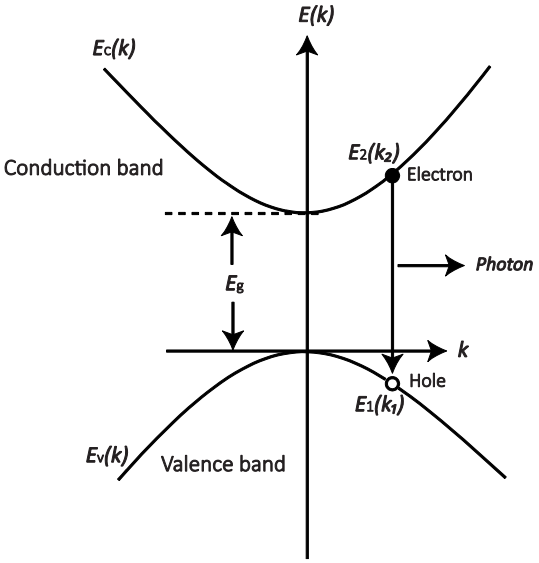

Fig. 1.1: Band structure of semiconductor laser. In a direct bandgap structure the minimum of the conduction band and the maximum of the valence band occur at the same value of k. The conduction band and valence band are separated by energy difference (E_g).

When the semiconductor is pumped with incident light of energy equal or larger than the band gap, the electrons from the valence band can absorb this energy, being promoted to the conduction band and creating, at the same time, a vacancy (hole) in the valence band. The radiative recombination of electron-hole pairs leads to the emission of photons with energy equal or larger than the bandgap energy. For this process, the conservation of energy (E) and momentum $(\hbar k)$ must be satisfied. The radiative transition between the conduction band and valence band results in the emission of photon with energy equal or larger than the value is given by the expression:

$$E_g = h\nu = E_{2c} - E_{1v} \tag{1.1}$$

In semiconductors, the electron energy in the conduction band and in the valence band is given by:

$$E_c(k) = E_g + \frac{\hbar^2\kappa^2}{2m_e} \; and \; E_v(k) = -\frac{\hbar^2\kappa^2}{2m_h} \tag{1.2}$$

Where m_e and m_h are the effective masses of electron and holes, $k = 2\pi/\lambda$, $\hbar$ is reduced Plank's constant and E_g is the energy gap of the material.

If the intra-band non-radiative relaxation processes act very fast, the electrons (holes) can relax to the lowest (highest) energy states within the band leading to an emission at the gap energy. In indirect band gap semiconductors such as Si and Ge, the maximum of the valence band and the minimum of the conduction band occur at different *k* values. In this case, band-to-band recombination is difficult by the fact that momentum conservation requires excitation of a phonon simultaneously to the radiative decay. This fact results in recombination processes occurring mostly by non-radiative relaxation, involving phonon excitations. Indirect band gap materials are not suitable materials for lasing activity [20]. For Si and Ge, the energy gap is 1.1 eV and 0.74 eV respectively.

1.2. Absorption and emission process

The principle of lasing action in semiconductor lasers is identical to that in solid state or gas lasers, involving pumping of the gain medium, creation of a population inversion, and feedback into cavity.

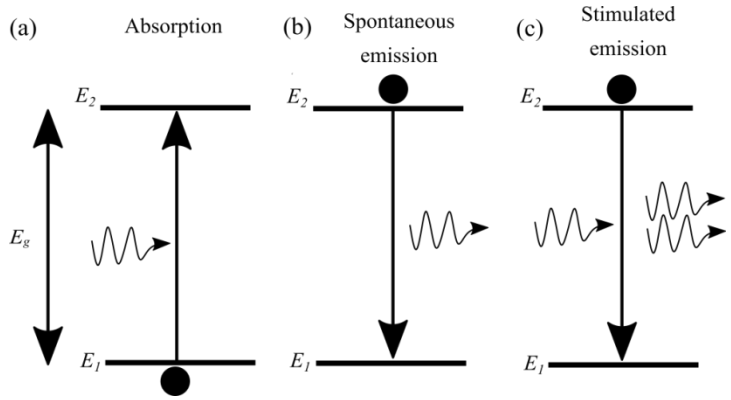

Fig. 1.2: The three basic process of light-matter interaction. (a) Absorption: electron is excited to higher energy state; (b) Spontaneous emission: excited electrons relax back to the ground state releasing a photon. (c) Stimulated emission: the emission of a photon is stimulated by the presence of photons with frequency equal to the transition resonance. The emitted photon is in phase with the cavity photons resulting in coherent emission.

The three basic process through which electromagnetic field interacts with matter are: (1) absorption, (2) spontaneous emission, and (3) stimulated emission. These processes are illustrated in figure 1.2 for a two-level system with energy levels E_1 and E_2 and with respective population densities N_1 and N_2 [21].

Absorption – In this process, an electron in the lower energy state, E_1, absorbs a photon of energy $h\nu = E_2 - E_1$ and jumps to the higher energy state E_2 as illustrated in fig. 1.2 (a). In this process, an electron is transferred to higher energy level. The rate of change of the population levels is given by:

$$\frac{dN_1(t)}{dt} = -B_{12}N_1\rho(\nu) \tag{1.3}$$

Where B_{12} is the Einstein coefficient for absorption and $\rho(\nu)$ is the spectral energy density of the incident radiation.

Spontaneous emission – An electron in the excited state decays spontaneously to the ground state by emitting a photon with energy equal to the difference in energy between the two states. This photon is emitted in a random direction. The rate of change of population in the excited state due to this process is given by:

$$\frac{dN_2(t)}{dt} = -A_{21}N_2(t) \tag{1.4}$$

Where A_{21} is the Einstein coefficient for spontaneous emission and is related with the spontaneous emission lifetime by the relation $\tau = \frac{1}{A_{21}}$. The emission from light emitting diodes (LED) is based on this process.

Stimulated emission – An electron in the excited state, E_2, is induced to make a transition into the ground state, E_1, by the presence of photons of the right frequency in the cavity. The transition from the higher to the lower state produces an additional photon that has the same phase and direction of the incoming photon. The corresponding rate equation is given by:

$$\frac{dN_2(t)}{dt} = -B_{21}N_2\rho(\nu) \tag{1.5}$$

Where B_{21} is the Einstein coefficient for stimulated emission. Light sources based on this emission process are called lasers.

In a real situation, more than two levels are usually involved and the electronic populations are changed through radiative and non-radiative transitions, which may involve relaxation or transitions to other levels. To achieve laser light in the semiconductor material, it is fundamental that the stimulated emission process dominates over the absorption and spontaneous emission. This condition can only be

achieved under population inversion ($N_2 > N_1$) conditions and with the presence of enough photons in the cavity to promote the stimulated emission.

1.3. p-i-n double heterostructure

Laser diodes are fabricated by sandwiching a p-type and an n-type section of the same semiconductor material in metallurgical contact. The p-type has excess number of holes while the n-type has excess number of electrons (majority carriers). In these materials, at room temperature, the charge carriers are in continuous random thermal motion in all directions. When the two sections are put into contact, a number of effects appear: i) Diffusion of the majority carriers takes place, so electrons move into the p-region while holes move into the n-region. The diffused charges recombine with the existing holes or electrons leading to a disruption of the charge balance in the two regions; ii) This creates a narrow region around the junction nearly depleted of mobile charges, leaving a region (depletion layer) with fixed charge; iii) The fixed charge induces a static electric field, pointing from the n-side to the p-side, acting against the electron or hole diffusion motion; iv) The equilibrium condition results in a net built-in potential difference at the junction, with the n-side exhibiting a higher potential than the p-side, resulting in the bending of the energy bands at the junction; v) As a consequence of this voltage difference no net current flows across the junction.

In these lasers, the population inversion condition is achieved by electrical pumping using an injection current through the p-n junction. The injection current promotes electrons and holes into the depletion region leading to photon emission through electron-hole recombination by stimulated emission. The rate of absorption and stimulated emission in the semiconductors depend on quantities such as the incident photon flux spectral intensity, the recombination lifetime of the involved energy levels, the optical joint density of states and the occupancy probabilities for emission and absorption. In order to achieve lasing, the injected current must be sufficiently large to achieve optical gain. The optical feedback is obtained using mirrors or, more frequently, by cleaving the semiconductor material along its crystal planes and letting the sharp index contrast between the cleaved surfaces and air act as the cavity mirrors.

The actual semiconductor lasers offer better performance by using a double hetero p-i-n structure in which a low bandgap material is sandwiched between two high bandgap materials. In this way, the carriers are more effectively confined in the active region. The energy distribution of electron of double heterostructure is shown in figure 1.3.

When the junction is forward biased, the quasi Fermi levels (E_{Fc}) and (E_{Fv}) are located inside the conduction (E_C) and valence band (E_v). The carriers remain confined by the barrier created by the two high bandgap materials being forced to recombine and emit radiation by stimulated emission. The double heterostructure has two advantages

compared to simple P-N junction. The carriers are confined between the two energy barriers in the conduction band and valence band and the intrinsic layer acts as a waveguide formed by the two high band gap materials.

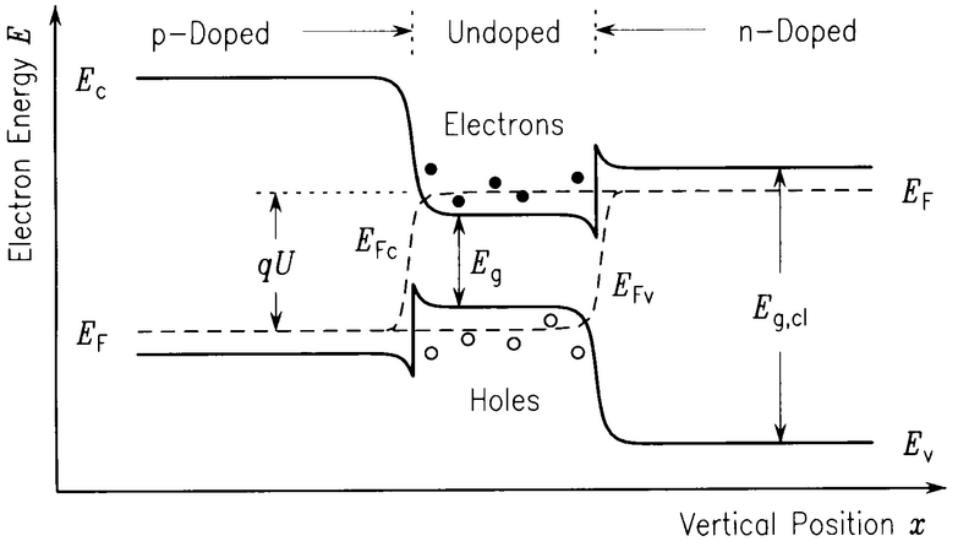

Fig. 1.3: Shows the p-i-n junction double heterostructure when it is forward biased. The conduction band and valence band are separated by the energy difference (E_g) [20].

1.4. Fabry Pérot laser configurations and coating

A resonator provides the necessary feedback for the amplification of the stimulated radiation. The simplest laser resonator consists of two highly reflecting mirrors with reflectivities R1 and R2, separated by a distance L. The simplest scheme for a semiconductor laser is based on this configuration called Fabry-Pérot laser or F-P laser. This configuration formed the fundamental basis of the open resonator, which allows lasing oscillation [22]. The mirrors provide feedback of the radiation generated in the active medium, which allows stimulated photons to return to the active medium. The standing wave profile between the mirrors gives rise to the development of longitudinal modes, but only those modes falling within the gain bandwidth of the active medium will be efficiently amplified [20]. For lasing action to take place, the gain must exceed the losses. In the edge emitting lasers, the two cleaved faces of the active medium form the resonator without the need of external mirrors. The refractive index difference between the semiconductor material and air results in a reflectivity of approximately 30%. The reflectivities of the facets are further controlled by the use of reflective coatings. Typically, the back facet of the diode laser is highly reflective coated, while the front facet remains uncoated or has an anti-reflection (AR) coating to reach a few percent reflectivity.

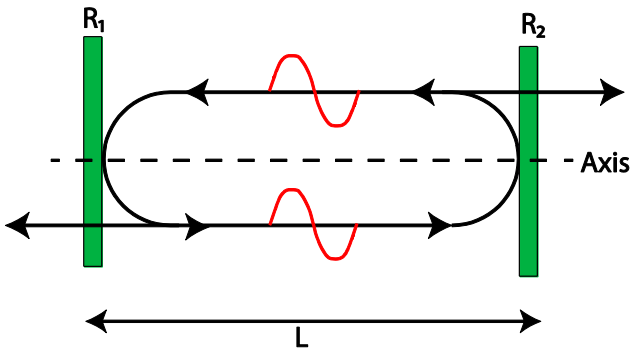

Fig. 1.4: Scheme of Fabry- Pérot laser with two reflective mirror separated by distance L.

Due to the large refractive index of the gain material in semiconductor lasers, the semiconductor/air interface on both sides naturally acts as partial mirrors providing reflections larger than 30%. Thanks to these properties, diode lasers can be mounted in a unique configuration where the active medium provides both the gain and the feedback simultaneously. For particular applications, the reflectivity of the facets can be altered by using a proper coating selection depending upon the application of the device. In high-power configurations, for instance, the rear facet is coated with a dielectric coating to increase the reflectivity, while the front facets can be AR coated. The AR coating or HR coating on the facets provides necessary passivation and reflectivity to obtain emission from only one side. With larger reflectivity, the threshold current decreases.

As an example, in diode laser bars the front facet is usually coated to get 4% reflectivity, while the rear facet is coated to give a 95% reflectivity. For amplifiers, both facets are AR coated (R<0.01%). In an extended cavity configuration, the front facet is coated with AR coating (R<0.01-0.1 %) to suppress unwanted reflections and prevent lasing from the active medium itself. The necessary feedback required for lasing is provided by the external mirror. The typical materials used for coating are Al_2O_3, MgF_2, and SiO2. The application of AR/HR coating on the facets of laser diode increases the effective efficiency of the device by nearly doubling the light output from one facet at a fixed drive current [23-24]. Additionally, diode laser facets can absorb light resulting in heat generation, which can degrade the facet and can even lead to catastrophic optical mirror damage (COMD), leading to an ultimate fail of the diode laser. The COMD is also limiting the power scalability. COMD is due to absorption of light at the facets, which has contamination from surrounding substances or to a faulty cleaving.

The right selection of the AR coatings is important for the operation of semiconductor lasers since they are highly-sensitive to the optical feedback. An excess of feedback can induce material damage that may immediately result in a loss of power or a reduction in the operative life of the device. The quality factor of this laser is poor due to its short cavity length and low reflectance of the output mirror. This leads to a reduced number

of photons inside the cavity with respect to other laser types, making the semiconductor laser very sensitive to the small amount of feedback. The optical feedback can also be used to control the stability of diode laser by locking the frequency of the laser to one of the modes of the external cavity for reduction of its linewidth [25].

1.5. Materials for semiconductor lasers

The materials required for lasing action in semiconductor lasers are found in the groups III-V of the periodic table. Usually compound materials from these two groups are used. Additionally, direct bandgap materials, providing momentum conservation, must be used. In indirect band gap semiconductor materials such as Ge or Si, the electron-hole recombination cannot take place without releasing the excess energy in the form of phonons. Many semiconductor materials have been investigated over the years. The typical materials used for semiconductor laser are GaAs, $In_xGa_{1-x}As$, $Al_xGa_{1-x}As$, InP, GaN, $In_xGa_{1-x}As_{1-y}P$, where the subscript (x, y) denotes the fraction of the given element in the material. Depending on this fraction, the wavelength of operation can be tuned. The first coherent stimulated emission was observed from GaAs material [10]. For lasers employing double heterostructure an important requirement is that the layers of semiconductor materials must be lattice-matched. Semiconductor lasers with Al-free materials (InGaAs/InGaP) have higher power conversion efficiencies due to their lower differential series resistance and higher conductivity [26-27]. In addition, an Al-free material has very tight carrier confinement and optical power densities (18-19 MW cm^{-2}) at catastrophic optical mirror damage (COMD).

1.6. Field confinement

The confinement of the optical field in the active region of the diode active region is very important for the operation of the laser. Field confinement can be evaluated through the use of the confinement factor [20]. The field confinement factor (Γ) measures the concentration of the field within the active region. If $J(x)$ is the optical intensity along the horizontal direction and d is the thickness of the active region, the confinement factor (Γ) is defined as follows:

$$\Gamma = \frac{\int_{-d/2}^{+d/2} J(x)dx}{\int_{-\infty}^{+\infty} J(x)\,dx} \tag{1.6}$$

The confinement factor depends on the overlap of the optical mode within the gain region of the laser. In semiconductor lasers, there are two ways to confine the optical field: through gain guiding and index guiding.

1.6.1. Gain guiding

In gain-guided lasers, optical gain is highest where the current density is higher. The carrier concentration is largest at the center of the stripe and it decreases away from center. Consequently, the center region has the highest gain and the edges have losses.

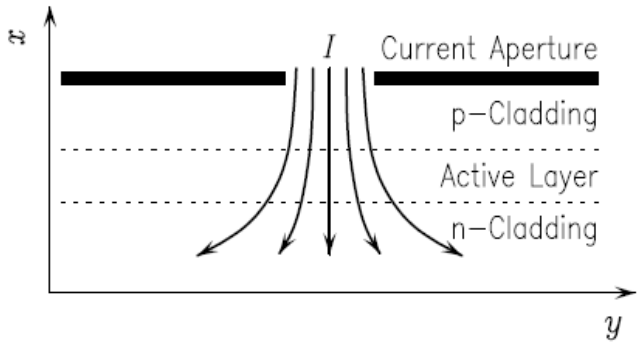

Fig. 1.5: Lateral confinement by current injected through the aperture [20].

From a fabrication point of view, gain guided lasers are easier to fabricate. The threshold current requirement is large. The disadvantage with this type of laser in broad area devices is that the confinement along the lateral mode is lost because of self-focusing and filamentation resulting in poor beam quality [28]. When the injection current increases, the refractive index changes due to free plasma effect and joule heating. The refractive index change (Δn_c) is given by:

$$\Delta n_c = \frac{e^2}{2m_c\omega^2\varepsilon_0 n} N_c \tag{1.7}$$

Where $e = 1.602 \times 10^{-19}$C is electron charge, $m_c = 9.1 \times 10^{-31}$Kg is the effective mass electron, $\varepsilon_0 = 8.85 \times 10^{-12}$ F.m^{-1} is the permittivity of free space, n is the refractive index, ω is the angular frequency of light. Assuming typical carrier concentration $N_c = 10^{18}$cm^{-3}, the refractive index will decrease approximately 10^{-3} [29]. The change in refractive index results in reduction of optical confinement called as anti-guiding effect. With increase in injection current, the temperature will also rise. This will lead to temperature induced refractive index change (Δn_T). The change in refractive index $\Delta n_T = 5 \times 10^{-4}\Delta T$. Where ΔT is change in temperature.

1.6.2. Index guiding

In this laser, the active region of high refractive index is surrounded by low refractive index material (high band gap). This arrangement acts like a dielectric waveguide [21]. This arrangement allows controlling the transverse modes. Because of the tight

confinement, the electron and hole density inside the active layer raises thereby raising the gain and reducing the threshold current. This type of laser produces high quality spatial beams, but the output power is typically limited to few hundred of milliwatts.

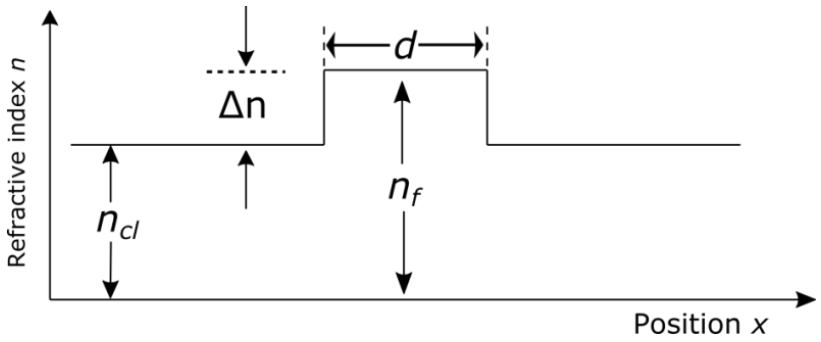

Fig. 1.6: Shows the optical confinement using index guiding.

1.7. Current versus light emission and Output power

Increasing the injection current in semiconductor lasers enhances the carrier concentration in the active layer. When the carrier concentration exceeds a threshold value, laser oscillation starts and the light output drastically increases compared to emission below threshold. The optical power (P_{opt}) of a diode laser is simply related to the injection current by the relation [30]:

$$P_{opt} = \frac{h\nu}{e}\eta_d(I - I_{th}) \tag{1.8}$$

Where $h\nu$ is the photon energy, e is the electron charge, I is the injection current, and I_{th} is threshold current. The differential quantum efficiency (η_d) is a critical parameter for maximizing output power and is defined by the relation:

$$\eta_d = \eta_i \frac{\alpha_m}{\alpha_m + \alpha_i} \tag{1.9}$$

Where η_i is the internal quantum efficiency, α_i are the internal losses and α_m the mirror losses. The mirror losses are related to the field losses over a round trip in the cavity and are related to the reflectivity of the mirrors (R_1 and R_2) and cavity length (l) through the relation.

$$\alpha_m = \frac{1}{2l}\ln\left(\frac{1}{R_1 R_2}\right) \tag{1.10}$$

1.7.1. Output power

The output power from semiconductor lasers can be in continuous wave mode (CW) or pulsed mode. The typical laser output power versus injected current curve is called L~I curve. The slope efficiency (η) is given as [31].

$$\eta = \frac{P}{(I - I_{th})} \tag{1.11}$$

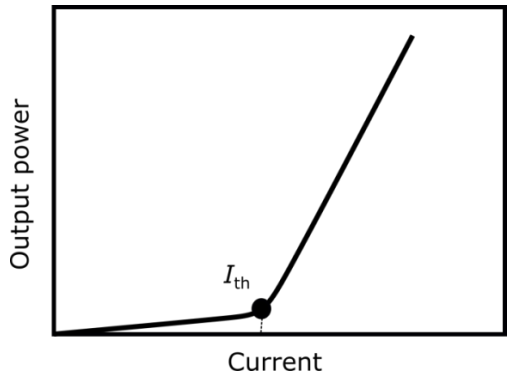

Fig. 1.7: L ~ I curve for semiconductor laser. I_{th} is the threshold current.

where P is the optical power, I_{th} is the threshold current and I is the operation current. The semiconductor laser emits only spontaneous emission below the threshold current. With increase in injection current, the gain inside the cavity overcomes all the losses, the stimulated emission increases and the output power rises rapidly with the increase in injection current.

1.8. Laser structure

As explained previously, the typical structure of a semiconductor laser consists of a double heterostructure formed by p-type and n-type semiconductor material. When the device is forward biased, the p-type is connected to a positive supply of voltage while the n-type is connected to the negative terminal. Under these conditions, the holes are injected from the p-side to the active region and the electrons are injected from the n-side. To achieve efficient recombination of electrons and holes, the carriers must be confined to the active layer [29]. The thickness of the active layer is 100 nm for bulk materials or 10 nm in the case of quantum wells, which improves the efficiency. When the radiative recombination of electrons and holes takes place at the junction, energy is emitted in the form of electromagnetic radiation. The amplification of radiation will occur when stimulated emission rate exceeds the spontaneous emission rate. To achieve high photon densities inside semiconductor lasers and sustain the laser emission, in edge

emitting lasers, the light bounces back and forth in the horizontal direction inside the structure. The end facets of edge emitting laser are obtained by cleaving the wafer along the crystal plane. The waveguide is formed by the high refractive index core sandwiched between the low refractive index cladding layers on both sides. In this configuration, the light is naturally guided without need for additional confinement techniques. The resonator length is between hundred of microns to few mm, enough to reach high gain even if resonator losses are high.

In the next section, we will discuss different geometries of edge emitting lasers each with own advantage-disadvantage. It is an important laser in high power regime.

1.8.1. Narrow strip laser

The output beam quality of this laser is nearly diffraction-limited in both directions. The confinement of optical mode along lateral direction is achieved using index guiding. The pump current is applied via a thin strip electrode, which is few µm and extends over the entire length of laser. The purpose of narrow strip is to confine the transverse mode oscillation and the transverse distribution of charge carriers. This laser supports single mode emission. The absence of multi transverse mode gives higher quality spatial beam. The output power from such laser is usually low because of the narrow width of the active region. Maximum output power of 1.5 W with M^2 of 1.3 in both axis has been demonstrated [32].

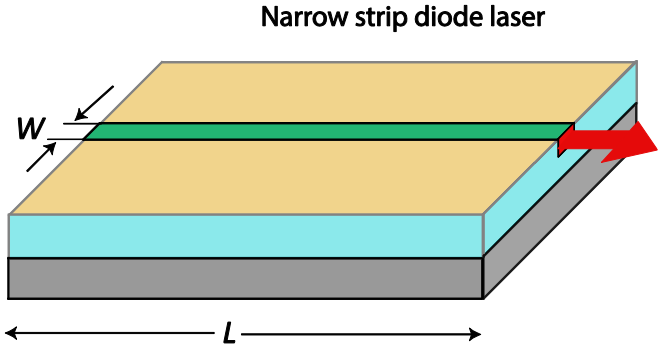

Fig. 1.8: Schematic view of a narrow stripe diode laser. The width (W) of the active region is few µm and L is the cavity length.

1.8.2. Tapered laser

Tapered laser is a monolithically integrated photonic device. It consists of two sections: an index guiding ridge waveguide and a gain guided broad area amplifier. The tapered section is typically 2 – 4 mm, the ridge section 0.3 – 1 mm long resulting in overall chip lengths of 2.5 – 6 mm. The total taper angle is 6° [33].

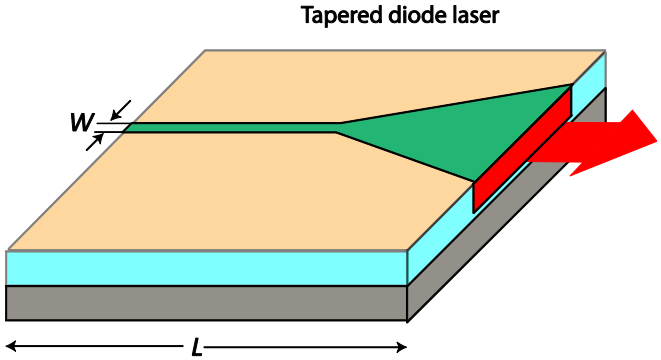

Fig. 1.9: Schematic view of a tapered diode laser. The width (*W*) of the active region is few µm and the amplifying region of hundreds of µm.

These lasers combine the advantages of higher beam quality from ridge waveguides and high optical power from the amplifier. One of the main advantage of monolithic integration is that it reduces the size and avoids the mechanical alignment error between two separate components. The diffraction limited output beam out of the index-guiding ridge is coupled into the tapered region for amplification of the output power. The output beam generally suffers from astigmatism.

1.8.3. Broad Area Laser

The output power from narrow strip lasers is usually limited to hundred mWs due to the possibility of catastrophic optical mirror damage (COMD). This limitation has overcome using broad area semiconductor (BAS) lasers, also called broad strip edge emitting diode lasers. "Broad" means that the dimension along the lateral side is large compared to wavelength. This laser allows increasing the output power by increasing the width of the emitting region.

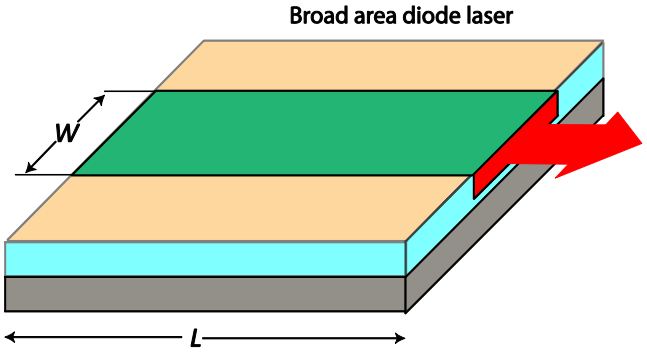

Fig. 1.10: The schematic representation of broad area diode laser. The width (*W*) of the active region can be between 50-400 µm and *L* is the cavity length.

The typical dimensions of the emitter are of few µm along the vertical axis and between 50-400 µm along the horizontal direction. The beam quality factor (M^2) along the vertical direction is close to 1 due to the small size aperture leading to single mode emission. In the horizontal direction, the beam has less divergence, but the light is distributed over many spatial modes due to elongated width. The wider the width of the active region, the higher is the achievable power but at expense of a poor beam quality along the horizontal direction.

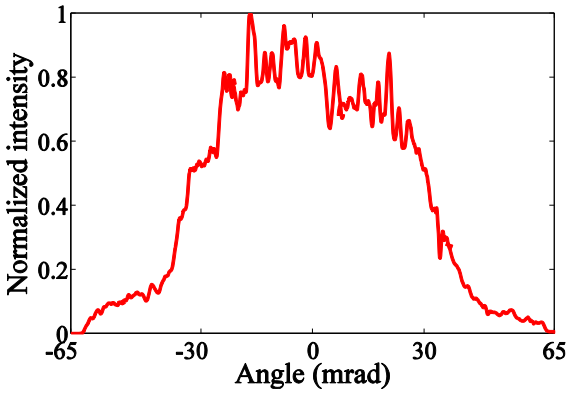

Fig. 1.11: Experimentally obtained far field profile from broad area laser (width = 400 µm).

The beam emitted from such laser has a large divergence angle along the vertical direction (Fast axis) due to small aperture size of the order of few micrometers. A high numerical aperture (NA) cylindrical lens is placed close to the facet before the beam diverges to collimate the beam in this direction. In the horizontal direction (slow axis), the beam has less divergence. In the far field, the output beam is elliptical in shape.

BAS laser output power emission upto 15 W has been demonstrated [34] and 73% power conversion efficiency at 970 nm diode laser bar has been demonstrated [35]. The BAS lasers usually come in different packages such as single emitters, diode laser bars and laser stacks. The output power from a single emitter is limited typically ranges from hundred of milliwatts [36] to tens of watts [34]. To increase the optical power further, a power-scaling approach is used in which several emitters are combined in a linear distribution. This linear arrangement is called bar, which can emit output powers of the order of hundreds of watts. Moreover, by stacking several bars, KW output power levels can be achieved in diode laser stack.

1.8.4. Single laser emitter

In this thesis, all the work is focus on broad area laser in single emitter configuration. The details will be discuss in chapter 4. The width along the fast axis is of the order of

few µm and can be considered as light point source, while along the slow axis can be between 50-400 µm. The output power from single emitters is usually low. Maximum output powers of 20 W have been demonstrated at 915 nm using single emitter [37].

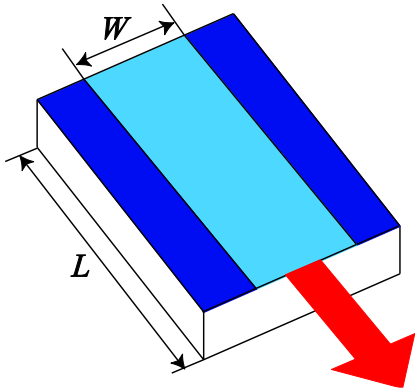

Fig. 1.12: Shows the broad area laser single emitter configuration. The width (W) of the active region and *L* length of the active.

1.8.5. Diode laser bar

Diode laser bars (DLB) are made by a combination of multiple broad area lasers mounted in a single package. The DLB usually consists of 19 to 69 emitters arranged linearly. The length along slow axis is 10 mm. A bar consisting of few number of emitters is called mini bar.

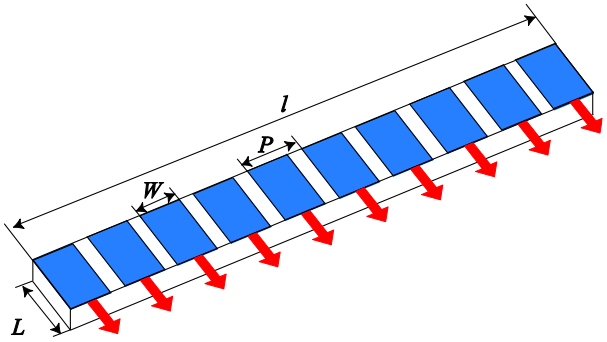

Fig. 1.13: Shows the diode laser bar schematic. The width (W) of the active region, *L* cavity length, the pitch of the emitter (*P*).

Each emitter has a well-defined width and is separated by a distance called “pitch”. The emitter width can be between 50-400 µm and the ratio of emitter width (*W*) to pitch (*P*) is called fill factor (%). The beam along vertical axis (fast axis) is considered as point source and the pitch between the emitters is small enough to consider that the radiation pattern along the slow axis can be considered as a single line source [38]. Output

powers exceeding 700 W in continuous wave regime has been demonstrated with single diode laser bar [39].

1.8.6. Diode laser stack

A diode laser stack consists of several DLB arranged in the form of stack. Each laser bar is separated from the other by a heat sink and the typical pitch between two bars is of the order of 1-2 mm.

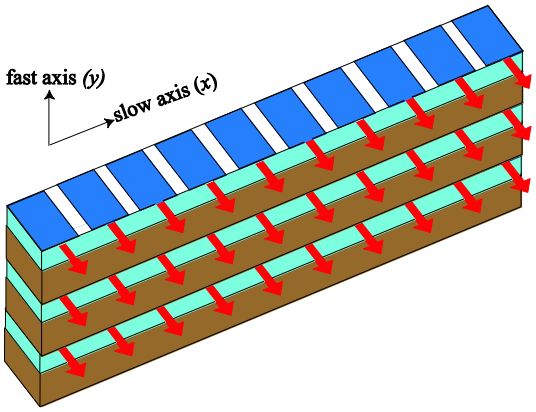

Fig. 1.14: Shows the diode laser stack configuration.

Each bar in the vertical direction has to be collimated first along the fast axis. The far field pattern of laser stack is rectangular. The laser stack can deliver powers of the order of KW. The maximum output power > 5 KW with 200 W per bar has been demonstrated in CW mode with more than 60 % power conversion efficiency [40].

1.8.7. Beam combination scheme

In order to scale up the power emission in diode lasers, a beam-combining technique in which the output from several lasers is combined to get a unified output can be used. The simplest approach is **incoherent or spectral beam combining** (SBC) in which several laser beams are combined to increase the total output power. Other method used for power scaling is **coherent beam combination**s (CBC) in which several lasers to be combined are positioned in side by side to form single beam.

The SBC technique combines several lasers operating at different wavelengths into one single beam. Wavelength division multiplexing is an example of SBC, which is commonly used in optical telecommunications. On the other hand, the CBC technique combines lasers operating at single wavelength by adjusting the phase of each laser to

match with the others. This method requires a precise control of the phases to the fraction of wavelength.

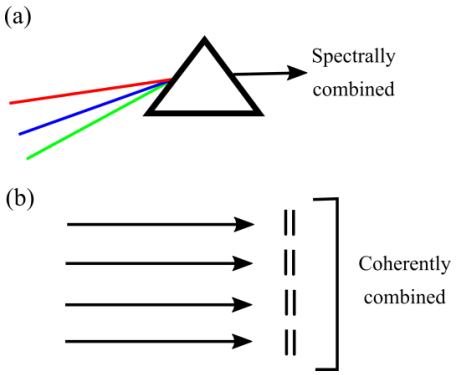

Fig. 1.15: shows the scheme of beam combination (a) incoherent or spectral (b) coherent beam combining [41].

1.9. Beam quality definition

The basic equation describing the propagation of monochromatic beams with arbitrary field amplitude

$$\vec{E}(x,y,z,t) = Re[\overrightarrow{E_0}(x,y,z)e^{iwt}] \tag{1.12}$$

Where E_0 is the complex amplitude, the Helmholtz equation is given by

$$\nabla \times (\nabla \times E_0) - k^2 E_0 = 0 \tag{1.13}$$

When the optical beam is highly directional or we want to study the beam only at the vicinity of a specific direction we can seek for simpler solutions. The region of interest close to a specific propagation direction is called the paraxial region and the expressions describing the optical beam within this region are called paraxial solutions. The paraxial beam is described by following equation.

$$\vec{E}(x,y,z,t) = Re[\hat{e}U(x,y,z)e^{i(kz-wt)}] \tag{1.14}$$

The lowest order transverse mode of an optical resonator is the Gaussian mode. The Gaussian beam is a case where the divergence angle is minimum so that paraxial approximation can be applied. In this approximation, the angle between the rays and reference axial rays is small, i.e.<< 1 rad. If the variations of field amplitude over distances of the wavelength are small, the slowly varying amplitude approximation is

also applied leading to the usual form of the paraxial wave equation for beams, given by:

$$\frac{\partial^2 U}{\partial x^2}+\frac{\partial^2 U}{\partial y^2}+2ik\frac{\partial U}{\partial z}=0 \tag{1.15}$$

A basic solution of the paraxial equation is the Fresnel's approximation of the spherical wave.

$$U(x,y,z)=\frac{U_0}{z}e^{ik\frac{(x^2+y^2)}{2z}} \tag{1.16}$$

The lowest order transverse mode of an optical resonator, the Gaussian beam, can be obtained from this solution replacing the variable z by a complex quantity, $q(z)=z-iz_R$, where z_R is the Rayleigh range and is a constant characterizing the properties of the beam. The Gaussian beam is, hence, a simple solution to the paraxial wave equation describing the properties of the optical beam in the paraxial region. For a monochromatic Gaussian beam propagating along the *z*-direction, the complex field amplitude can be expressed as [18].

$$U(r,z)=A_0\frac{w_0}{w(\mathrm{z})}e^{-\frac{x^2+y^2}{w^2(\mathrm{z})}}e^{-i\left[kz+\frac{k(x^2+y^2)}{2R(\mathrm{z})}-\varphi(z)\right]} \tag{1.17}$$

where

$$w(z)=w_0\sqrt{1+\left(\frac{z}{z_R}\right)^2}$$

$$R(z)=z\left(1+\left(\frac{z_R}{z}\right)^2\right)$$

$$\varphi(z)=tan^{-1}\frac{z}{z_R}$$

$$z_R=\frac{\pi {w_0}^2}{\lambda}$$

The beam waist (w_0) is located at z = 0 and corresponds to the minimum beam radius. At this plane the radius of curvature of the wave front, $R(z)$, is flat. As the beam propagates through space, the beam radius at any position z along the beam is given by $w(z)$. The planar wavefronts of the Gaussian beam at the beam waist plane become curved as the beam propagates, acquiring parabolic profiles given by the radius of curvature $R(z)$. The Rayleigh range is given by z_R. The beam radius at a distance z_R from the beam waist is a factor $\sqrt{2}$ larger and the intensity at the axis is decreased by a factor of two. The distance along the propagation direction where the beam is most confined, defined by the planes $z=\pm z_R$ (see Figure 1.16) is called the confocal parameter of the Gaussian beam.

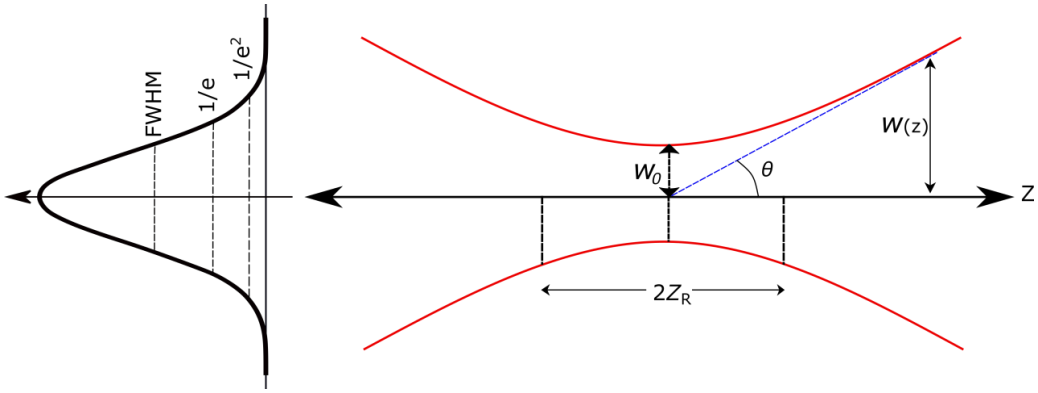

Fig.1.16: shows the beam caustic when the output beam is focused by lens. The beam waist (w_0) is shown and the divergence angle (θ). The total Rayleigh range is 2 z_R.

The Gaussian beam propagates in space maintaining a constant shape but with an increasing radius during propagation. The transverse spatial broadening of optical beams is an intrinsic characteristic of any transversally localized light distribution and is linked to the physical process called diffraction.

The divergence angle in the far field ($z \gg z_R$) is given by (θ).

$$\theta = \frac{\lambda}{\pi w_0} \tag{1.18}$$

Smaller the beam waist (w_0), shorter the Rayleigh range will be and larger will be the divergence angle. So tightly focused Gaussian beams tend to diverge very fast in the far field.

The Gaussian beam is not the only solution of paraxial wave equation. Other high-order mode solutions can be expressed using Hermite-Gaussian modes (rectangular co-ordinate) or Laguerre-Gaussian mode (cylindrical co-ordinate). The complex amplitude of Hermite-Gaussian beam is given by equation 1.19.

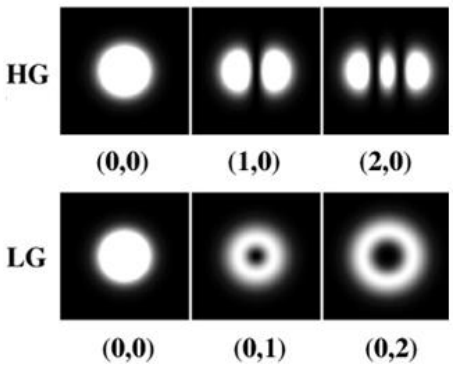

Fig. 1.17: Shows the intensity distribution of Hermite-Gauss (HG) and Laguerre-Gauss beam.

$$U_{l,m}(x,y,z) = A_{l,m}\left[\frac{w_0}{w(\mathrm{z})}\right] G_l\left[\frac{\sqrt{2}x}{w(\mathrm{z})}\right] G_m\left[\frac{\sqrt{2}y}{w(\mathrm{z})}\right] e^{-\frac{x^2+y^2}{w^2(\mathrm{z})}} e^{\left(-i\left[kz-(1+l+m)\varphi(z)+\frac{k(x^2+y^2)}{2R(\mathrm{z})}\right]\right)} \quad (1.19)$$

The equation (1.19) is Hermite-Gaussian beam of order *l, m.* The lower order (0, 0) is the simple Gaussian beam.

In reality, the beam emitted from semiconductor laser edge emitting laser is multiple transverse modes. Each mode is quasi-Gaussian mode. All these modes combine to form multimode beam. As all the modes propagate, they grown in size and merge with other modes to form a line in the far field. Such beam cannot be well collimated or focused into smaller spot.

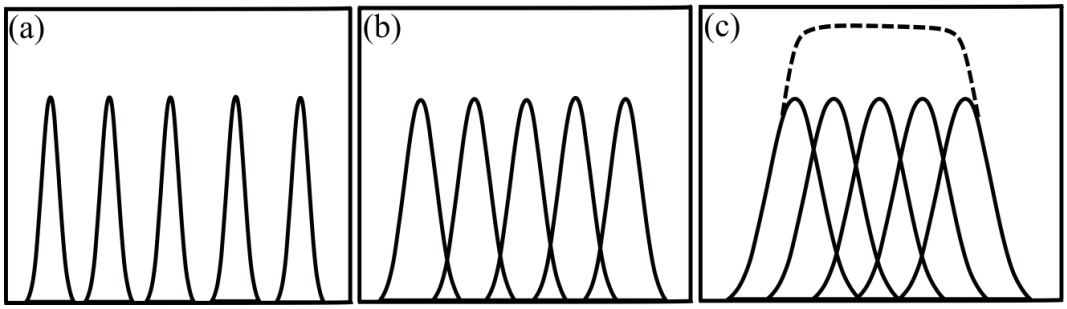

Fig. 1.18: Shows the emission of modes from broad stripe laser (a) emission near the facet of laser (b) after propagation of few microns (c) after propagation of tens of micron or more [31].

In practical laser beam, higher order Hermite beam is rarely observed. The higher order beam is usually characterized by M^2 factor, which defines how far the real beam from ideal TEM_{00} is. It is measures of difference between the real beam and theoretical limit given by diffraction. For higher order modes, M^2 tells about how many times the diameter of beam is larger than simple Gaussian beam. The introduction of the M^2 factor enables the equation set for basic mode Gaussian beam to describe non-basic mode Gaussian with reasonable accuracy and thereby significantly simplify the mathematics involved. In the next section, we will give the formula for M^2.

1.9.1. Beam parameter product (BPP)

The beam parameter product (BPP) of diffraction-limited beam is given by product of divergence angle and beam waist.

$$BPP = Beam\ waist\ (w_0) * Divergence\ angle\ (\theta) \quad (1.20)$$

The BPP can be different for non-diffraction limited beam along vertical and horizontal direction and is used to define the spatial quality of the beam. A lower BPP means a better beam quality. For semiconductor laser, the BPP along the two axes is quite different.

The beam quality factor (M^2) is defined as the beam parameter product of the measured beam divided by the corresponding product for a diffraction-limited Gaussian beam.

$$M^2 = \frac{BPP_{actual\ beam}}{BPP_{Gaussian\ beam}} \tag{1.21}$$

The beam quality factor (M^2) can be further written [42-43]:

$$M^2 = \frac{\pi}{\lambda}\frac{W\Theta}{4} \tag{1.22}$$

Where W is the diameter of the beam and Θ full divergence angle.

For a diffraction-limited Gaussian beam, the beam parameter product is BPP = λ/π, which gives M^2 close to 1. For gas laser such as He-Ne the M^2 can be between 1.1 to 1.3. For semiconductor lasers M^2 is close to 100. The details of M^2 measurement will be discussed in chapter 3 (section 3.4). In multimode laser diodes, the ridge widths are typically about 100 microns, which allows for a much larger volume of material to be actively involved in the lasing process and therefore generate higher laser powers. Additionally, this provides a larger surface area at the facet reducing the intensity and decreasing the risk of catastrophic optical damage.

1.9.2. Brightness of semiconductor laser

High brightness laser source offers many benefits over conventional source in terms of good beam quality, longer field of focus and low divergence. The high brightness diode lasers are in demand and offer several advantages over low brightness sources. This high brightness source is particularly interested in the field of material processing and pumping solid-state laser.

Diode lasers are usually high-gain oscillators. Accordingly, it is difficult to control their spatial and spectral properties. The spatial beam quality of diode laser is worse by 10-20 factor compared to other lasers whereas spectral output of these lasers is broader. Diode lasers offer roundtrip gains in the range 10^3 to 10^6 and are thus operated with correspondingly high roundtrip losses. A second complication, making the generation of high-brightness radiation particularly difficult with high power diode-lasers, is the strong optically nonlinear response of the amplifying semiconductor material [20].

The brightness of the laser beam is given by its optical power divided by the product of area of focused intensity and solid angle divergence [44].

$$B = \frac{P}{A\Omega} \tag{1.23}$$

For diffraction-limited beam, the brightness is given by its output power divided by its wavelength squared.

$$B = \frac{P}{\lambda^2} \tag{1.24}$$

For higher-order non-diffraction limited beams such as those from edge emitting laser, the M^2 factor can be significantly different in two perpendicular directions (x-horizontal direction and y-vertical direction). Thus, brightness for edge emitting laser is given by output power divided by M^2 factor along vertical and horizontal directions [45].

$$B = \frac{P}{\lambda^2 M_x^2 M_y^2} \tag{1.25}$$

Where P is the average power of the beam, M_x^2 and M_y^2 are the beam quality factor along horizontal (slow axis) and vertical direction (fast axis). For diffraction-limited beam, the M^2 are close to 1 in both direction. The brightness can be enhanced either by increasing optical power or by decreasing M^2 value. In semiconductor lasers, due to low mode selectivity of Fabry-Pérot cavity, it results in higher order transverse modes emission. The M_x^2 can be decreased by reducing the far field divergence angle and decreasing the width of active region. For broad area laser with hundreds of micron width results in M_x^2 order of 100, which is quite larger than the diffraction limited beam.

Chapter 2

Photonic crystal

The first **Photonic crystals** (PhC) were studied in the year 1887 by Lord Rayleigh as 1D periodic stack with alternating layers of materials with different dielectric constants [46]. In his work, he showed that such system could have photonic bandgap i.e. forbidden range of frequencies where the waves cannot propagate inside the structure. The photonic bandgap is due to modification of the dispersion relation by the structure. In the year 1972, Bykov investigated for the first time the effect of the photonic bandgap of 1D PhC on the spontaneous emission of an atom [47-48]. The idea of 3D PhC was discussed by Ohtaka [49]. However, after the work of Yablonovitch [50] and John [51], the field has grown rapidly. Recently many novel phenomena such as negative refraction [52], slow light effect [53] and photonic devices such as photonic crystal laser [54], optical switching [55] have been demonstrated. A lot of research in this field has been carried out over the years demonstrating that the PhC can be promising solution to control the propagation and shaping of optical beams. In addition, due to their compact size, the PhC could be used in micro optical and photonic integrated devices. Due to such advantages, the PhC will play an important role in designing an all-optical circuit in near future.

Introduction

Photonic crystal (PhC) structures are fabricated by introducing a periodic variation of the dielectric constants or refractive index on the wavelength scale [56]. The periodicity can occur in 1D, 2D and 3D as shown in figure 2.1.

A 1D PhC usually consists of a Bragg grating, a periodic distribution of two alternating materials along one particular direction, defining the PhC axis. These PhCs offer a limited number of possible periodic structure variations so only the refractive index, layer's thickness and the number of layers can be varied. In these structures, a chirped distribution of the periodicity can be introduced to broaden the bandgap or include some wavelength or frequency dependent propagation effects. 1D PhCs are widely used in high reflective mirror and anti-reflection coated lenses.

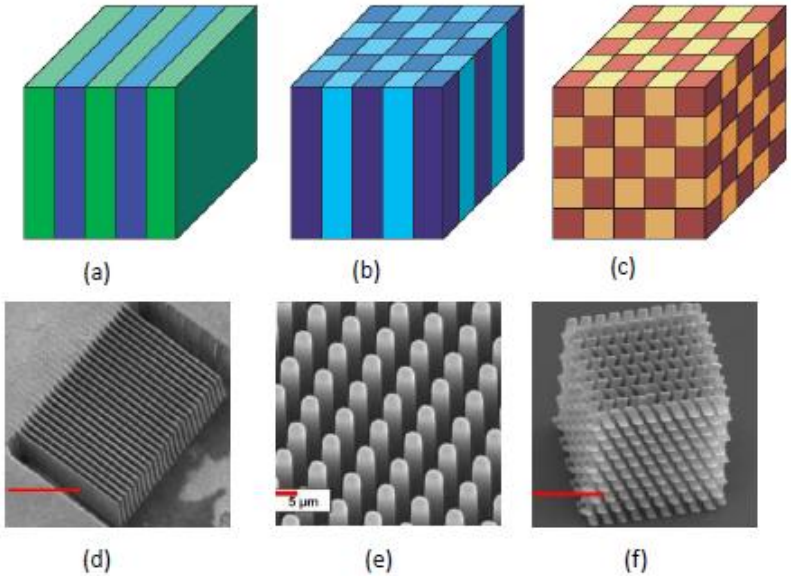

Fig. 2.1: Schematic representation of (a) 1D, (b) 2D and (c) 3D photonic crystals [56]. SEM images of (d) 1D periodic structure scale marked in red is of 500 µm [57]; (e) 2D PhC consisting of periodically arranged rods [58]; (f) 3D PhC fabricated by two photon polymerization technique scale is of 16 µm [59].

In 2D PhCs, the periodicity of the refractive index shows a modulation along two directions forming a lattice pattern with defined symmetry. The variation of the unit-cell shape and their distribution gives the possibility to create many different lattice types. However, for technological reasons, the two most commonly used types of 2D PhC are the square and the hexagonal lattice. The unit cell of the PhC with square lattice has the shape of a square and its characterized by its longitudinal and transverse period. These structures have been discussed, for instance, in the study of the generation of non-diffracting beams [60]. The unit cell of hexagonal lattice has the form of regular

hexagon. 2D PhCs are widely used in hollow photonic crystals, where light is trapped inside the core due to photonic bandgap.

3D PhCs possess a refractive index variation along the three directions and can have different lattice types and a much richer structure of their dispersion relation. Their geometry can be varied in very different manners so they can have a great number of lattice types. Because 3D PhCs are the most similar to solid-state crystals, many lattice types of such PhCs have similar conformation and similar names. Moreover, depending on the method of the PhC production, they can possess periodic distributions that cannot be obtained in solid-state crystals. 3D PhC are not so common in use due to difficulty in fabricating the structure, but are under extensive research.

The periodic modulation of the dielectric constant in PhCs is the reason of the appearance of photonic bandgaps. At the frequencies within the gap, the wave vector becomes imaginary and light is not able to propagate inside the structure being totally reflected. Besides the similarity between electronic and photonic band gaps, there exist some distinctions between them mainly due to the differences in energy distribution of particles (electrons follow Fermi-Dirac distribution while photons obey Bose-Einstein distribution). In addition, the electrons are affected by interactions with the lattice and among themselves during propagation inside the material (intra-crystalline fields) while photons propagation remains unaffected by intra-crystalline field, leading to simplified computation of optical field distribution and photonic band structures.

The band structure of the PhC gives the most general information about the PhC properties. Computation of the band gaps for infinite periodic structures show a number of eigen states or eigen frequencies for specific values of the wave vector. The gaps appear as a consequence of the interference of the different Fresnel reflections appearing inside the medium at each interface where constructive and destructive interference between forward and backward waves causes either transmission or reflection of the radiation. The gap formation can be also studied as the result of the coupling between modes at the edges of the Brillouin zone.

Photonic structures have been occurring in nature for several million years. The color is used for communication and causes a direct impact in the way living beings interact. Photonic crystals occur in plants and animals showing a characteristic iridescence, whereby their color can change depending upon the angle of the viewer and/or the light illuminating it. For example, Camouflage often changes its color in response to external stimuli [61]. The color of a butterfly wing depends on the interaction of light with the wings and their spatial structure. Many butterfly and Beetle species wings have 1D, 2D and 3D PhC structure [62]. Plant leaves shows reflections due to their multilayer structure (1D PhC) [63]. Some fish can change color in response to light due to multilayer reflector in their iridophores. Motivated by the natural PhC, scientists try to imitate artificial structure in the laboratory.

Fig. 2.2: Color iridescence in (a) Beetle [64] (b) Paradise whiptail [61] (c) Callophrys butterfly [65].

2.1. Temporal dispersion

The periodicity of the PhC leads to a change of the propagation properties of electromagnetic waves depending on the temporal and spatial frequency of the incident wave. The modification of the temporal dispersion relation, the dependence of the frequency of the eigenmodes (Bloch modes) on the modulus of propagation wave number $\omega = \omega(k)$, leads to formation of photonic bandgaps (PBG) in the frequency domain. If, for some frequency range, the PBG occurs at all incidence angles, as well as for both polarizations of light, we call it a complete PBG. In such a crystal, light with frequency within the complete PBG cannot propagate. In other words, a complete PBG is the range of frequencies for which there are no propagating (real $\vec{k}$) solutions. If the bandgap exists in certain directions only, but not all propagation direction it is called pseudo bandgap, which exist only over certain range of wave vectors. The PBGs are angle-dependent due to the different periodicities experienced by light propagating at different incidence angles, which results in the fact that the reflected light depends sharply on the angle.

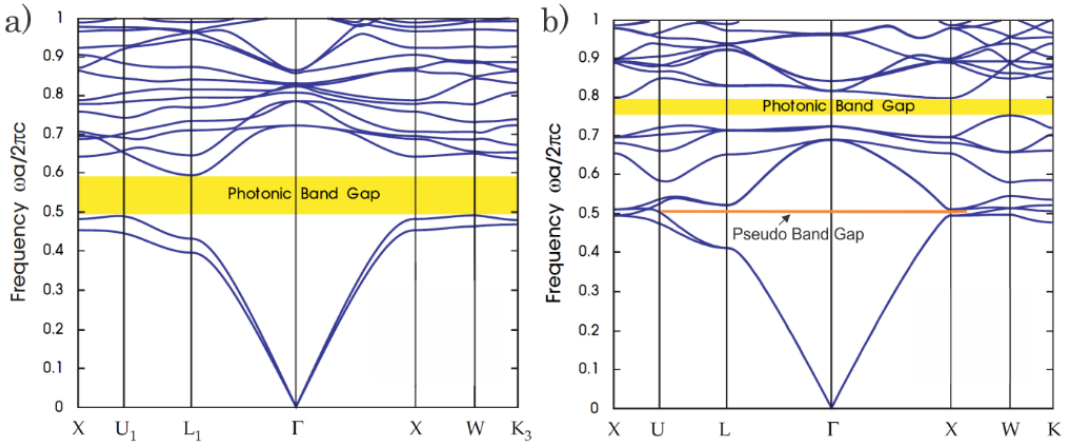

Fig. 2.3: The photonic band structure (a) for Yablonite structure, producing full photonic bandgap [56]; (b) shows narrow as well as pseudo bandgap.

In the year 1991, Yablonovitch demonstrated in his experimental work that 3D PhC can have complete bandgap [66]. The PhC was modification of diamond structure (called Yablonovite) and it was constructed by drilling air holes in a dielectric material. This was demonstrated in the microwave regime. The first demonstration of a structure showing a complete 2D bandgap in visible region was demonstrated in 1999 by Cregan et al. [67] while structures with a full 3D bandgap were demonstrated in titania woodpiles by Frölich et al. in 2013 [68]. From the fabrication point of view, 3D PhC with periodicity smaller than wavelength of visible light is a difficult task due to the small scale of the periodicity to be imprinted in the structure.

The curvature of the dispersion relation leads to a change in group velocity and close to the band edges results in a large reduction of group velocity leading to slow light effects or strong interaction with the lattice.

2.2. 1-D Photonic crystal

The 1D PhC is the simplest structure with a linear arrangement of high and low refractive index variations (see figure 2.1(a, d)) possessing many interesting applications. A multilayer film is an example of this crystal and has been used in high-reflective mirrors and anti-reflection coatings, which allows minimizing the reflection from surfaces and improving the quality of lenses. Bragg gratings are another example used as distributed reflectors in vertical cavity surface emitting lasers. When a wave propagates through such structure, multiple reflections and refractions occur at each interface, leading to enhanced reflection at particular directions defined by the 1D structure periodicity and the incident wavelength. In 1D PhCs, there is no complete bandgap, i.e. there are no frequencies for which propagation is inhibited in all directions.

2.2.1. Frequency band gap

The simple 1D periodic structures consisting of high-low refractive index reflects wave efficiently with wavelength $\lambda = 2d$, where d denotes period of the structure. This condition is called Bragg reflection for normal incidence. The constructive interference takes place when the waves reflecting from different layers are in phase with each other. In this way, the bandgap appears [50-51, 66, 69-70]. The waves at those particular frequencies cannot propagate inside the structure and ultimately reflect back. The central frequency of band gap is equal to $\omega_m = \frac{\pi c}{d} m$ or ($\lambda = \frac{2d}{m}$) where m is the order of the band-gap, ω_m is directly related to the period of the structure. The width ($\Delta\omega_m$)

of the photonic band-gap is different for different values of m and depends on the refractive index contrast.

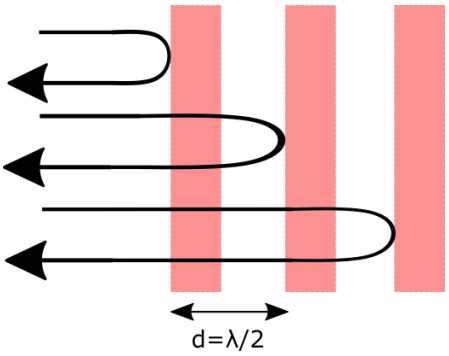

Fig. 2.4: Shows the reflection from periodic structure resulting in constructive interference.

Very roughly, the width for the first band-gap is $\Delta\omega_m = \frac{\pi c}{d}\Delta n$, with higher refractive index contrast Δn between the materials, the broader is the width of band-gap. Fig. 2.5(b) shows the dispersion relation for a periodic material having refractive indices $n_1 = 2.17$ and $n_2 = 1.49$ and layer thicknesses $d_1 = 0.8\,\mu m$ and $d_2 = 0.8\,\mu m$ with a total period $d = 0.16\,\mu m$. An effective refractive index can be calculated for the whole structure as $n_{eff} = \sqrt{(d_1 n_1^2 + d_2 n_2^2)/(d_1 + d_2)}$. For 1D PhCs with equal layer-thickness, $d_1 = d_2$, the effective index becomes $n_{eff} = \sqrt{(n_1^2 + n_2^2)/2}$.

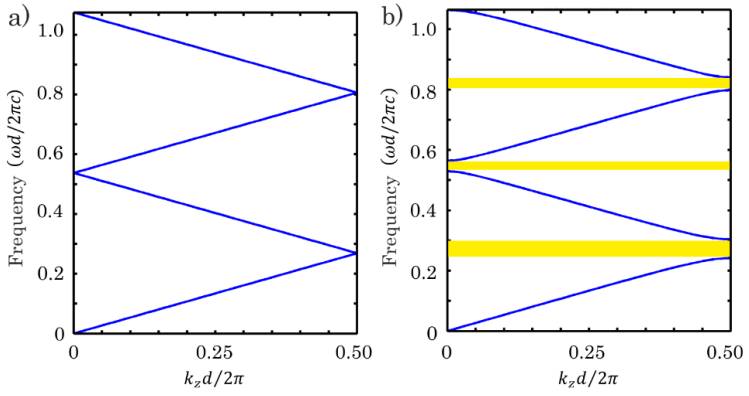

Fig. 2. 5: (a) Shows the dispersion relation of material with no refractive index contrast. (b) dispersion relation for the periodic structure with period $d = 0.16\,\mu m$ ($d_1 = d_2 = 0.8\,\mu m$) and refractive index between the materials are $n_1 = 2.17$, $n_2 = 1.49$ [71].

2.2.2. Chirping of PhC

One of the possible ways to increase the bandgap width of PhC is to use chirped structures. In this method, the chirp can be introduced either by varying the refractive

index contrast along the structure or by increasing/decreasing the period of the structure. In PhCs with linear chirp, the period is increasing linearly with the propagation distance, resulting in an increase of the total bandgap (the larger the difference between first and last period, broader is the bandwidth of bandgap) and a central frequency of the bandgap that can be changed.

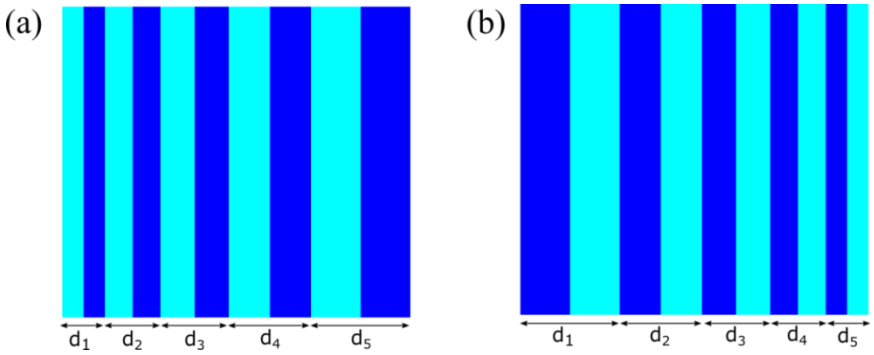

Fig. 2.6: Shows the chirp structure (a) period are linearly increasing from left to right (b) period are decreasing from left to right [71].

2.2.3. Defect in 1D PhC

The periodicity of the structure can be changed by introducing defects. There are few ways to introduce disorder in the structure, introducing a slightly different width or using different material layer (refractive index change) in some of the layers.

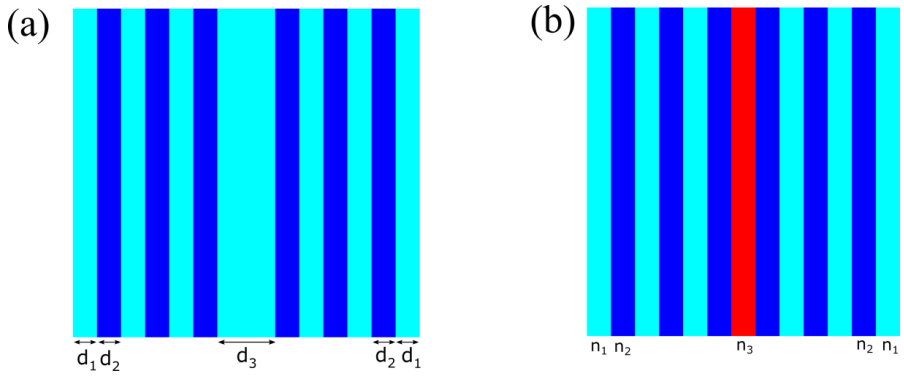

Fig. 2.7: PhC having defect (a) with different period width (b) with different refractive index of the layer.

The presence of defects alters strongly the dispersion relation, introducing localized states within the band gaps of the perfectly periodic PhC. If the width of the defect layer or its refractive index is increased, increasing the optical path, the modes appear in the bandgap from the upper edge of the frequency band edge leading to an increase of the wavelength of the defect mode [72]. In 2D PhCs, line defects can also be introduced,

acting as waveguides, which can transport light around tight corners with no losses. A localized defect in 3D PhC can be used to trap the light and create optical cavities with large quality factors.

2.2.4. Angular bandgap

The frequency filtering principle can be applied to the angular or spatial filtering of a light beam. The illustration of this idea is shown in figure 2.8 for a case with oblique incidence in a 1D PhC. For oblique incidence, the Bragg condition for the central wavelength of the bandgap is given by:

$$2k_{\parallel} = q, \qquad 2\frac{2\pi}{\lambda_{BG}}cos\alpha = \frac{2\pi}{d}, \tag{2.1}$$

$$\lambda_{BG} = 2dcos\alpha, \tag{2.2}$$

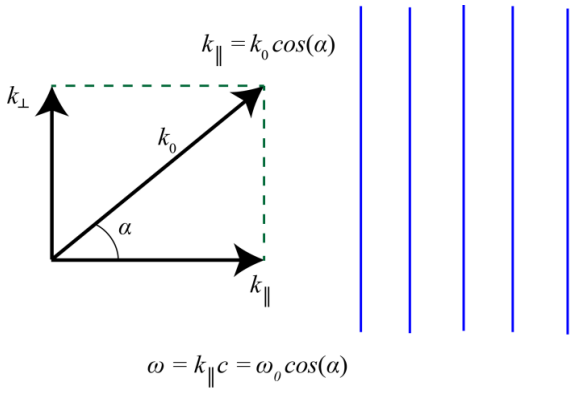

Fig. 2.8: Angular bandgap in 1D PhC structure.

Where $k_{\parallel}$ is the longitudinal wave vector of the incident wave, q is the reciprocal period of the 1D structure, α is the incidence angle and λ the medium wavelength. The effect of the structure for arbitrary incident beams can be obtained by Fourier decomposing the incident field into a set of spatial frequency components with given $\vec{k}$ vectors and different α values and calculating the reflection and transmission using matrix methods [71]. The Bragg condition (Eq. 2.2) for wave with oblique incidence will apply for longitudinal components of wave vector $k_{\parallel}$.

Spatial filtering leads to transmission of the structure depending on the incident angles, leading to the appearance of angular bands where light is totally reflected. Using 1D PhCs for spatial filtering is inefficient as the position of angular bandgap highly depends on the longitudinal period and filtering angles of practical interest, smaller than 1°, cannot be achieved using such structures.

2.3. Spatial dispersion

An adequate management of spatial dispersion phenomenon offers the possibility to control the light propagation in PhCs. It was first proposed by H. Kosaka as an alternative approach to control the propagation of photons in devices based on allowed photonic bands. Many effects, such as super collimation, flat lensing, negative refraction, superprism and spatial filtering of light are based on spatial dispersion properties.

A monochromatic beam having finite transverse width can be decomposed into a set of plane waves propagating with particular directions. If we project all the plane waves ($\vec{k}$ vectors) of the beam into the direction of propagation (longitudinal wave vector components), k_z , we obtain a delay for each component compared to central part of the beam $k_{\parallel} = k_z = (|\vec{k}|^2 - |\vec{k}_{\perp}|^2)^{1/2}$, where $k_{\parallel}$ is the central component of the beam and $\vec{k}_{\perp}= (k_x, k_y)$ is the perpendicular component. These waves will acquire phase shifts during propagation depending on their propagation angles. When the beam propagates through a homogeneous medium, this phase-shift leads to a spatial dispersion relation as the one shown in Fig. 2.9 (a), where the phase difference appearing between the different components in the propagation direction leads to a broadening of the beam. This is the regime for positive diffraction also called normal diffraction.

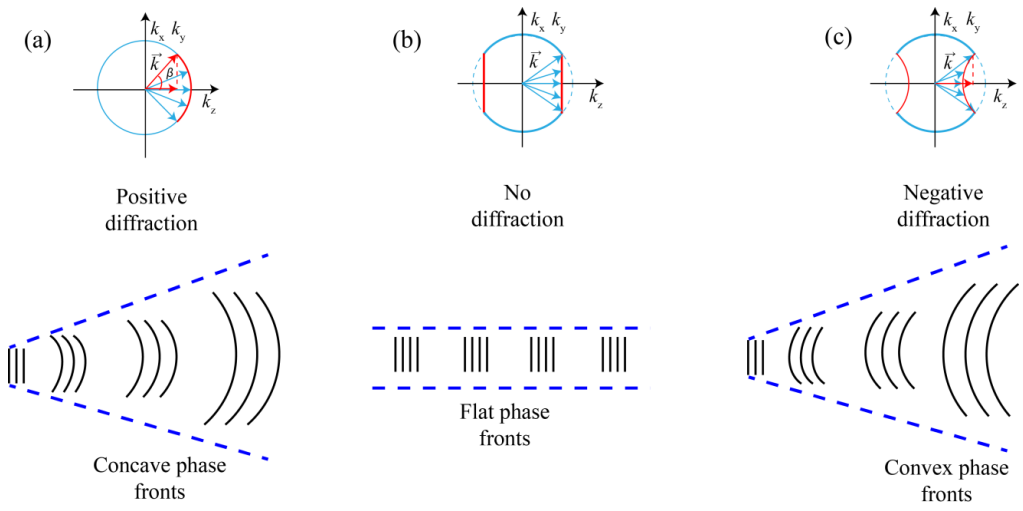

Fig. 2.9: Geometrical interpretation of diffraction of beam propagating along *z*-axis. (a) Propagation for normal diffraction (b) no diffraction (c) negative diffraction.

The spherical (parabolic in paraxial approximation) contours of the spatial dispersion relation are modified in a PhC, leading to the appearance of regions with different curvatures as shown in Fig. 2.9 (b) and (c). Self-collimation effects occur when the iso-frequency contours of the PhC bands are flat. In this case, light beams can travel

without diffractive broadening [73-74] and all the $\vec{k}$ vectors propagate with the same velocity with respect to the z-axis.

Another modified dispersion effect also occurs when propagating through PhC where the phase fronts are convex as in Fig. 2.9 (c). In this case, the phase of the modes propagating off-axis is opposite to the case of normal dispersion and the beam gets focused instead of diffracted. Such phenomenon is called negative diffraction or anomalous diffraction. When the isofrequency contours are strongly curved, it gives rise to another effect, called superprism. The beam entering the superprism will lead to large angular dispersion [75]. Super lensing effect is caused by negative refraction of light [76]. Such anomalous refraction might be created by convex curved isofrequency contours. Spatial filtering of light is also achieved by allowing the light to propagate in particular direction.

2.4. Spatial filtering

As explained in the previous section, PhCs allow to control the properties of light propagation as a function of their transverse wave vector, $k_{\perp}$. This possibility can be exploited in different ways and, in particular, a very interesting application is to use such crystals for **spatial filtering.** By spatial filtering, we mean the possibility to act on the different spatial frequencies of the incident beam to change their spatial characteristics.

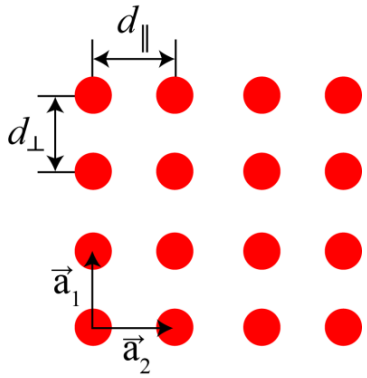

Fig. 2.10: Shows the 2D square lattice with transverse ($d_{\perp}$) and longitudinal period ($d_{\parallel}$).

In this thesis, the work is focused on the spatial filtering of semiconductor laser beams using PhCs. As we discussed in the section 2.2, the 1D PhC performance in terms of angular filtering is quite modest. The position of angular bandgap can be, however, controlled precisely using 2D PhCs with refractive index modulation in longitudinal and transverse direction. The parameters of the PhC determining the range of angular

components that can be filtered, that is, removed from the propagating beam, are the longitudinal and the transverse period. The effect of the PhC on the Bloch modes can be illustrated in the iso-frequency curves of the dispersion relation, where the plane waves propagating inside the angular bandgap cannot propagate and, hence, will be back reflected disappearing from the forward propagating wave. From this idea, efficient low-pass filters can be designed by achieving high transmission for axial components of the beam and reflection or deflection of the off-axis (diverging) components that we want to filter out.

Different types of filters may be conceived, depending on the propagation direction of the angular components filtered by the crystal. These can be classified in two types: Bragg diffraction (backward deflection) or Laue diffraction (forward deflection) regimes.

2.4.1. Bragg diffraction

In this regime, waves diffract in the backward direction as seen in fig. 2.11. The angular components in resonance with a reciprocal lattice vector of the periodic structure are back scattered into backward propagating modes [77-79].

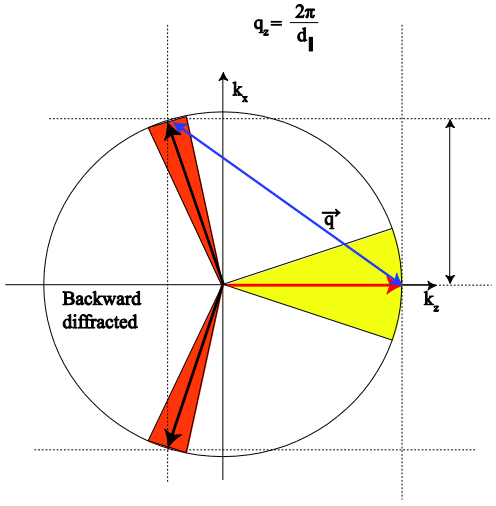

Fig. 2.11: Schematic of spatial filtering in Bragg regime where the diffracted wave components propagate in the backward direction.

To obtain an angular band gap at a particular wavelength, the longitudinal period of the structure should be less than the wavelength of light.

$$(d_\parallel < \lambda) \text{ or } \left|\vec{q_\parallel}\right| > \left|\vec{k_\parallel}\right|$$

where $\overrightarrow{q_{\parallel}}$ is the longitudinal component of the wavevector. From the fabrication point of view, a Bragg structure (mostly $d_{\parallel} < \lambda/2$) is difficult to fabricate for optical beams in the visible range.

Holographic techniques using UV light source are used to fabricate this type of structures [80]. Angular filtering in Bragg regime was fabricated by physical vapor deposition technique [81]. Bragg diffraction appears naturally in diffraction from crystalline solids when illuminated with X-ray wavelengths and is one of the most powerful techniques to study the geometrical configuration of solids.

2.4.2. Laue diffraction

In this case, the deflection of the spatial modes in the particular angular range takes place although no full photonic bandgap exists in the structure and, hence, the filtering using such crystals is also called gap-less filtering. The first proof of spatial filtering using PhC arranged in a gapless configuration was experimentally demonstrated by Maigyte et al. [82]. In the Laue regime, the PhC works by deflecting the waves in the forward direction, i.e., the resonant interaction takes place in the forward direction. From the fabrication point of view, PhC in the Laue regime are easier to fabricate because the longitudinal periods involved can be greater than the wavelength of light.

$$(d_{\parallel} > \lambda) \text{ or } \left|\overrightarrow{q_{\parallel}}\right| < \left|\overrightarrow{k_{\parallel}}\right|$$

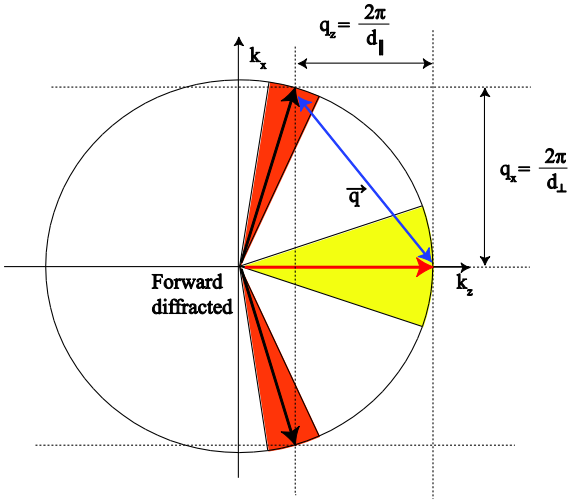

Fig. 2.12: Schematic of spatial filtering in Laue regime where the diffracted wave propagates in the forward direction.

However, the efficiency of the filtering is reduced, because some of the wave components deflected in the forward direction can be scattered back into the modes of

initial radiation [83]. The PhC used in our work is based on Laue configuration. The fabrication details are discussed in chapter 3.

In paraxial approximation, the expression for the filtering angle is given by [84]:

$$sin\alpha = \frac{q_\perp}{2k}(Q-1) \tag{2.3}$$

Where $q_\perp = 2\pi/d_\perp$ is the transverse wave number of the index modulation, $k = 2\pi/\lambda$ is the wave number of the electromagnetic wave, $Q = 2d_\perp^2\, n/\lambda d_\parallel$ is the geometry factor, and *n* is average refractive index. The filtering angle depends on the longitudinal period of the structure through the Q parameter. By introducing the chirp in the longitudinal period and keeping the other parameters constant, the filtering angle can be varied. Chirping of the structure improves the filtering performance. Other possibilities are increasing the refractive index contrast or increasing the length of the structure. However, these latter possibilities are conditioned by the current technology fabrication processes.

So far we have discussed about the photonic crystal, its types and the phenomena associated with it. In the last section of this chapter we will discuss about the light-glass interaction, fabrication methods of PhC and multiphoton absorption inside the glass.

2.5. Glass processing

In this section, we will discuss briefly some key aspects of the crystal fabrication properties concerning the glass and laser-light interaction. We will not enter into many details since we were not fabricating directly the crystals in this thesis, but were provided by our collaborators.

Glass has unique capabilities compared to other materials. From the optical point of view, it can reflect, transmit or absorb incident light. It is chemically corrosion-resistant and inert so that it can be used as container for chemicals. It is an excellent insulator of heat and electricity and mechanically it is hard surface. However, all these properties make glass processiing a challenging task. Typical glass materials, such as silica, have a bandgap larger than the energy of visible light and, hence are highly transparent. Photons with energies below the bandgap will not be absorbed unless there are some impurity or defects in the material.

Due to such a low absorbance, the treatment of the glass using laser light is difficult. However, it is possible to process the glass in the non-linear regime by using focused femtosecond laser beam into the material. The induce intensity at the foused spot is large enough to modify locally the refractive index. The advantage of femtosecond over nanosecond laser pulses is that it will have less thermal diffusion, allowing high-

precision material processing. The laser irradiation can alter both the optical and the chemical properties of the glass. The PhCs are generally fabricated on N-BK7 glass substrate using femotsecond laser, inscribing waveguides on different glasses achieving refractive index changes of the order of 0.01-0.035 [85].

2. 6. Fabrication techniques of PhC

The PhC can be fabricated using different methods such as electron beam lithography [86], photolithography [87], holography [88] and direct laser writing [89]. For long time 1D structures were fabricated using vapor deposition technique. Depending on the material and parameters required suitable technique were used to fabricate the structure. In this section, we will briefly describe these techniques.

Lithography in which the PhC layer are built by etching cross section of PhC pattern on to substrate. The etched holes are filled with the different material and second layer of substrate is deposited. The process is repeated for required number of layers [90].

Photolithography is a process of transfer shapes from photo mask onto substrate using light. The photolithographic microstructuring of photosensitive materials is applied, where after light exposure and structuring of one layer it is lowered in a bath of liquid photoresist, and a second layer is exposed on top of the first. The sequential steps are repeated until the desired height of the structure is reached [91]. This technique requires expensive clean room facility and specialized skills.

Holographic lithography, also known as multibeam interference lithography, can be used for the fabrication of the PhCs. The light distribution resulting from multiple beam interference can have spatial periodicity on the order of wavelength. The interference pattern using photoresist material can be recorded as volume hologram and then converted into PhC. Using holographic lithography large PhCs samples, with high flexibility in unit cells can be fabricated. However, the structures are strictly periodic, therefore additional methods to introduce defects should be applied. It is a mask free technique.

Electron beam lithography uses focused beam electrons to create tiny structure across surface. The advantage of using electron beam lithography over other patterning techniques is that there is no need to fabricate a mask and so the pattern can be transferred directly onto the substrate.

In this thesis, the PhC is inscribed on the glass substrate using **direct laser writing** (DLW) technique. In DLW, a tightly focused laser beam at a particular frequency, this initiates the multi-photon absorption in the material and sequentially the polymerization. The shape of an object can therefore be traced out by the laser. Femtosecond laser

irradiation can modify the interior of glass in a spatially selective manner through multiphoton absorption. When such femtosecond beam is focused inside glass material with enough pulse energy, the absorption is confined near to focal point inside the material. The main advantages of the DLW method are that there is no necessity for using a mask, easy to operate, small structures can be fabricated in relatively short time, and complicated 3D structures can be designed and printed in a straightforward manner. In the next chapter, we will discuss about the details of fabrication of PhC using Bessel beam.

2. 7. Multiphoton absorption

Single photon can excite the electron from valence band to conduction band if the energy of incident photon is equal to bandgap energy of the material [92]. If not, electron cannot be excited to higher level. Multiphoton absorption (MPA) is a non-linear process in which electron is excited to higher energy state by absorption of several photons. The process of single and multiphoton process is illustrated in fig. 2.13.

Due to the nonlinear nature of MPA, photochemical or photophysical events can be localized within the focal volume of an ultrafast laser beam that has passed through a microscope objective. The MPA process can be induced only at intensities above a critical value that depends on both the material and the pulse width. If the intensity of light exceeds a certain threshold values, non-linear photon absorption occur within focal spot leading to polymerization process.

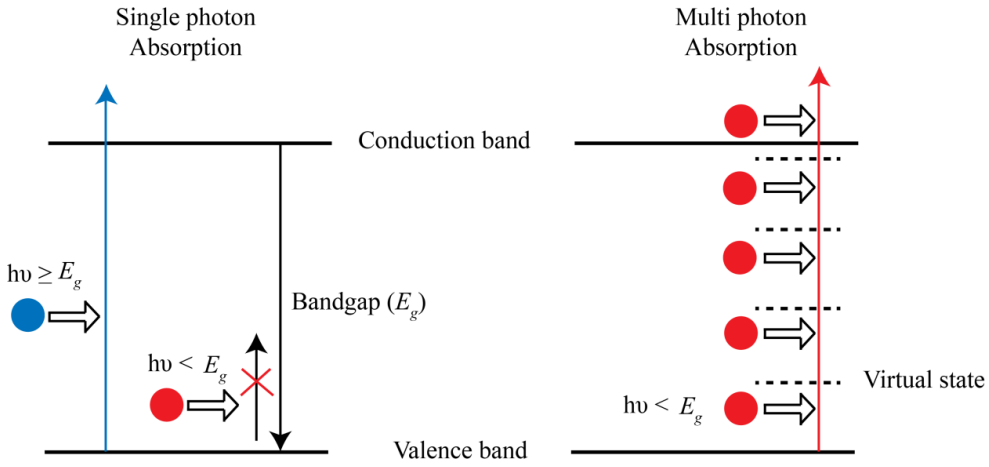

Fig. 2.13: Shows the comparison of single and multiphoton absorption [93].

The high-density photons required for this process can be achieved using femtosecond laser. The femtosecond laser beam can induce strong absorption even in transparent material due to nonlinear MPA. The MPA will be limited to focal region of the beam. By scanning position of focus, it is possible to fabricate 3D shapes with nm resolution.

The building block of 3D structure is volume pixel (VOXEL) [94]. The size of voxel depends on the focus of the laser beam. A high numerical aperture lens will give tighter focus inside the material with smaller propagation distance. 3D microstructure can be constructed by moving the focal position inside the material and overlapping multiple voxel close to each other.

Chapter 3

Methods and Measurement

3.1. Fabrication of photonic crystal using Bessel beam

The Photonic Crystal used in thesis has been fabricated by direct laser writing with femtosecond pulse having perfect Gaussian beam. The tight focusing is achieved using high numerical aperture (NA) microscope objective. Due to such tight focusing the achievable lengths of the PhC are limited, restricting the filtering range, since the angular range of the deflected components is related with the length of the PhC. Finally, one has to make a compromise in the fabrication procedure choosing between the use of high NA and short working distance or low NA and long working distance. This problem has been partially overcome and the quality of fabricated PhCs can be improved by using Bessel beams instead of Gaussian beams [95]. Bessel beams are well known in the study of nondiffracting solutions to Helmholtz's equation. The first experimental demonstration of Bessel beams using simple optical elements was reported by Durnin [96]. The advantage of Bessel beams with respect to Gaussian beams resides in its longer Rayleigh range, which allows fabricating longer length PhCs. The PhC used in our experiment were fabricated in Femtika (spin-off from Vilnius university Laser Research centre), Vilnius, Lithuania. Using Bessel beam different types of structure were fabricated [97-100].

The PhCs were fabricated using direct laser writing technique on N-BK7 (n=1.52) 4 mm thick substrates mounted on a 3D positioning stage. The Bessel beams were generated using an ultraviolet fused silica (UVFS) conical lens (axicon) with half angle $\alpha = 0.5°$

illuminated by a collimated incoming Gaussian beam with diameter of 5.3 mm at $1/e^2$. The central wavelength of the laser source is 1030 nm, the pulse repetition rate 25 kHz and the pulse duration approximately 200 fs delivering pulse energies of 8 µJ [101].

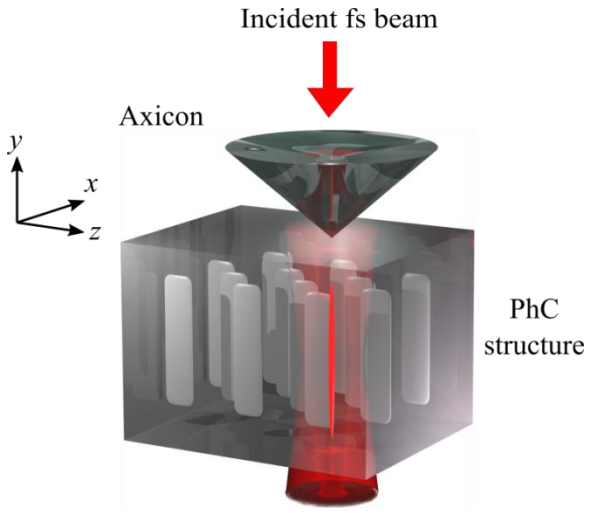

Fig. 3.1: Shows the scheme of fabrication of PhC by direct laser writing using Bessel beam. The incident femtosecond beam is nearly Gaussian beam.

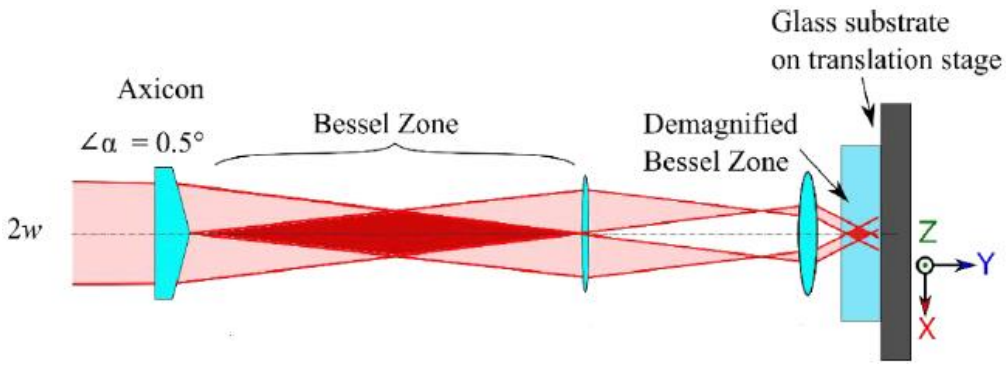

Fig. 3.2: Bessel beam generation for the fabrication process of photonic crystal using axicon and de-magnifying telescope.

Fig 3.2 sketches the experimental setup. The incoming Gaussian, incident on the axicon lens, generates a Bessel beam with a collimated zone of approximately 1.34 m. Two lenses of focal lengths 500 mm and 9 mm were used to reduce the beam diameter by a factor of 55.6 to obtain the Bessel beam incident on the sample [101-102]. After demagnification, the Bessel zone inside the substrate was around 600 µm. The sample was scanned using the 3D linear motion stages to produce the patterns. The fabricated structures were inspected transmission optical microscope.

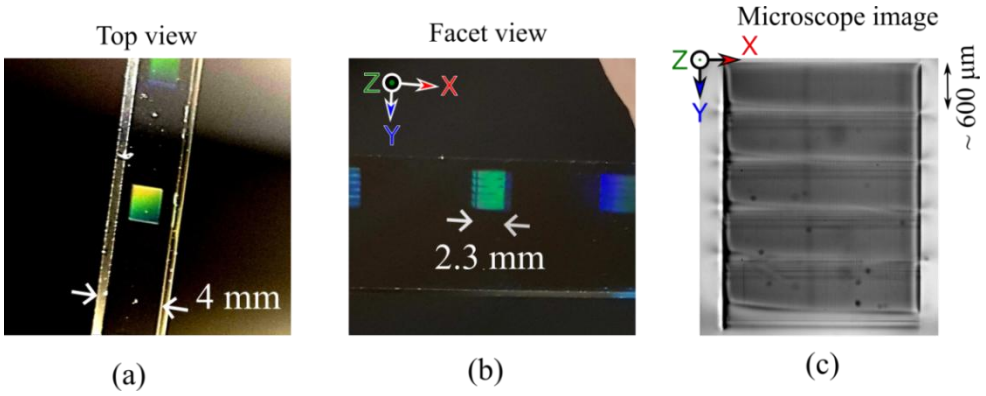

Fig. 3.3: Sample images of fabricated structure (a) Top view (b) Facet view (c) Microscope image

For the spatial filtering purpose, two PhCs were used with different parameters. The geometry of the fabricated structures is characterized by its longitudinal and transverse period (see fig. 3.4).

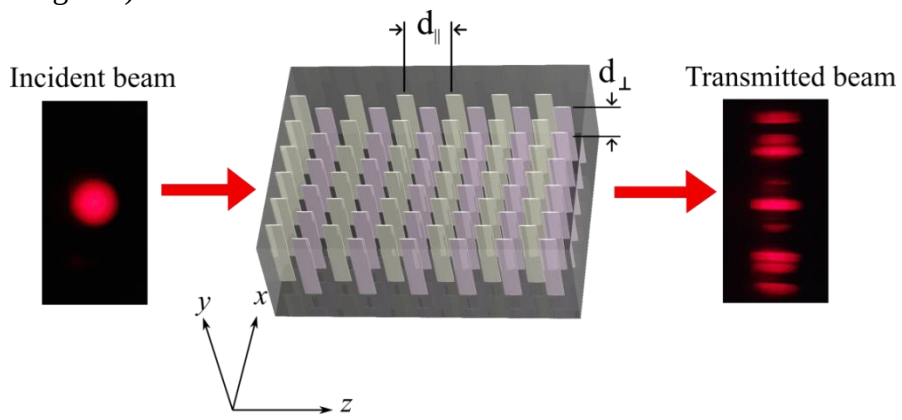

Fig. 3.4: Schematic representation of the photonic crystal structure showing transverse period ($d_{\perp}$) and longitudinal period ($d_{\parallel}$).

The first samples (sample 1) were fabricated with a transverse period of 3µm and with 80 longitudinal periods, N_p, with a linear chirp along the propagation direction in the range $1.15 \leq Q \leq 1.27$. Whereas, the second sample (sample 2) had similar transverse period while its chirp was varied along z-direction in the range $1.10 \leq Q \leq 1.60$, dQ =0.25 and $N_p = 60$. The parameter dQ is defined as the average of the minimum and the maximum value of the Q parameter in the structure.

The idea of PhC spatial filtering in single pass configuration is illustrated in fig. 3.4. The beam is incident on the sample from left side. The deflected higher order angular components of the beam depend on the periodicity of the structure.

3.2. Simulation of single pass through PhC

Let's assume a plane wave incident on the PhC grating at a given angle α. Its wave vector $\overrightarrow{k_0}$ is written as:

$$\overrightarrow{k_o} = k_x\hat{\imath} + k_z\hat{k} = |k_o|cos\alpha\hat{\imath} + |k_o|sin\alpha\hat{k}$$

The modulation of the refractive index in the PhC gives rise to the scattering of the incident wave. Since the index contrast is small, a paraxial model can be used to describe the scattering process and, under this assumption, we consider only the forward propagating wave components. The angles and the propagation vector inside the PhC are modified by the corresponding average refractive index. The forward scattering from the harmonic index modulation with transverse period d_x results in the coupling of the incident radiation to different diffraction modes. We will consider the coupling between three relevant diffracted beam components (first diffraction orders) with respective transverse wave vectors: $k_x - q_x$, k_x, $k_x + q_x$ where $q_x = 2\pi/d_x$ is the wave number of the index modulation in the transverse direction. The amplitude of the transmitted field is given by:

$$A(x,z) = e^{ik_{x,z}x}(A_0(z) + A_{-1}(z)e^{-iq_x x} + A_1(z)e^{iq_x x}) \tag{3.1}$$

The field component may be written in the form of column matrix

$$\vec{A}(z) = (A_{-1}, A_0, A_1)^T \tag{3.2}$$

The scattering matrix is given by equation (3.3). For simple case, we consider the scattering truncated to only three harmonic components. Here *S* denotes scattering, which can be related to modulation of refractive index. The details about the model can be found here [103].

$$\hat{S} = \begin{bmatrix} \frac{\cos(\sqrt{2s})+1}{2} & \frac{isin(\sqrt{2s})}{\sqrt{2}} & \frac{\cos(\sqrt{2s})-1}{2} \\ \frac{isin(\sqrt{2s})}{\sqrt{2}} & \cos(\sqrt{2s}) & \frac{isin(\sqrt{2s})}{\sqrt{2}} \\ \frac{\cos(\sqrt{2s})-1}{2} & \frac{isin(\sqrt{2s})}{\sqrt{2}} & \frac{\cos(\sqrt{2s})+1}{2} \end{bmatrix} \tag{3.3}$$

The free propagation between the scattering layers is consider by the simple paraxial propagation equation:

$$\partial_z A(x,z) = \frac{i}{2k_0}\frac{\partial^2}{\partial x^2}A(x,z) \tag{3.4}$$

Substituting equation (3.1) in to (3.4), we obtain that the free propagation between the gratings is described by diagonal propagation matrix:

$$\hat{P} = Diag(e^{-iL(k_x-q_x)^2}, e^{-iLk_x{}^2}, e^{-iL(k_x+q_x)^2}) \tag{3.5}$$

Here $L = d_z/(2k_0)$ is the normalized longitudinal period.

The field propagation along the whole phase mask is obtained by considering the propagation through all the layers in the grating, calculated by simply multiplying the scattering and propagation matrices.

$$\hat{T} = \hat{S}\hat{P}\hat{S}\hat{P}\hat{S}\hat{P} \ldots \hat{S}\hat{P}$$

The coupling co-efficient s depends on the modulation of the refractive index which is of the order of $\Delta n \sim 10^{-3}$.

Using this model, we calculated the far field profiles for the two fabricated PhCs described in the previous section (see section 3.1). The calculated profiles for these two samples are shown in fig. 3.5.

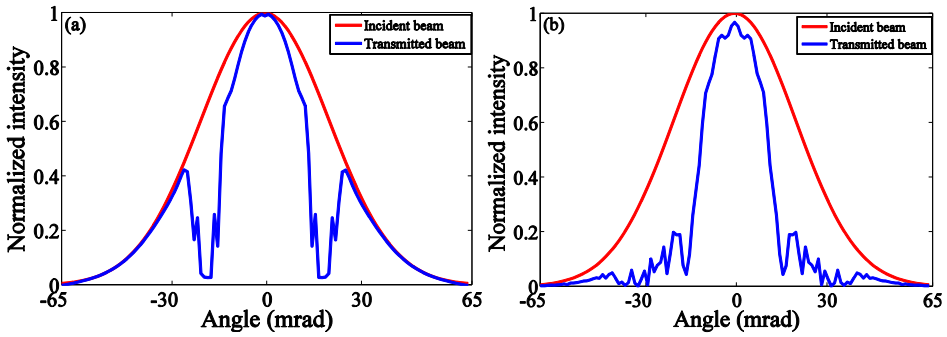

Fig. 3.5: Angular transmission profile for two different PhC: (a) sample 1 and (b) sample 2. The incident beam has Gaussian profile.

The sample 1 (fig. 3.5 (a)) and sample 2 (fig. 3.5 (b)) are chirped structure with. The parameter of these two samples is given in section 3.1. The parameters (Q, dQ, and N_p) of the PhC (sample 1 and sample 2) are the same as used in experimental case (see section 3.1). A more clear difference is seen in the filtering angle of these two structure. The figure 3.5 (b) has narrower profile because of higher chirp value compared to the profile shown in fig. 3.5 (a).

An increase in the efficiency of the spatial filtering in gapless (Laue) configuration is obtained by the use of chirped structures, where the longitudinal period varies along the photonic structure. By increasing the chirp, the filtering range in the angular spectrum can be shifted to smaller angles.

We further investigated numerically the dependence of the filtering performance with the chirp and the number of periods. In the first case, we fixed the number of periods to 60 and varied the chirp (dQ) of the structure from 0.05 to 0.35. By increasing the chirp, the angular range of the filtered-out components can be increased, as displayed in Figure 3.6.

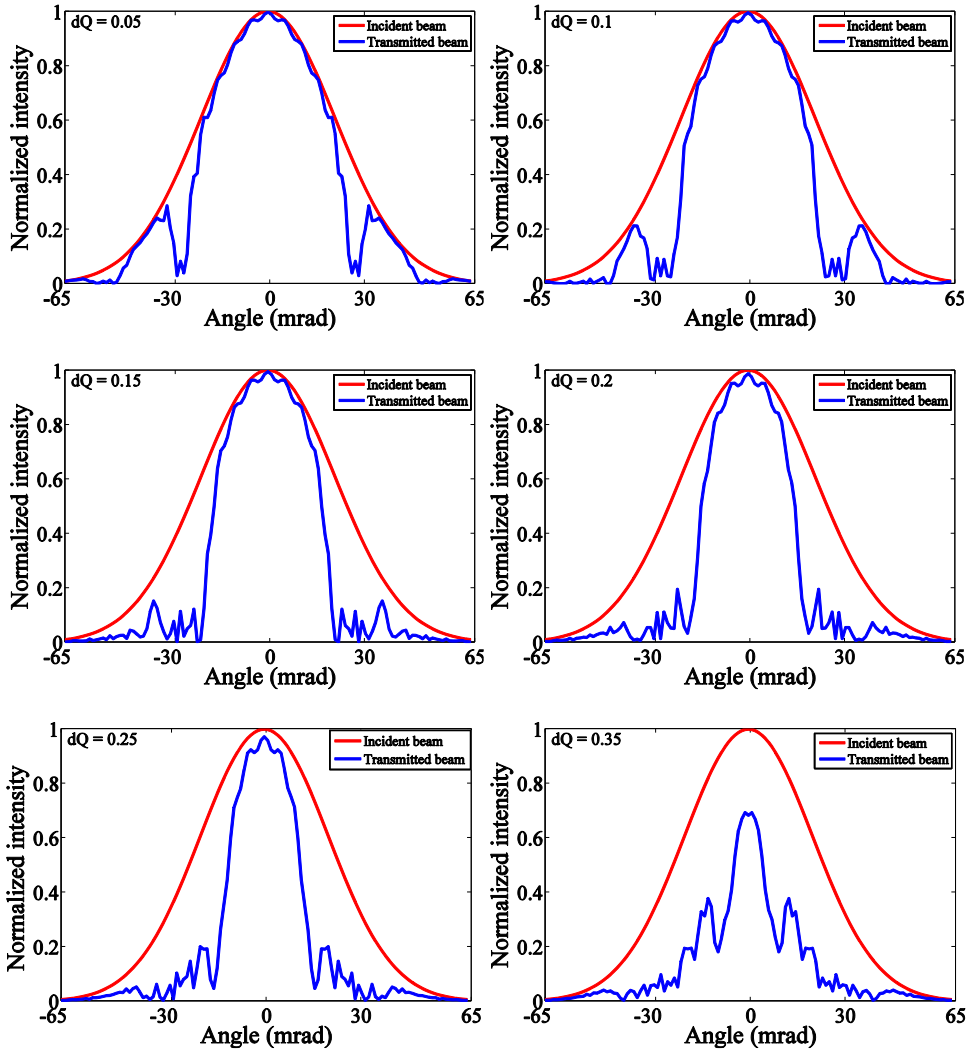

Fig. 3.6: The calculation of angular profile with incident Gaussian incident beam and transmitted beam for different chirp of the structure.

From Figure 3.6, it can be recognized that the introduction of chirp in the structure improves the spatial filtering significantly. The best filtering case is obtained at dQ=0.25, while at higher chirp values the filtering efficiency reduces since the central lobe is being affected by the filtering.

Another possibility to increase the filtering efficiency is by increasing the number of periods of the structure. In this case, we varied the number of periods (N_p) starting from 20 to 120. The Q parameter used here ranges from $1.10 \leq Q \leq 1.60$ and the chirp (dQ=0.25) used corresponds to the best value encountered from Figure 3.6. The angular transmission plots are shown in Figure 3.7.

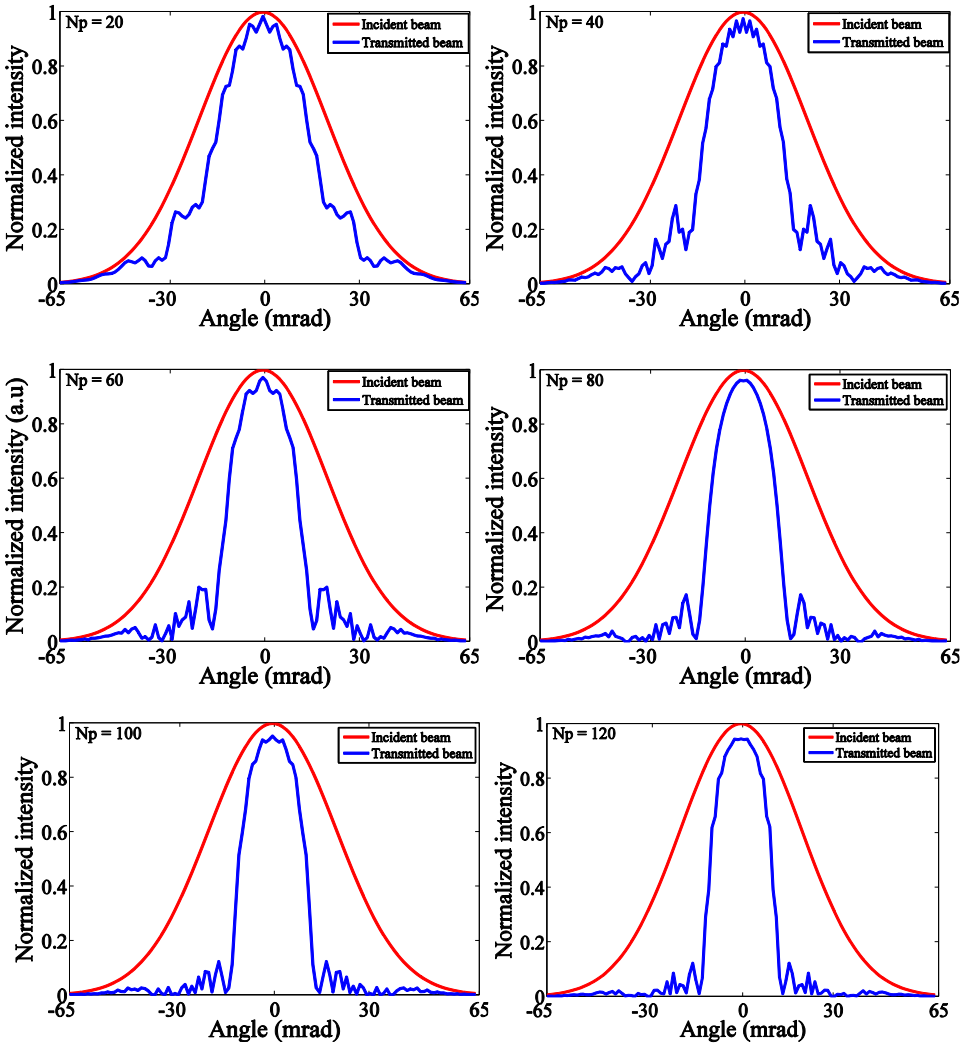

Fig. 3.7: Numerically obtained angular profile for incident Gaussian beam and transmitted beam for different number of longitudinal period (N_p).

As the number of period increases, the filtering performance increases. The effect of increasing the period is clearly seen in the transmitted profile (blue). Initially, at lower number of periods, the transmitted profile is broader and its width decreases with the increase in the number of periods. The filtering dips in the angular transmission get deeper with increasing the number of periods.

3.3. Numerical model of Edge emitting laser

In this section, we discuss the numerical model of semiconductor edge emitting laser. The results of spatial filtering obtained by using this model will be discussed in chapter 5.

The simulation of semiconductor laser diodes with optical feedback from an external cavity have been widely considered in the literature, particularly, the dynamics of the transversally single-mode narrow waveguides as developed by Lang and Kobayashi [104]. The detailed numerical modeling of a semiconductor lasers with a substantial width of the emission area, such as BASL lasers, supporting multiple optical modes, require in contrast the modeling of at least 1(time) + 2(space) dimensional partial differential equations resulting in a more complex task. In particular, the numerical simulation of chirped photonic crystals for the spatial filtering of broad-area lasers through optical feedback was performed by C. Bree and coworkers [105] indicating that spatially filtered reinjection enhances lower-order transversal optical modes in the laser diode and, consequently, improves the spatial beam quality.

In this thesis, we numerically simulate the edge-emitting laser by considering a simplified model in which thermal effects inside the cavity are neglected. The model includes only spatial-temporal evolution of field propagation inside the cavity and time evolution of the carriers given by equation (3.6) and (3.7) respectively. The edge-emitting lasers are generally described by stationary models for the electromagnetic fields and carriers [106], also by simplified mean field models including temporal evolution [107]. For a precise description, a complete model is use by solving Maxwell equation for the forward/backward fields propagating within the cavity, together with Bloch equations for the slow carrier's inversion [108]. We have developed a different approximation, by separating the field propagation in space, and slow variation of inversion in time [109]. The method is a simplification, taking advantage of different time scales of the optical field evolution (roundtrip is of the order of picoseconds) and relaxation of inversion life time (life time of carriers is in the order of nanosecond), therefore it is very fast comparing to complete model [106], and it has been proved it provides reasonable results for lasers and amplifiers [107].

$$\pm\frac{\partial A^{\pm}}{\partial z} = \frac{i}{2k_0 n}\frac{\partial^2 A^{\pm}}{\partial x^2} + s[(1-ih)N - (1+\alpha)]A^{\pm} \tag{3.6}$$

$$\frac{\partial N}{\partial t} = \gamma\big(-N-(N-1)\big)\,|A|^2 + p_0 + D\nabla^2 N \tag{3.7}$$

$$\text{where } |A|^2 = |A^+|^2 + |A^-|^2$$

The k_0 is the wave vector, n is the refractive, s is the interaction parameter inversely proportional to the light matter interaction length, h is the Henry factor related with linewidth enhancement factor of laser, α corresponds to losses, γ is the carrier relaxation rate, p_0 is the pump, and D is the carrier diffusion. The material polarization of the semiconductor is adiabatically eliminated, as usual for class B laser.

In our method, every integration step combines the field propagation in one-cavity round trip assuming constant carriers, and subsequently the temporal integration of carriers, considering constant field configuration. The electromagnetic fields are composed by the forward (A^+) and backward (A^-) fields; the two-dimensional distribution of carriers, *N*, evolves in time.

All physical laser parameters are similar to the experimentally used laser, and always assuming realistic values. However, the intrinsic parameters of the semiconductor material as matter-field interaction coefficients are different for each particular laser and become almost impossible to predict.

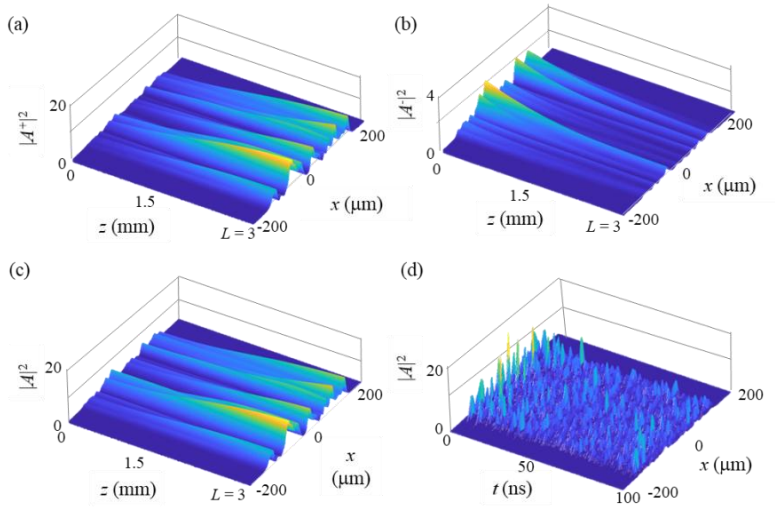

Fig. 3.8: Intensity of the fields within the laser for (a) forward field intensity, (b) backward field intensity, (c) total field and (d) temporal evolution of the output intensity.

The system of equations (3.6 and 3.7) is completed by the boundary conditions, where the field components, $A^+$and A^-, are related by the corresponding relations: $A^-(x, z = L, t) = r_L A^+(x, z = L, t)$; $A^+(x, z = 0, t) = r_0 A^-(x, z = 0, t)$ where L =1500 μm is the laser resonator length and r_0 and r_L are the corresponding reflection coefficients of the cavity mirrors at $z = 0$ and $z = L$ respectively, see Fig. 3.8. The delay of the fields in the feedback is not taken into account (as in Lang-Kobayashi

model [110]), due to slowness of the population inversion. Integration parameters used here are: p_0= 2.0, width = 400 μm, length = 1500 μm, α = 0.1 μm^{-1}, h = 2.0, s = 0.04 μm^{-1}, k_0 = 2πμm^{-1}, D = 0.03 cm^2/s and n = 3.

We preliminarily analyze an edge-emitting laser with the parameters corresponding to an experimentally used laser, as proof of the numerical model, before considering the PhC filtering effects. The laser is modeled by the system of equations (3.6) and (3.7), calculating a forward propagating field, i.e. A^+, see Fig. 3.8(a), a backward propagating field, i.e. A^-, Fig. 3.8(b), and a total field, i.e. A, see Fig. 3.8(c). The spatio-temporal integration exhibits both inhomogeneous and multimode spatial and unstable temporal behaviors (Fig. 3.8(c) and Fig. 3.8(d)). The sufficiently good agreement with the experiment results permits one to use the model for spatial-filtering simulation.

PhC simulation

To establish a comparison with our experimentally obtained results of spatial filtering described in the following chapters, we numerically investigated the action of the PhCs by introducing them in the numerical model of the edge emitting laser.

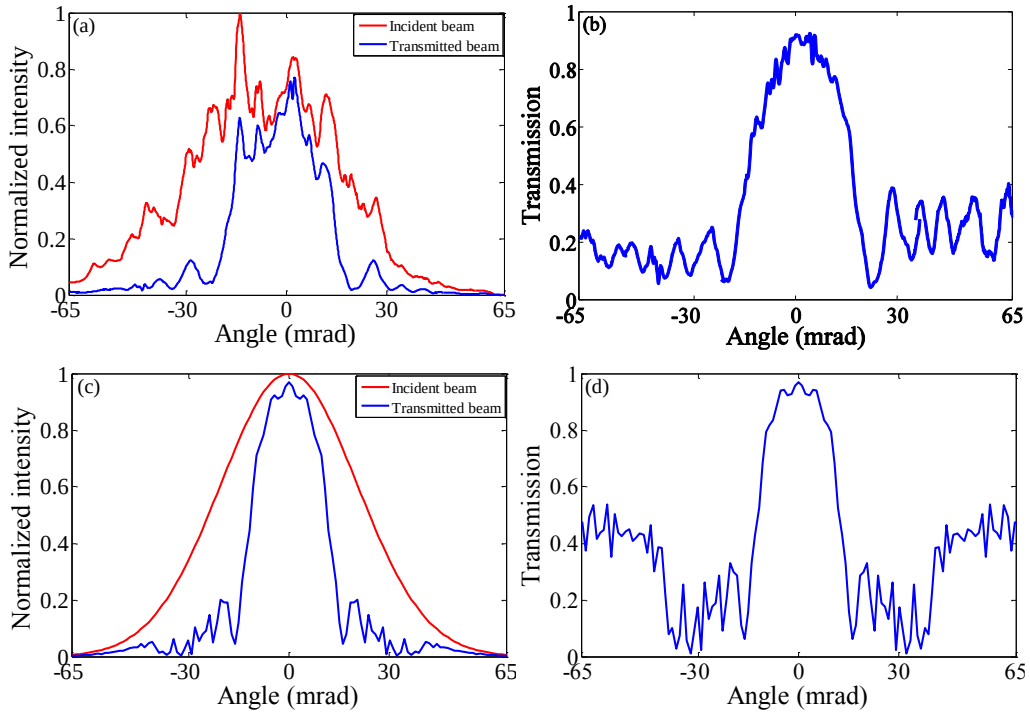

Fig. 3.9: (a) Experimentally single pass measurement and (b) corresponding transmission for sample 2 of PhC. The simulated profile for sample 2 (c) and the transmission obtained by dividing incident and transmitted beam (d).

The numerical and experimental results of spatial filtering using PhC will be discussed in the chapter 4. The PhC is introduced in the numerical simulation as a transmission function in the near field plane. The idea of placing the PhC in the near field is to demonstrate compact cavity situation. The transmission function is extracted from the experimentally obtained single pass transmission using the values of the sample 2 PhC by taking the ratio of the transmitted beam to the incident beam. This function is applied for both counter propagating fields (A^- and A^+) inside the cavity. This functions are shown in Figure 3.9.

3.4. Measurement of beam quality factor

The measurement and characterization of the beams is the most important aspect of this thesis. In this section, i will resume the methodology applied in the measurements that will be explained in the next chapters.

This section is dedicated to the characterization of the spatial quality of the beam. The beam quality is an important parameter in the performance of a laser in a wide range of practical applications, as well as a critical design parameter in optical beam trains and focusing systems. Since the beam profile is significantly affected during its propagation through space, it is important to analyze properly the beam characteristics.

The **beam quality** can be defined in different ways but normally it refers to a measure of how tightly a laser beam can be focused. In general, can be quantified through the measure of different parameters:

Beam parameter product (BPP): is the product of the beam radius at the beam waist times the far-field beam divergence angle.

M^2 factor: BPP of the beam divided by the corresponding BPP of a diffraction-limited Gaussian beam with the same wavelength.

Brightness: It is defined as power emitted per unit area per unit solid angle divergence of beam, and corresponds to the radiance defined in radiometric measurements.

The minimum focusing spot size that can be achieved with a given laser beam for a given divergence depends on the beam's M^2 factor. Lower M^2 factors correspond with a tighter focus, a more efficient use of the power within the beam, and a higher potential effective power of the laser. Focusing laser beams tightly is particularly important when you are using laser for imaging, because smaller beam waists mean that higher power densities can be reached, as well as better resolution.

Larger M^2 values means deviation from ideal Gaussian beam. In some laser sources, an increase in the output power can be accompanied by an increase in M^2 and a reduction of the beam quality due to higher order modes and thermal lensing inside the gain medium. In particular, some high-power lasers such as solid-state bulk or semiconductor lasers (diode bars for instance) can show values exceeding 100. This increase of the M^2 factor may be due to thermally induced wavefront distortions or to the emission in a multimode waveguide.

Measuring M^2 is not as simple as recording the beam profile at a single plane on the laser axis. A minimum of five beam diameter measurements must be taken at different positions along the optical axis in both the near field and the far field [43]. Moreover, the measurement of the beam size can depend strongly on the particular beam profiles of the source.

3.4.1. Beam Width Definitions

There are many definitions of the beam width or beam diameter [111]. The beam diameter must be well defined when one refers to circular cross-section beams or beams presenting non-circular symmetry having elliptical cross-section with respect to major or minor axes. The beam width definition used can have an effect on the way the beam width measurement must be conducted and it is important which definition should be used in terms of the application. The only beam profile for which a beam radius or diameter may be defined unambiguously is the top hat beam with a constant intensity distribution over the beam profile. Even in this case the top hat profile occurs only at the exit plane of the laser or at any conjugated plane obtained by a direct imaging of this plane. At any other position along the propagation axis, the beam profile will correspond to a beam shape modified by diffraction. For the top-hat beam the far field will adopt a $\mathrm{sinc}^2(x)$ profile.

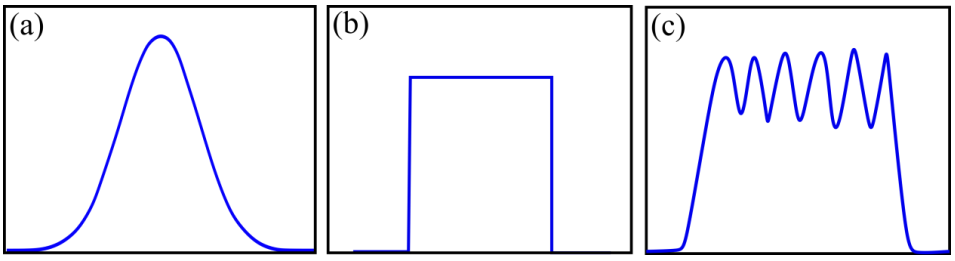

Fig. 3.10: Three different beam profile (a) Gaussian profile (b) top hat profile (c) multimode beam.

Most of the beams emitted by real sources may be approximated by mathematical solutions of the paraxial wave equation or Helmholtz's equation, such as Gaussian

beams, Laguerre-Gauss, Hermite-Gauss. These solutions are infinitely extended in the transverse plane, but a calculation of the power transmitted by a given aperture will show that most of its energy is concentrated within a circle of given radius. Consequently, for any real beam we could adopt a first definition of radius in terms of the radius of an aperture, placed perpendicular to the beam propagation direction, which collects a given % of the total beam energy. This definition could be useful for beams that have a smooth profile decaying from the beam axis and formed by a single peak.

For beams with more complicated transverse distributions, Laguerre or Hermite Gauss for instance, or with very large intensity oscillations, the establishment of a criterion to determine a radius is not easy. The adopted criterion to define a beam radius for any transverse distribution of our beam, $I(x,y)$, is the calculation of the second moment method of the beam [43].

3.4.2. Second moment method

The second moment beam width, also known as D4σ method, is defined as 4 times the standard deviation of the energy distribution of the beam evaluated in the transverse direction over the beam intensity profile [43]. Considering the propagation along the z-axis, and at any plane, the beam has intensity distribution $I(x,y)$, the beam diameter is defined as:

$$d_{\sigma x} = 4\,\sigma_x \qquad d_{\sigma y} = 4\,\sigma_y \tag{3.8}$$

Where d_σ- 4 sigma beam width.

$\sigma_{x,y}$ – standard deviation of the beam intensity.

$$\sigma_x^2 = \frac{\int_{\infty}^{-\infty}\int_{\infty}^{-\infty}(x-\overline{x})^2\ I(x,y)dxdy}{\int_{\infty}^{-\infty}\int_{\infty}^{-\infty} I(x,y)\ dxdy} \qquad \sigma_y^2 = \frac{\int_{\infty}^{-\infty}\int_{\infty}^{-\infty}(y-\overline{y})^2\ I(x,y)dxdy}{\int_{\infty}^{-\infty}\int_{\infty}^{-\infty} I(x,y)\ dxdy} \tag{3.9}$$

Where $\overline{x}$ and $\overline{y}$ are the coordinate of the centroid.

$$\overline{x} = \frac{\int_{\infty}^{-\infty}\int_{\infty}^{-\infty} x\, I(x,y)dxdy}{\int_{\infty}^{-\infty}\int_{\infty}^{-\infty} I(x,y)\ dxdy} \quad \overline{y} = \frac{\int_{\infty}^{-\infty}\int_{\infty}^{-\infty} y\, I(x,y)dxdy}{\int_{\infty}^{-\infty}\int_{\infty}^{-\infty} I(x,y)\ dxdy}$$

This definition could be implemented in principle for the determination of the diameter of any beam, irrespective of its beam profile distribution. For a perfect Gaussian beams:

$$I(x,y) = I_0 exp(-2(x^2+y^2)/w^2) \tag{3.10}$$

we can obtain analytically the value of the 4σ diameter to be $d_{4\sigma}=2w$, obtaining a BPP for the Gaussian beam: $BPP = \lambda/\pi$. This allows to obtain a general equation for the determination of the M^2-factor as:

$$M^2 = \frac{\pi}{\lambda} BPP_{beam} = \frac{\pi \cdot d_{4\sigma}^{beam} \cdot \Theta^{beam}}{4\lambda} \tag{3.11}$$

Where $d_{4\sigma}$ and Θ correspond to the diameter and total divergence angle of the beam.

Although this defines a well-established procedure to obtain the M^2-factor, we still have to face the problem of how to obtain experimentally the value of the $d_{4\sigma}$ for our beam. The technique, which has proved to be more satisfactory for the determination of beam widths is the knife-edge technique.

3.4.3. Knife-edge method

This method has been widely used for many years due to its simplicity. The knife-edge moves along the perpendicular direction of the laser beam and the output transmitted power is measured as a function of knife-edge position. This method is also called the 10-90 method, measuring the knife-edge position at the points where the power meter reads a value corresponding to 10% and 90% of the total power emitted by the beam. A scaling factor is used to convert the measured beam width to the 4σ diameter. The scale factor is given by $s = \frac{D_{10-90}}{\sigma}$. Where σ is the standard deviation of the beam in the knife-edge scanning direction [112]. Then the diameter of the beam can be expressed as $D = M.D_{10-90}$, where M is a multiplier factor. This factor in general will be different for different beam profiles, but for many beam types can be given by$M$=1.561.

In knife-edge method , the modal content of the beam is not known. The beam width is calculated by measuring the clip width and applying the corresponding scaling factor. This method is less accurate for higher multimode beam or complex beam profile due to the fact that large error in the standard deviation value could be obtained if the value of the multiplier factor used is far from that corresponding to that beam. For higher order transverse beams, the second order moment method is preferred [113].

M^2 measurement requires capturing several beam diameters along the propagation direction to properly measure the beam divergence and the beam waist diameter. Knife-edge method is usually performed manually, which requires many measurements at

every single plane. Nowadays, CCD camera is commonly used for measuring beam diameters. One advantage of cameras over mechanical scanning is that the software can quickly find the major and minor axis of an elliptical beam, and perform the measurement along these axes without having to actually reposition the mechanical device.

3.4.4. Considerations in M^2 Measurement

A number of factors in the characteristics of a camera used for beam profile measurement must be carefully considered and taken into account for accurately measuring beam widths. Among these considerations, the signal-to-noise ratio, i.e., the magnitude of the beam relative to the background noise in the camera must be well adjusted in the measurement. The amount of attenuation used for the camera is usually adjusted to enable the peak pixel in the camera to be as near to saturation as possible without overdriving the camera. In addition, if the beam is of a very small size in a very large field of camera pixels, this may be a very small amount of signal compared to the random noise of all the pixels. Because of low power, energy in the wings of a laser beam can have a strong impact on the width measurement [114]. Therefore, it is necessary to be able to characterize the noise in the wings of the beam. Both the noise components that are above and the noise components below the average noise in the baseline must be considered.

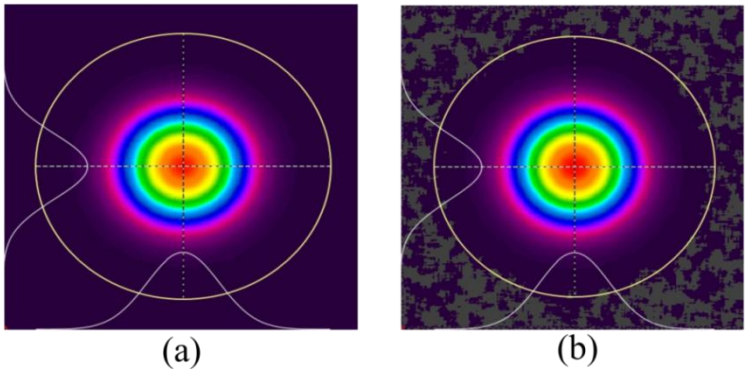

Fig. 3.11: shows the beam (a) before Ultracal and (b) after Ultracal.

The noise below the average baseline will hereafter be called negative noise. The software (BeamGage) used in the experiment performs the subtraction of background noise. The noise can be electrical and optical. The electrical noises are due to circuitry of camera and the optical noise can be due to ambient light. A calibration process called Ultracal is applied before acquiring the data in order to properly account for the background during the measurement. Ultracal uses sophisticated algorithms that

improve the accuracy over various operating conditions. The beam profile image with and without Ultracal process is shown in fig. 3.11.

3.4.5. CCD Camera

The camera used in the experiment is from Ophir (SP620U). The total number of pixels is 1600 x 1200 with a resolution of 4.4 µm with minimum dynamic range of 62 dB. The BeamGage software controls the camera with well-calibrated baseline correction algorithm "Ultracal". Before performing the beam profile measurement, Ultracal was applied to set the baseline to zero. An imaging system is used to image it onto CCD chip with a proper demagnification factor to make it fit inside the CCD detector area. This must be done in our case because the profiles to be recorded in the far-field are quite wide due to the large divergence of the semiconductor lasers. In our case a factor of 2.2 was used to properly image the real beam into the sensor. A number of neutral density filters were used to attenuate the beam and select the exposure level into the camera. To perform the measurements an aperture was selected to limit the noise outside the area of interest in making the beam measurement.

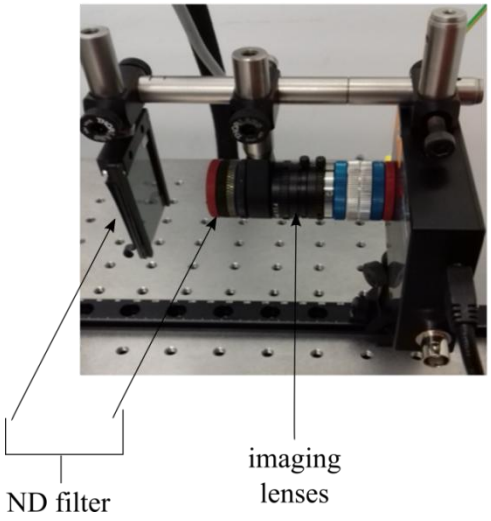

Fig. 3.12: Shows the complete camera setup used for M^2 measurement.

3.4.6. M^2 measurement

The emission from a BAS laser is characterized by its emission profiles along two perpendicular directions. The emission along the vertical direction (fast axis) is a single mode emission whereas along the horizontal axis it is multimode emission. To measure M^2, the output from the external cavity is focused using a 100 mm focal length. The external lens is used to generate a converging beam, which focuses to the beam waist and then expands in the far-field region in order to have access to different planes for

the measurement of the diameters. The beam caustic has a minimum width at the waist. The beam width is measured at different locations on either side of beam waist along the propagation axis.

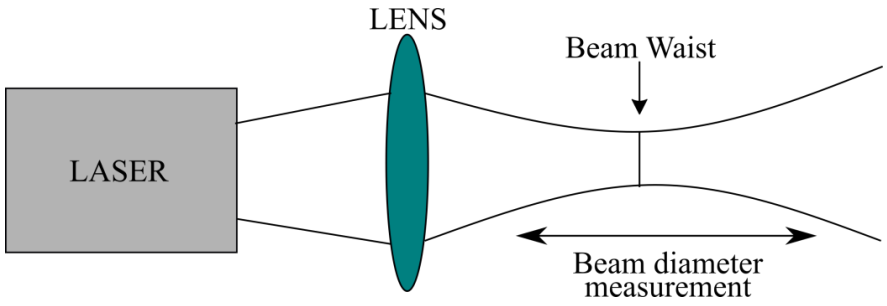

Fig. 3.13: Shows the schematic of beam focused by lens of focal length. The beam width is measured at location along propagation direction.

To accurately measure the beam width at the waist, minimum 5 intensity profiles were recorded and for each position the beam radius was determined according to what explained in the previous section. From the beam width vs propagation distance, the data were fitted with beam propagation equation.

$$w(z) = w_0\sqrt{1+\left(\frac{Z}{Z_R}\right)^2} \tag{3.12}$$

The M^2 value as function of wavelength is given by:

$$M^2 = \frac{\pi W^2}{4\lambda Z_R} \tag{3.13}$$

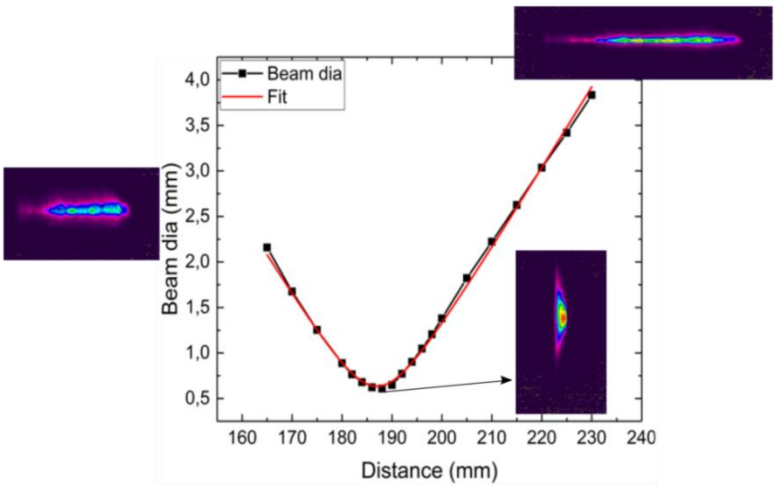

Fig. 3.14: Shows the beam caustic when focused by lens of focal length. The beam width is measured at different location along propagation direction and fitted beam waist equation.

From the fit, we can extract the value of M^2. This method due to large number of data points used reduces the relative error in the beam width which improves the accuracy. The M^2 along both axes can be determined using this method. Three different profiles of the beam are shown in the inset of fig. 3.14. Two profiles are shown at the far field plane and one at minimum diameter. The results of M^2 along the slow axis are discussed in section 4.3.5 of chapter 4.

Apart from this method, beam propagation factor (M^2) can be determined using a single measurement of the minimum beam width (W) achieved after focusing the beam and the divergence angle (Θ), and applying equation 18 [42-43]. The divergence angle can be measured with a single measurement by using a lens of known focal length since the ratio of the beam width at this plane to the focal length gives good approximation of the divergence angle. This method would allow to measure M^2 from two single measurements: at the focal plane and at the beam waist plane. However, this method can give erroneous results due the difficulty in properly determining both planes. In fact, to obtain the smallest beam radius, at least three measurements around the beam waist are recommended [115], while a single measurement would be enough to determine the divergence if the focal plane is well known.

Chapter 4

Extended cavity setup

Introduction

The single-spatial mode diode laser offers high beam quality, but the output power from such laser is restricted to hundreds of mW due to catastrophic optical mirror damage (COMD). This problem is overcome by increasing the width of the active region to hundreds of microns obtaining higher output powers of few watts. By arranging the laser emitters in the form of bar and stacks, output power of the order of kW can be achieved. With increasing width along the lateral direction (slow axis), the beam quality deteriorates due to multi transverse mode oscillations. In their typical configuration these lasers show a good beam quality along the fast axis since the radiation emitted along this direction is diffraction-limited, the only possibility is to improve the beam quality in the slow axis.

The main goal of the project initiated with this thesis is the achievement of a significant improvement of the beam quality of the radiation emitted by BAS lasers using a filtering mechanism integrated in a compact monolithic implementation. To this end, our motivation is to test the possibility of using PhCs for this purpose. Due to its compact size, PhCs are good candidates to be used for applications in micro-optical devices or inside the resonators of micro-lasers. The successful demonstration of PhC spatial filtering could lead to a future design in a monolithic implementation. However,

testing the performance of the PhCs and their filtering effect requires an experimental setup where different crystals or filtering techniques can be studied and compared.

In this chapter, we will introduce our approach using an extended cavity configuration, which mimics the ideal compact cavity case, but provides the possibility of experimental validation. An external cavity diode laser consists of an AR coated laser diode, a collimating lens, and an external mirror to provide the feedback to the laser. The feedback strength depends on factors such as the reflected power, the cavity length, and phase of the reflected light.

This chapter describes our approach to obtain the spatial filtering of BAS lasers in external cavity configuration including the description of the experimental setup of the extended cavity. The observed increase in laser brightness supports by first time a physical proof of principle of the filtering effect of PhCs in such kind of lasers. Moreover, the results of PhC filtering are compared with those obtained using the more traditional intracavity slit method. The results of this chapter have been published in [36]. In first place, we will introduce the general description of the spatial filtering in a conventional confocal arrangement. Being one of the simpler methods to obtain spatial filtering and one of the most extended in several configurations, its study will provide a direct way to compare the results obtained with the ones obtained using PhCs although the confocal arrangement offers serious limitations in terms of its size and is not suitable for its implementation in a compact cavity configuration.

4.1. Spatial filtering schemes

4.1.1. Conventional spatial filtering

Beams emitted from He-Ne, CO2, and single mode fiber laser possess a high spatial quality with M^2 factors approaching 1. Solid-state lasers, on the other hand, have poor beam quality due to thermal effects inside the gain medium or their multi-mode emission. High spatial quality beams are required for many applications such as laser material processing (marking, cutting, drilling etc), Interferometric metrology, non-linear frequency conversion [116] or medical applications.

Spatial filtering is a process of cleaning the laser beam to improve its spatial quality. As the beam passes through the different optical elements, its wave fronts are distorted due to the presence of dust, damage in the optics, variation in the refractive index of the medium and diffraction effects. All these distortions appear in the form of ripples or noise added to the smooth profile of the beam. If we represent the beam in the spatial frequency domain (far-field), we will observe that most of these variations are impressed in the high spatial frequency content of the beam. The simplest way to clean our beam should be, then, to apply a band pass filter in the frequency domain cutting the

larger frequencies. This can be easily achieved by passing the beam through a lens and inserting a pinhole in its focal plane, where the Fourier plane is located. In this way, we can remove the noise present in the higher frequency components of the beam leaving only the central part of the spectrum and creating a smooth profile.

The quality of the filtering depends on the diameter of the pinhole. Smaller the pinhole, better the beam quality, but with reduction in output power. This technique is also used to remove higher order transverse mode emission in the laser cavity.

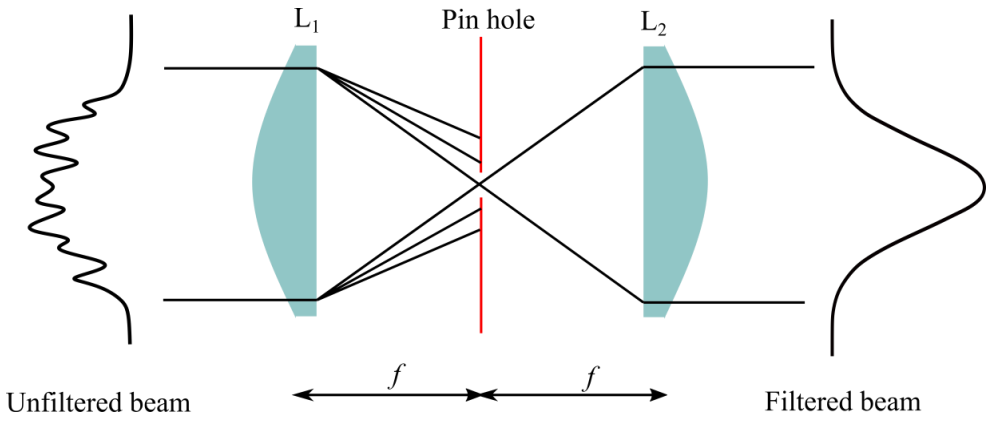

Fig. 4.1: Shows the conventional spatial filtering using confocal arrangement with two lenses. At the output of first lens (L_1), all the higher angular components of the beam are blocked using pinhole.

The conventional spatial filtering technique in confocal configuration consists of two lenses and a pinhole or iris. The scheme of confocal spatial filtering is shown in fig. 4.1. The pinhole is placed at the focal plane of the first lens, the Fourier plane. Each spatial Fourier component corresponds to a plane wave with a certain propagation direction, which is focused at a different position in this plane. The relation between points in the plane and spatial frequencies is given by the simple relation:

$$(f_x, f_y) = (\frac{x}{\lambda f}, \frac{y}{\lambda f})$$

Therefore, the pinhole diameter defines which frequencies will be filtered out. The second lens recollimates the beam transmitted through the pinhole, and the resulting beam has a cleaned intensity and phase profile [117]. The disadvantage of such system is its relatively large size since typical arrangements use two microscope objectives and pinholes with diameters of the order of few microns leading to spatial extensions of few centimeters.

When the aperture is sufficiently small, only the lowest-order transverse mode of a laser beam will lase. Generally, spatial filtering outside the laser cavity increases the spatial quality of the emission, but then the total power reduces linearly with the number of

transverse modes, assuming all modes have equal power. Such spatial filtering outside the laser results in a much lower efficiency compared to the case where the filtering is performed inside a cavity. For the case of micro-lasers such as microchip or semiconductor lasers, the length of the resonator is of few millimeters and, therefore such filtering technique is not convenient and impossible to implement due to bulky size of the lenses.

The improvement of the beam quality of the multimode lasers we are using in this thesis is not directly linked to the goal of achieving a perfect smooth Gaussian beam profile of the slow axis emission since this would result in an impermissible loss of the output emission power. The improvement in the beam quality in these lasers is more related to the decrease in their beam divergence and a consequent reduction of the M^2 factor, which is related to an improved far-field emission profile of our laser. In the next section, we discuss the proposed PhC spatial filter in compact cavity configuration. In the section 4.3, we will describe in detail the experimental setup of extended cavity configuration. In the same section will discuss the characterization of extended cavity by measuring its output power, spectrum, and profile in the near/field. In the last section of this chapter we discuss about the spatial filtering using intracavity slit and PhC.

4.1.2. Photonic crystal in compact cavity scheme

The advantage of PhC spatial filtering compared to the conventional confocal arrangement is its extremely small size, which allows integration of such filter in micro-optical devices or inside the resonators in microlasers [118]. PhCs could be integrated inside the laser cavity between the front facet and the cavity mirror leading to the extremely compact cavity configuration shown in fig. 4.2. The successful demonstration of the filtering action by PhCs in this scheme could lead to a very compact device with optimized beam quality.

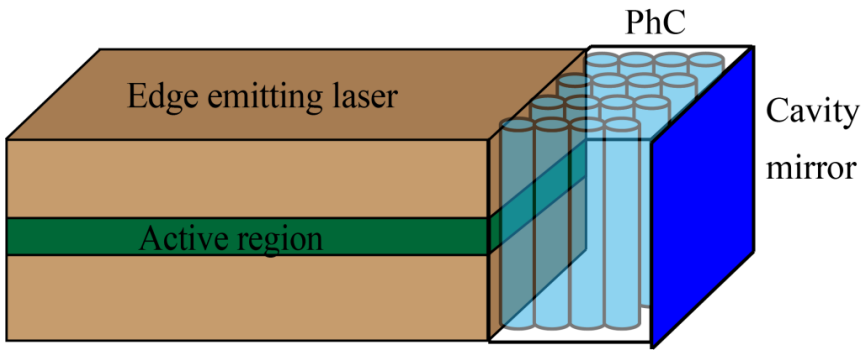

Fig. 4.2: Shows the scheme of compact cavity configuration in which PhC filter is place between front facet and cavity mirror.

In this integrated configuration, the PhC placed at the same plane of the exit facet and cavity mirror, acts on the near-field of the emitted beam. To have the possibility of testing different crystals and compare with other filtering techniques we need to make accessible these planes. Our proposed solution is to use an extended cavity, which mimics the action of compact cavity, allowing to place the PhC in an accessible near-field plane. The added advantage of the extended cavity is that it will allow to test the action of the filtering by a slit in the same setup.

An external cavity (EC) allows to spatially and spectrally control the feedback acting on a diode laser compared to its own feedback from its facet. In our situation, we are not looking to this situation since we want to filter the lasing modes acting inside the laser cavity. To construct an extended cavity, the first step is to eliminate the reflection from the output facet of the semiconductor material to prevent lasing from the gain medium itself. This can be obtained by coating the facet with an antireflection layer. The simplest implementation of an extended cavity configuration is to use a collimating lens and mirror. However, we will use another configuration, which will be useful to test different filtering schemes in the same cavity as explained in the next section.

4.2. Extended cavity setup

4.2.1. 4*f* optical system

The PhC as spatial filter works only in near field plane. In our case, this plane is located at the exit facet of the semiconductor. The beam emitted from our broad area laser has a large divergence angle in the fast axis (typical 40° FWHM). To efficiently capture all the radiation, the beam is collimated along fast axis using a micro lens placed very close to the facet of the laser. Since this precludes the possibility of placing the PhC directly at the output facet of the semiconductor as desired, we need a way to access the near-field plane.

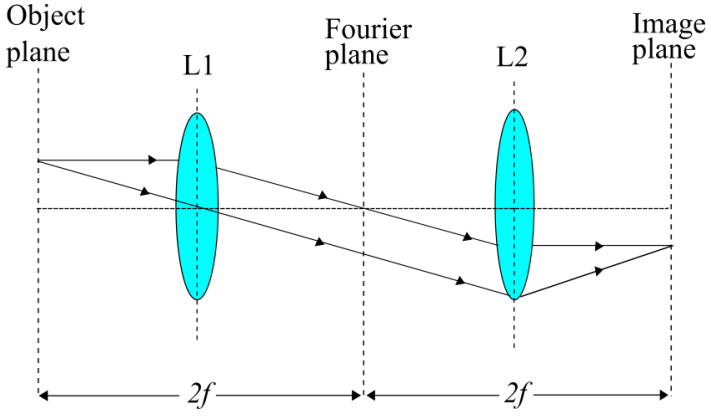

Fig. 4.3: Schematic of 4*f* optical system.

For this purpose, we employed a 4-*f* optical system, which allows us to recreate the near field plane at the conjugated image plane as shown in Fig. 4.3. The 4-*f* imaging system consists of two lenses placed along the optical axis and separated by a distance of 2*f* between them. The Fourier plane is located at the back focal length of the first lens and the image is located at the focus of the second lens. Since, both lenses have equal focal length, the distance between the object and the image is 4*f*. With this configuration, we can insert our PhC at the image plane, where the beam wavefront will be overlapped in amplitude, and phase to that of the object plane. Now to complete the laser cavity, we need to place the laser cavity mirror. One possibility should be to place this mirror attached to the PhC crystal in the same plane.

4.2.2. Experimental setup

In this work, we implement a double 4*f* system creating a second conjugate plane of the exit facet of semiconductor laser, where the external cavity mirror will be placed. The advantage of this configuration is that we have access to the Fourier plane, where we can act on the far-field components of the laser. In this way we can also study the effect of slit filtering (acting in the far-field) in the same setup to make a comparison with the PhC filtering (acting in the near-field). The schematic representation of our extended cavity setup is shown in Figure 4.4.

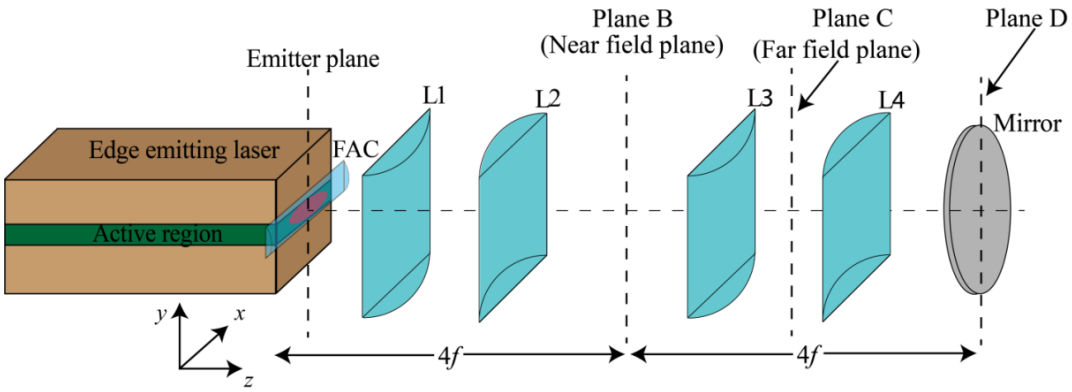

Fig. 4.4: Schematic of extended cavity setup for spatial filtering using broad area semiconductor laser.

In this self-imaging cavity, each ray with arbitrary position and arbitrary angle with respect to the optical axis returns back to the same position after one round trip. As a result, every ray has the same optical length in one round-trip in the resonator and the superposition of the modes of the resonator gives the field distribution inside the cavity. Next, we will discuss in detail the characteristics of the setup. Our cavity consists of a single emitter BAS laser mounted on C-mount package structure (Fig. 4.5). The C-mount is highly desired when other optical components need to be in very close

proximity to the front facet. C-mount contains four main parts: cathode, a ceramic slice, a laser chip, and a mounting substrate, which also acts as the anode. The hole in the mounting substrate is designed to fix the C-mount to an installation platform. The ceramic slice is used to insulate the cathode from the anode. The mount acts as a material with high heat conductivity, which effectively extracts heat from semiconductor chip. Even though the C-mount is a very good heat sink, additional water-cooling will be required for best performance. The whole C-mount is assemble inside a mechanical housing assembly with active water-cooling at 18° C as shown in Fig. 4.6.

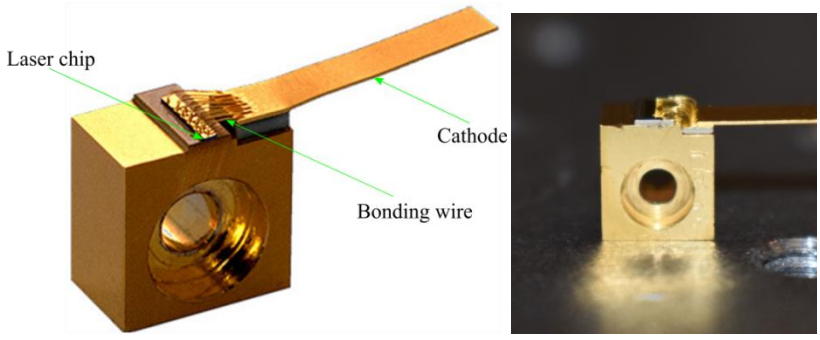

(a) (b)

Fig. 4.5: (a) Typical C-mount laser diode package structure (b) photograph of c-mount structure in the lab.

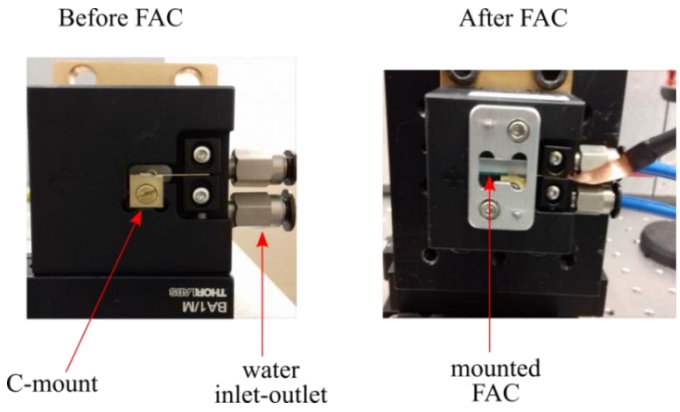

Fig. 4.6: Before and after mounting of FAC lens.

In typical BAS lasers the high reflectivity of the polished front and back facets of the gain medium act as the laser resonator. In our case the laser is modified to construct the extended cavity so the reflectivity of the back facet is 95% while the front facet has been AR coated to obtain R< 0.01%. The transverse width of our laser is of 400 μm and the active length is 1.5 mm, operating at a central wavelength of 970 nm. The output

beam has larger divergence along the transverse direction (fast axis) so it needs to be first collimated in this direction. A fast axis collimator (FAC) micro lens with focal length of 0.59 mm and numerical aperture (NA) of 0.8 is used for this purpose and placed directly in the laser mount as shown in Fig. 4.6.

After collimation, the beam divergence is reduced to less than 1° in the vertical (fast) axis. The beam along the lateral direction (slow axis) is multimode, its emission profile shown in Fig. 4.7 (a), where the direct light (spontaneous emission) without any feedback mirror is observed on the IR card. As we can observe, the emission is quite broad along the lateral direction. This fact imposes a first limitation in the selection of the optics of our setup since we must use large aperture lenses with short enough focal lengths to capture the full radiation along the lateral direction.

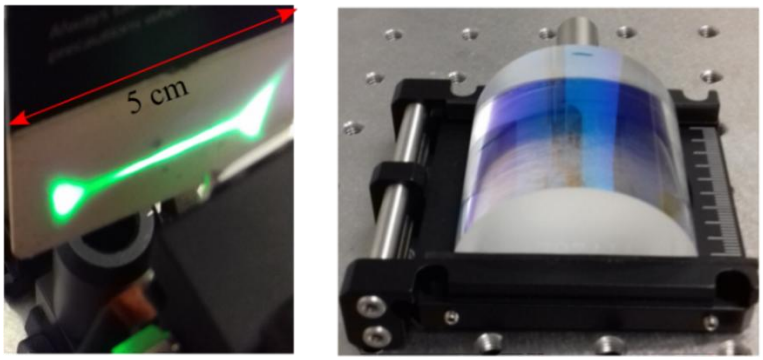

Fig. 4.7: (a) direct emission on the IR card and (b) cylindrical lens used in the experiment.

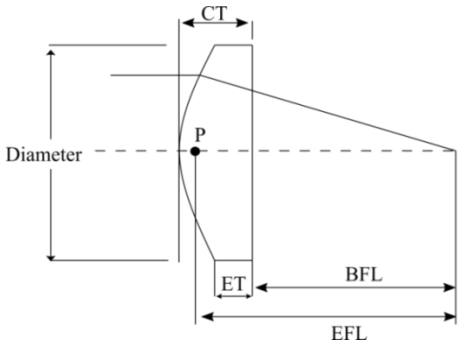

Fig. 4.8: Shows the schematic of the lens. The point "P" indicates the principle plane, ET is the edge thickness, CT is center thickness, BFL is back focal length, and EFL is the effective focal length.

Four cylindrical lenses of equal dimension and equal focal length (51.97 mm), acting on the lateral direction, were used to create the double conjugate plane scheme with magnification of 1:1. In this way, the field distribution at the output facet (emitter plane

in figure 4.4) was reproduced in the planes B and D shown in figure 4.4. The separation of the lenses was obtained from the position of their principal planes and its refractive index at the emission wavelength. It was checked by direct imaging using CCD that the field in the emitter plane was properly recreated in planes B and D.

The laser cavity mirror is placed in the conjugate plane (D in figure 4.4.) to complete the laser resonator. The reflectivity of the mirror was selected to be 4 % in this first configuration. All the lenses used in the setup and the non-reflecting side of the cavity mirror had a broadband AR coated in NIR to avoid multiple cavity formation.

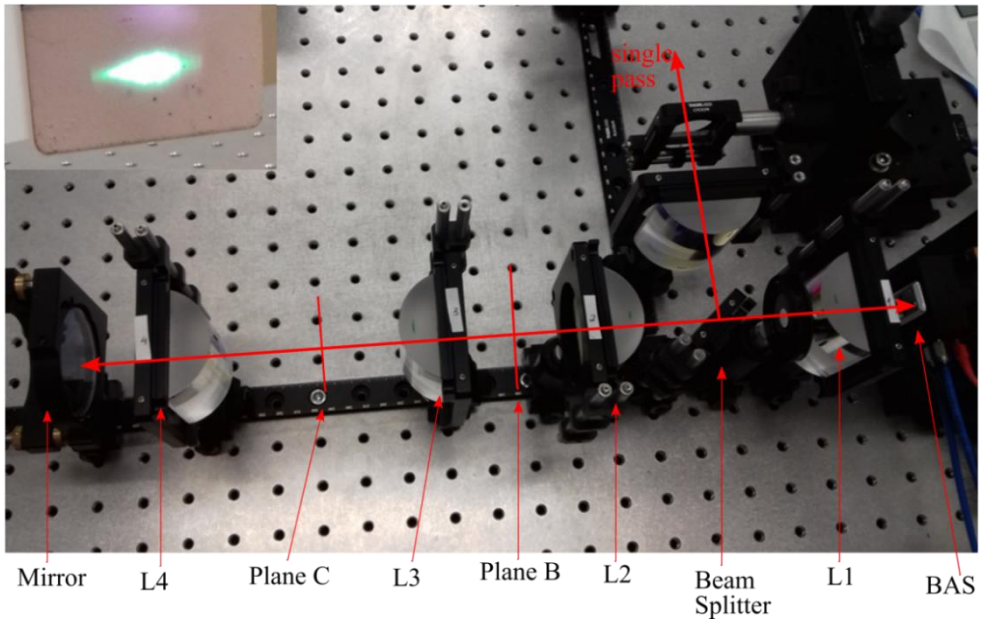

Fig. 4.9: Experimental setup of extended cavity.

The mounted setup is shown in figure 4.9, conforming an extended cavity. We used cylindrical lenses of width 50.8 mm, length of 53 mm and focal length 51.97 mm to capture the full beam emission and avoid unnecessary power losses, which would lead to an erroneous estimation of the brightness. The inset in top left corner of figure 4.9 shows the output lasing beam visualized on IR card at a distance of 10 cm from the output mirror.

This basic configuration will allow different measurements in our system. Plane B is a convenient near-field plane where the PhCs can be inserted for filtering tests; at the same time, we have also access to the far-field (plane C) to insert a slit and test the conventional spatial filtering of the beam. Additional measurements can be made in this configuration by placing a beam splitter as indicated to obtain information of the distribution of the field inside the cavity or to test the filtering effect of the PhC in single pass configuration.

4.3. System characterization

4.3.1. Mode of operation

The laser current was mostly driven in quasi-continuous mode (QCW) with pulse width of 5 ms and period of 20 ms giving a repetition rate of 50 Hz. The duty cycle, given by the ratio of pulse width to period expressed in %, indicates the percentage over a period for which the laser is in ON state. A duty cycle of 25% was used throughout the experiment in order to work with smaller output powers to protect some of the detectors in our characterization setup, to increase the lifetime of the emitter and avoid unnecessary overheating. The emitter was characterized by measuring the optical power, output spectrum and the power-dependent beam profile along the lateral direction (slow axis).

4.3.2. Output optical power and Spectrum

The emission from the extended cavity system was characterized in different aspects. The laser emission curve, measured both in CW and in pulsed mode, is represented in figure 4.10 (a) and (b) respectively, showing a threshold injection current of 1.3 A for laser emission.

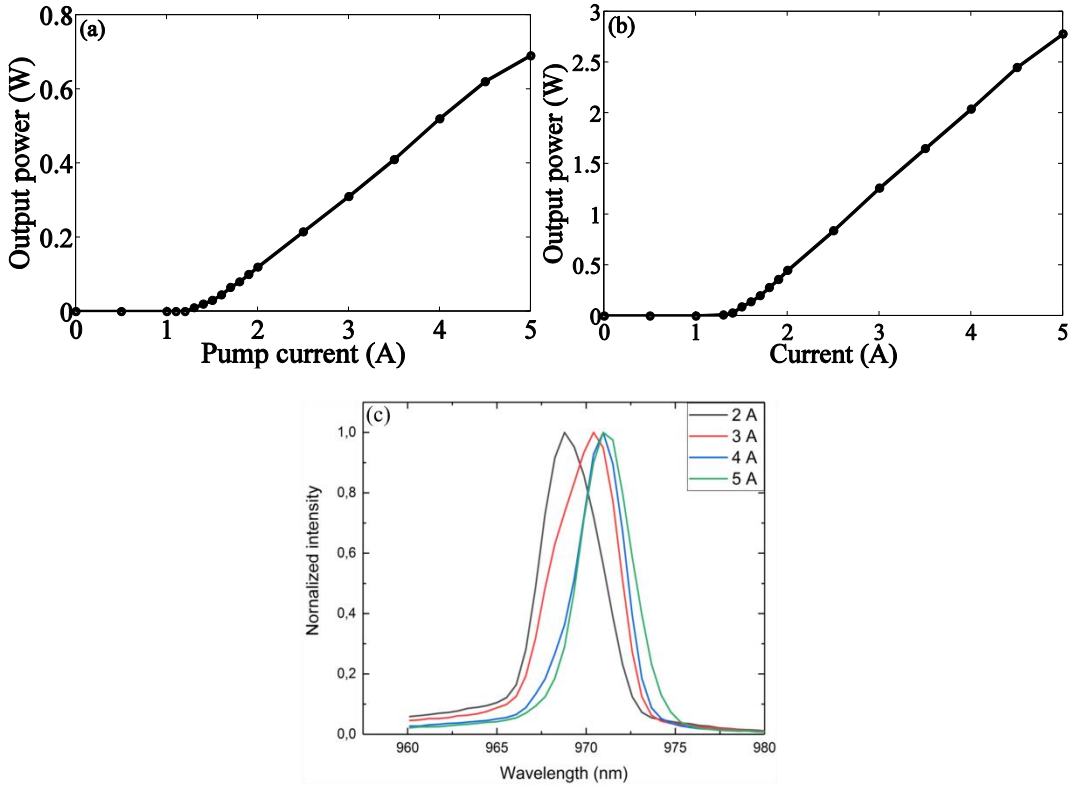

Fig. 4.10: Power-current curve measured at the output of external cavity (a) in pulse mode (b) in CW mode. (c) Spectrum for varying pump current.

The output power in the pulsed mode is reduced by 25% according to the duty cycle selected and the coincidence of both curves will allow us to make all measurements in the pulsed mode. The total emitted power in CW emission is close to 3W at an injection current of 5A. In this thesis, the values of optical power measured will correspond to pulse mode operation unless explicitly mentioned and, hence, a factor of 4 should be applied to obtain the total power emitted in CW operation.

The frequency spectrum of the external cavity, measured at different injection currents is represented in figure 4.10 (c) showing a red shift for larger injection currents. The monitoring of this spectrum allows to control the semiconductor laser temperature and to avoid overheating which could damage the laser. The central wavelength lies close to 970 nm at 3 A pump current.

4.3.3. Vertical (Fast axis) emission

The emission along the fast axis is close to single-mode because the beam is tightly guided in this direction by the waveguide structure in the epitaxial layer with a thickness of few microns. Diffraction from such a narrow aperture results in a beam emitted with a large angular divergence of the order of 40° (due to this large divergence angle, this is also called the fast axis direction). Because of this large divergence angle in this direction, the output light from the laser cannot be used efficiently unless it is collimated by placing a cylindrical lens of very short focal length at the output of the semiconductor material. Due to the single-mode emission along this axis, a close to diffraction-limited beam with M^2 close to 1 is obtained.

For our system, the cylindrical lens used was mounted directly on the C-mount of the laser as shown in figure 4.6. The measurement of the M^2 factor of the beam along this direction gives a value of M_y^2 =3.3. This value is slightly larger than expected most probably due to a slight misalignment of the lens with respect to the emission region. With increasing pump current, there was slight increase in M_y^2 value.

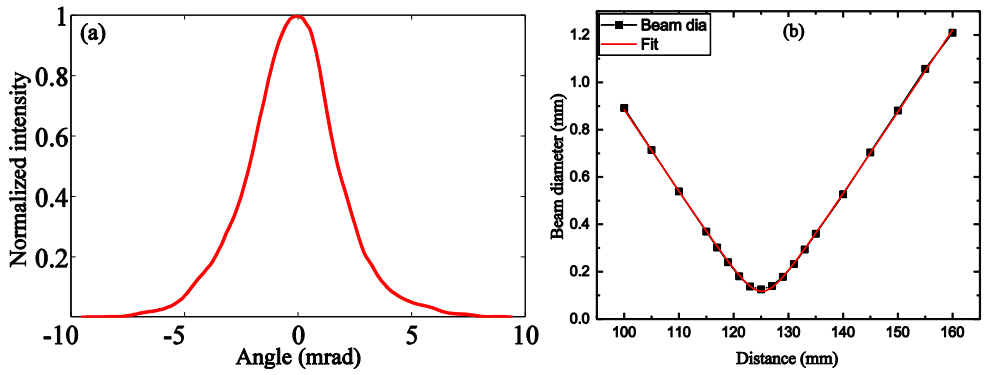

Fig. 4.11: (a) shows the profile along the fast axis and (b) the corresponding M_y^2 measurement.

4.3.4. Horizontal (Slow axis) emission

The beam formation along the lateral direction is driven by gain guiding due to the large width of the active region or index guiding along the junction plane. The beam profile along this direction is dependent on the injection current, since an increase of the injection current induces higher order mode oscillations.

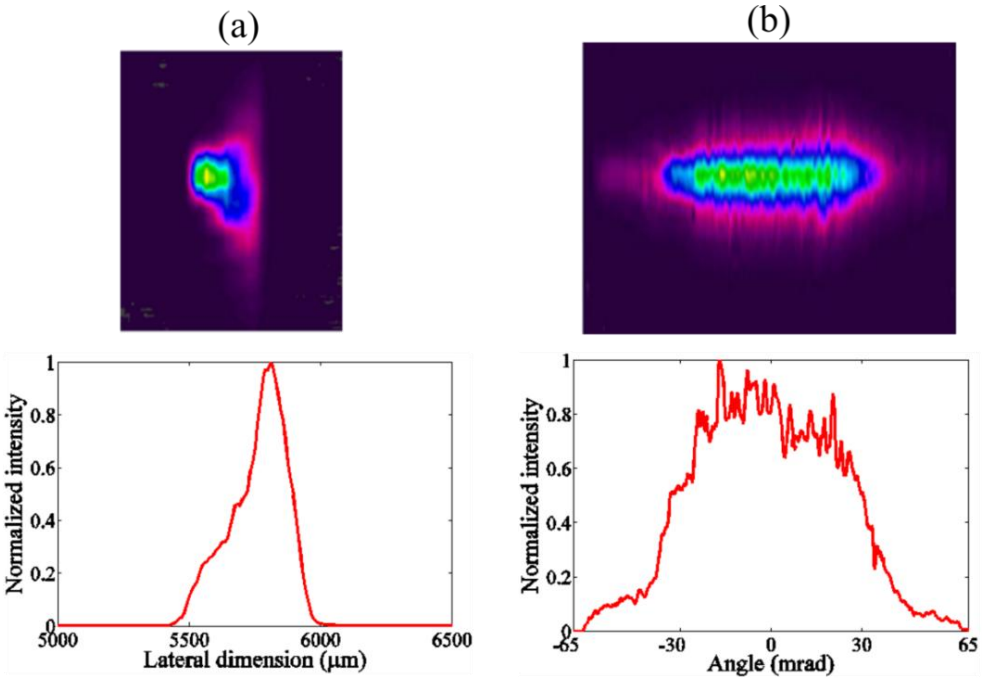

Fig. 4.12: Transverse field distribution in the (a) near-field plane and (b) in far-field plane.

With increasing output power, other non-linear effects start to develop such as filamentation, spatial hole burning and transverse mode instability [119-121]. All these effects degrade the beam quality resulting in an increase of the M_x^2 factor.

To characterize the beam quality along the slow axis, beam profiles were measured with the CCD. The near-field profile at the output of the cavity mirror (image of the field at the facet of semiconductor laser) and the far-field profile, measured outside the cavity at a distance far from the cavity mirror or at the focal plane of an external lens, are shown in figure 4.12 at injection current of 3A. The spatial profiles of the extended cavity with BAS emitter shows poor beam quality with an asymmetric beam profile in the near-field. To obtain higher output power, the width along the lateral direction is increased. Such elongated width waveguide can support large transverse modes. The far-field beam profile along the slow axis increases its width to support the larger number of modes as we increase the injection current.

4.3.5. Effect of pump current on spatial profiles

Below the threshold current, the light emitted from diode laser is spontaneous emission. At threshold current and above, the output power increases rapidly with increase in pump current and the far field emission is very sensitive to the alignment of the feedback mirror. As the pump current is increased, the spatial profile in the far field also changes due to excitation of higher order transverse modes. In this section, we show how the spatial profile is changed with increasing the pump current when a 4% reflectivity mirror is used for the lasier cavity.

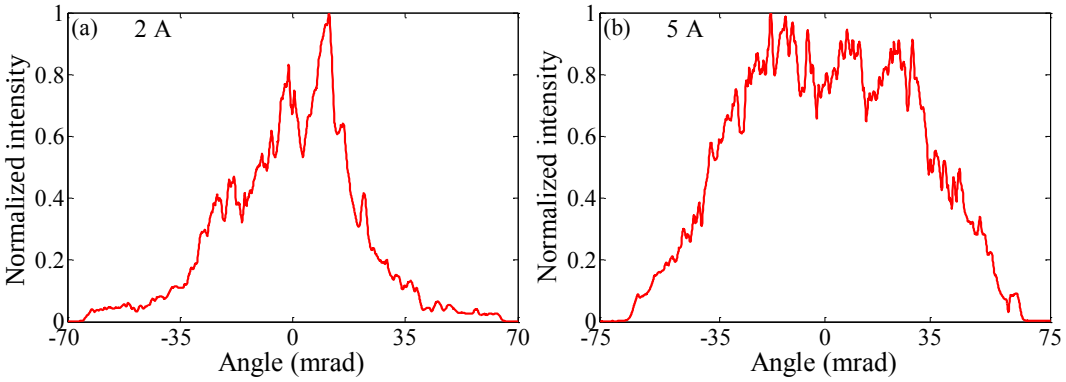

Fig. 4.13: far-field beam profiles as a function of the injection current for (a) 2 A injection current and (b) for 5 A injection current.

At lower pump current, the profile is narrower with deeper vallies. At higher pump current, the profile has broader width with no deeper vallies. The same will be applicable for increasing the reflectivity of feedback mirror which will be shown in chapter 5. The dependence of far field divergence on pump current is shown in figure 4.14 (a). With increase in injection current, higher order spatial modes are excite which increases the spatial width of the beam.

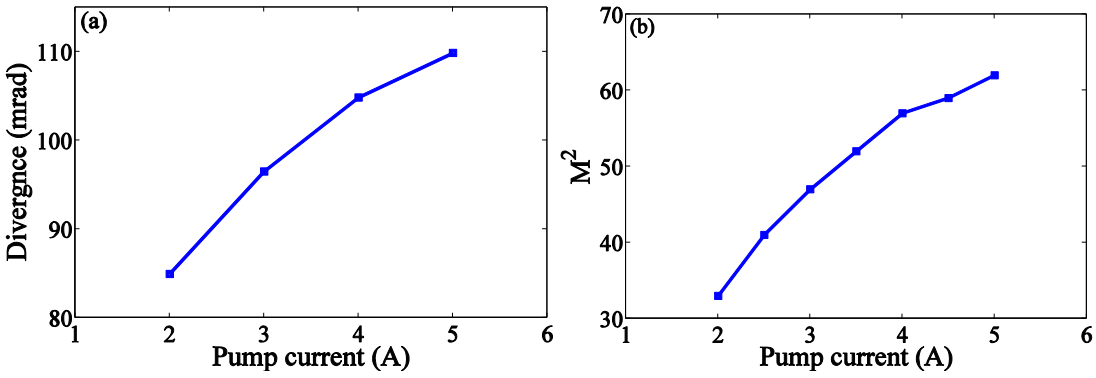

Fig. 4.14: Shows the (a) dependence of divergence of far field on pump current and (b) unfiltered laser M^2 value with the injection current.

The measurement of the M^2 factor as a function of the input injection currents shows a monotonic increase, indication of beam quality degradation with injection current. The M_x^2 values, increasing from 30 at 1.8 A ($1.38I_{th}$) to 62 at 5 A ($3.8I_{th}$), are consequence of the non-Gaussian emission by these high-power lasers (figure 4.14 (b)).

4.4. Spatial filtering in extended cavity configuration

The first proof of spatial filtering in the broad area laser using extended cavity configuration will be discussed in this section. The results were obtained using both the intracavity slit and PhC (sample 1). These measurements were performed at at single pump current of 3 A and feedback mirror reflectivity of 4%. The results obtained by exploring the pump current and mirror reflectivity will be discussed in the next chapter.

4.4.1. Spatial filtering using intracavity slit

Before exploring the PhCs, we first test the effect of the spatial filtering using an intracavity slit placed in the far field plane (plane C in figure 4.15). The slit is an easily available option and most commonly used as spatial filter. The schematic of the setup is as shown in figure 4.15, where a well-calibrated variable slit with step size of 0.5 mm is used for the experiment. Spatial filtering can be implemented also in a single-pass configuration outside the cavity. However, this linear single-pass action, while improving the spatial quality of the beam (reducing M^2 along the slow axis) does not increase the brightness of the emitted radiation.

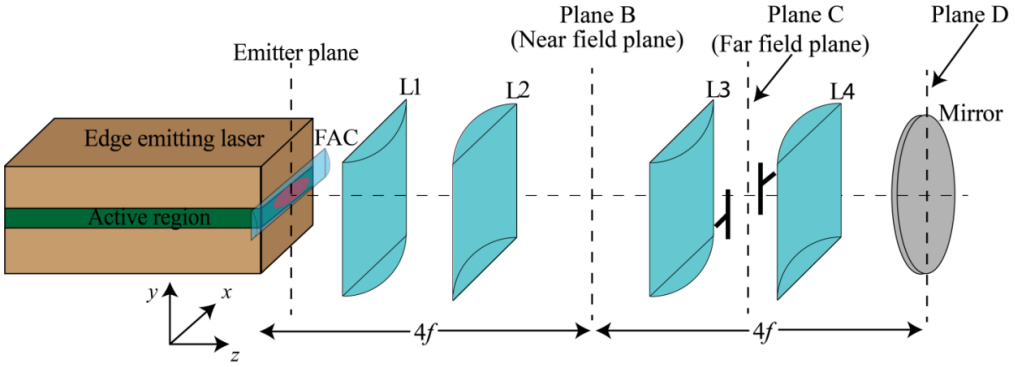

Fig. 4.15: Spatial filtering using intracavity variable slit placed in the far field plane (plane C).

The slit acts in the slow axis by laterally blocking the beam placed at the Fourier plane. The slit serves as a spatial filter that introduces losses to higher order transverse modes. The use of intracavity filtering in a conventional confocal lens arrangement, as the one we propose, suppresses the higher-order transverse modes concentrating most of the

pumping energy into the lowest order modes. The increase in brightness is obtained because closing the aperture has a weak effect on the total intensity, which decreases weakly, but a strong effect on the beam divergence, which can decrease considerably. If the aperture is too narrow, it will start to affect the lowest transverse modes and the brightness will decrease.

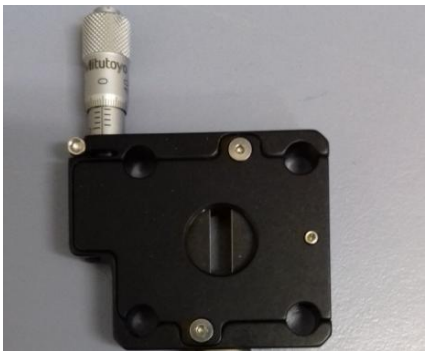

Fig. 4.16: Shows the variable width slit used as a spatial filter.

The slit has variable width from 6.5 mm to 1 mm. As we start to close the slit, the higher order modes start to be suppressed and for a slit width of 1 mm, only the lower order mode continues to lase. Figure 4.16 shows the photograph of the variable slit used in the experiment. The effect of slit along the lateral axis is illustrated in fig. 4.17. The beam width along the lateral direction with decreasing the slit is clearly seen in the figure.

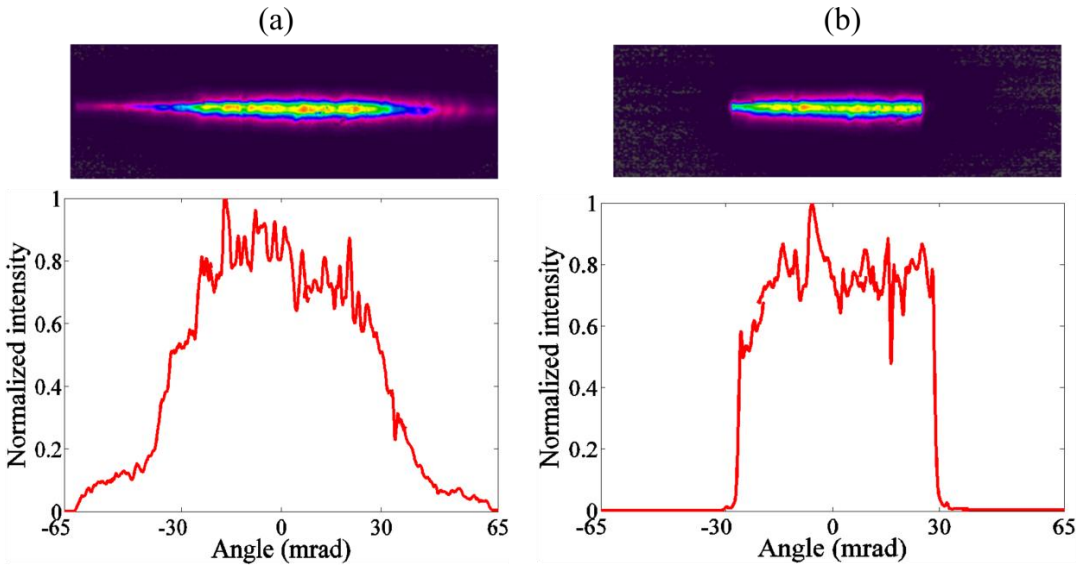

Fig. 4.17: Shows the effect of slit on the far field profile (a) far field profile with no slit (b) when slit is introduced inside the cavity having width.

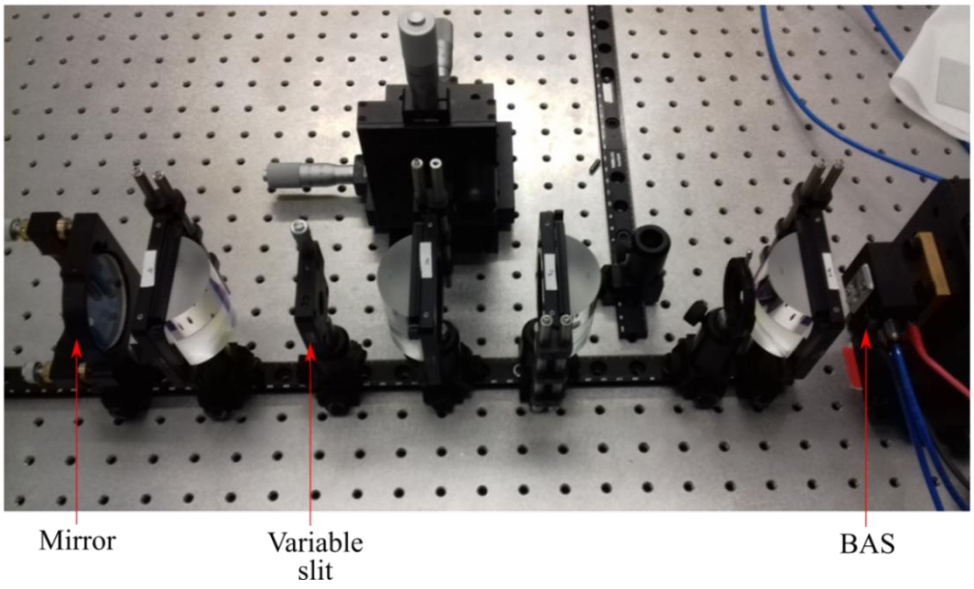

Fig. 4.18: Photograph of the experimental setup showing variable slit in plane C.

The experimental setup of intracavity spatial filtering using slit is shown in fig. 4.18. The variable slit is placed in the plane C of fig. 4.15.

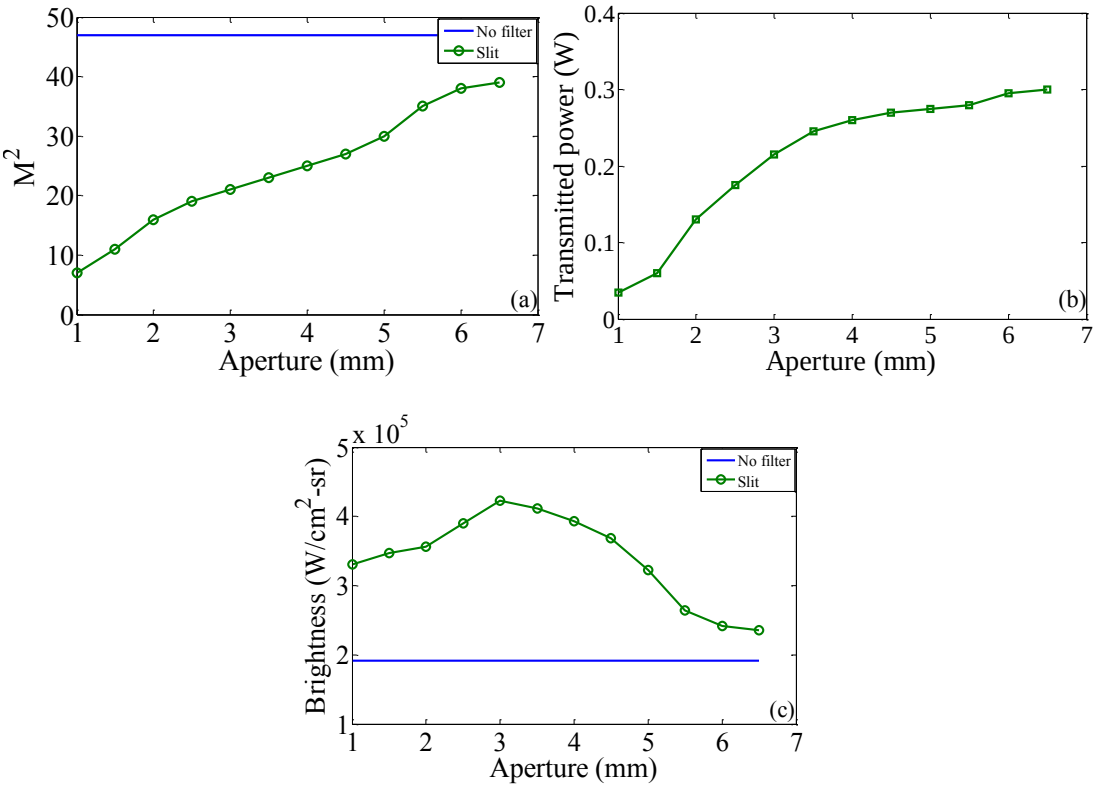

Fig. 4.19: Results of spatial filtering using intracavity slit (a) M_x^2 as a function slit aperture, (b) output power as a function of aperture and (c) brightness for varying slit values.

The injection current used in the experiment was 3A. At this current the emitted beam has an M_x^2 factor of 47, as shown in figure 4.14 (a). The values of this unfiltered case are shown in blue horizontal lines in figure 4.19.We measured the M^2 factor at several slit widths and, as can be seen from the figure 4.19 (a), the M_x^2 decreases with decreasing the aperture of slit. The corresponding reduction in output power as we close the slit is shown in figure 4.19 (b). Figure 4.19 (c) shows the brightness of the beam at the different filtering positions.

When compared with the unfiltered case, we observe an enhencement of brightness as expected. The brightness is maximum at aperture of 3 mm and at lower values it falls due to loss in the optical power. The maximum enhancement at the most optimum slit width is around 2.2. This result confirm the possibility to obtain an improvement of the optical quality of the emitted beams by the action of the spatial filtering in an intracavity configuration.

4.4.2. Photonic crystal spatial filtering in BAS laser

In the previous section, we demonstrated the possibility to achieve an increase of brightness by the action of the filtering in the confocal configuration using a variable slit. This is not our principal objective since it is not possible to integrate this configuration into a monolithic, compact implementation in a real device. This step helped us to obtain the expected brightness enhancement and to establish a comparison with the performance of the PhC filtering. As commented in previous sections, the filtering action of the PhC takes place when it is placed in the near-field plane, whereas the conventional spatial filtering with the slit acted on the far-field plane. In our extended cavity configuration, the near field corresponds to the plane B, in figure 4.20, conjugated of the exit semiconductor facet plane.

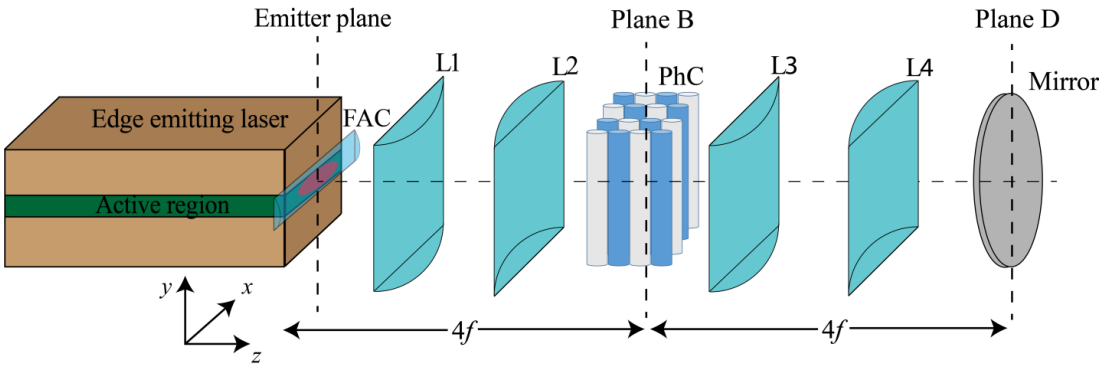

Fig. 4.20: Spatial filtering in extended cavity configuration using photonic crystal (PhC) as spatial filter.

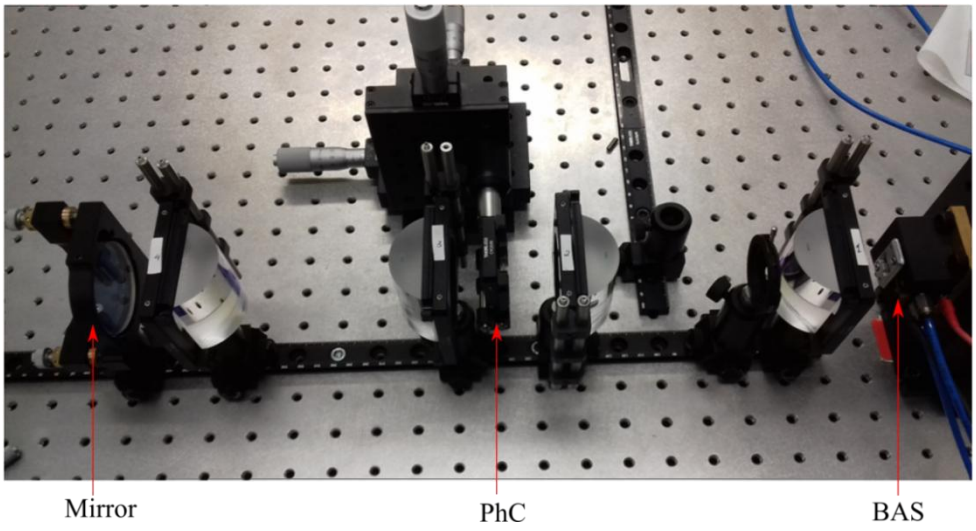

Fig. 4.21: The photograph of experimental setup. The PhC is place at plane B, which is the near field plane.

The extended cavity setup remains same as shown in figure. 4.15 except that spatial filter (PhC) is placed in plane B. The working mechanism of PhC as spatial filter is that it filters out higher angular components, which reduces the divergence angle of the central mode. When PhC placed in inside the cavity, the laser beam makes many pass through the PhC and in each pass it removes the higher order modes and fills the lower order modes. The PhC in single pass transmission could improve the beam quality, but the brightness does not increase. In the next sub-section, we will discuss the filtering performance of PhC in intracavity configuration. The deflected beam after the PhC is shown in figure 4.22.

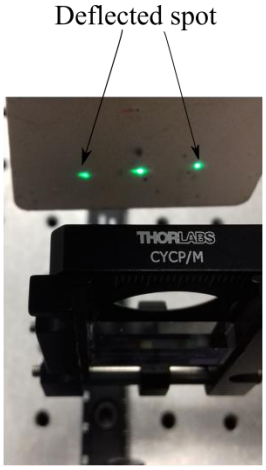

Fig. 4.22: The deflected light after the PhC.

Gaussian-beam fabricated Photonic crystal

The first test of spatial filtering using PhC is conducted using Gaussian beam fabricated crystal. The fabrication process of this crystal remains same except that the incident beam used to inscribe the PhC is high spatial quality Gaussian beam from femtosecond laser. The fabricated structure is non-chirped. The PhC has transverse period ($d_\perp$) of 2 µm with $Q = 0.9$ at 970 nm and number of longitudinal period (N_p) equal to 10. The size of structure is 2x2 mm^2, enough to fit whole beam inside the PhC.

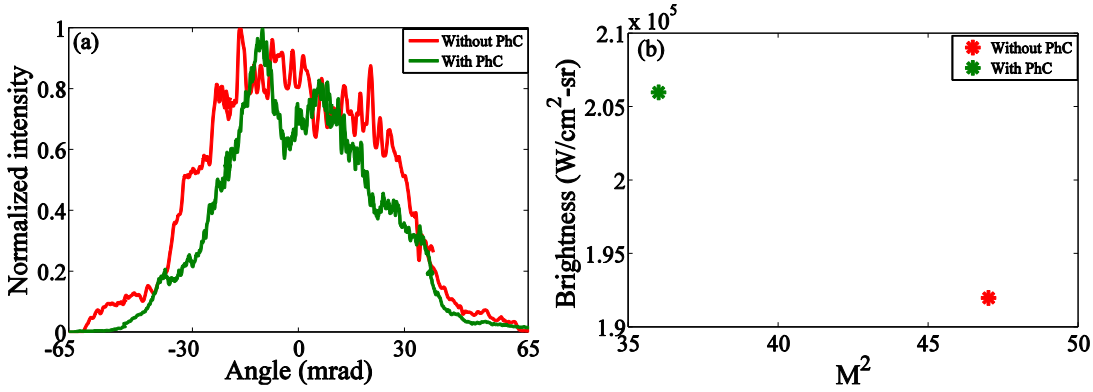

Fig. 4.23: (a) Far field profile with and without PhC and (b) their corresponding M^2 and brightness.

The far field profiles with and without the PhC as plotted in figure 4.23 (a) show a substantial narrowing of the far-field profile by the action of the filter. Although the M_x^2 factor decreased from 47 to 36, the output power drop from 0.31 W to 0.23 W at 3A injection current, led to a negligible increase in the brightness of the beam. The reduction in M_x^2 was not sufficient to compensate the output power loss and hence the brightness did not increase with the use of this filtering crystal. In order to improve the performance of the filter further crystals were fabricated using a Bessel beam technique in order to improve the quality of the filters.

Bessel beam Photonic crystal 1

For the experimental purpose, we used two PhC with different geometry factor and chirp. The first PhC (sample 1) described in this section was used for the demonstration of spatial filtering and compare the filtering performance with intracavity slit.

The PhC is a chirped structure with a Q value ranging from $1.15 \leq Q \leq 1.27$ and transverse period $d_x = 3\,\mu m$. The size of the fabricated structure 2.85 × 2.3 mm^2 is large enough to safely accommodate the whole focused beam into the filter aperture. The beam is incident on the crystal, showed in fig. 4.24, along the z-direction.

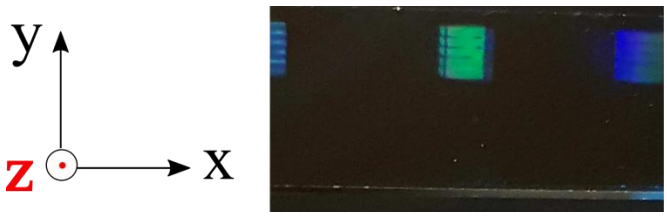

Fig. 4.24: Fabricated structure used in the experiment.

The spatial filtering performance was tested by placing the PhC inside the cavity. The PhC was mounted on 3-axis stage, placed at focal plane (plane B), and carefully arranged inside the beam path. The beam diameter along the slow axis is of 450 µm, enough to fit the entire beam inside the PhC. The far field distribution without and with the PhC were recorded using a CCD camera. Figure 4.25 (a) shows the reduction in the far field profile induced by the filtering action of this crystal. The reduction in the far field profile by a factor of 1.8 times compared to Gaussian-beam fabricated crystal which is 1.5 times as seen in figure 4.23, indicating the improvement of the quality of the crystals using the new Bessel-beam technique.

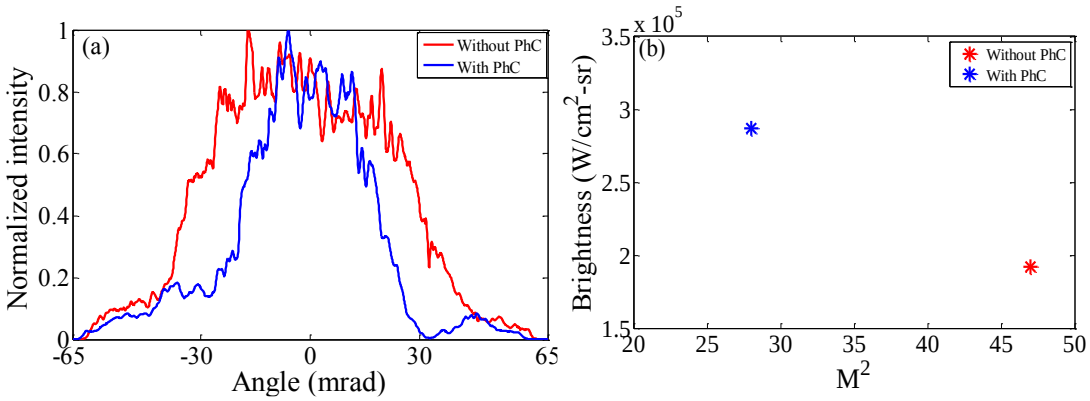

Fig. 4.25: (a) Far field profile with and without PhC and (b) brightness values.

Measurements were performed at a pump current of 3 A and with a reflectivity of the feedback mirror of 4%. The measured M_x^2 factor, with a value of 47 when there is no PhC inside the cavity, drops down to a value of 28 by the action of this filter. The reduction of the power measured in this case results in a brightness enhancement for this crystal. The corresponding M^2 and brightness values obtained are shown in figure 4.25 (b). From these results, we demonstrate brightness-enhancement by a factor of 1.5. Even if this result is lower than the one obtained using the slit, it indicates a clear indication of the possibility of improving the beam quality by the use of near-field filtering by means of PhC filters.

4.5. Near field profile with intracavity slit/PhC

As has been discussed previously, the filtering effect introduced by the slit or the PhC acts on the higher-order transverse modes of the laser and is observed mainly in the far field profile of the laser. The changes in the far field should be also related to changes in the near field. To see the effect of these filters on the near field, we imaged the near field plane outside the cavity when either the PhC or the slit were introduced in the near field plane or in the far field plane respectively inside the extended cavity. The near field profile recorded for different values of the slit are shown in Figure 4.26.

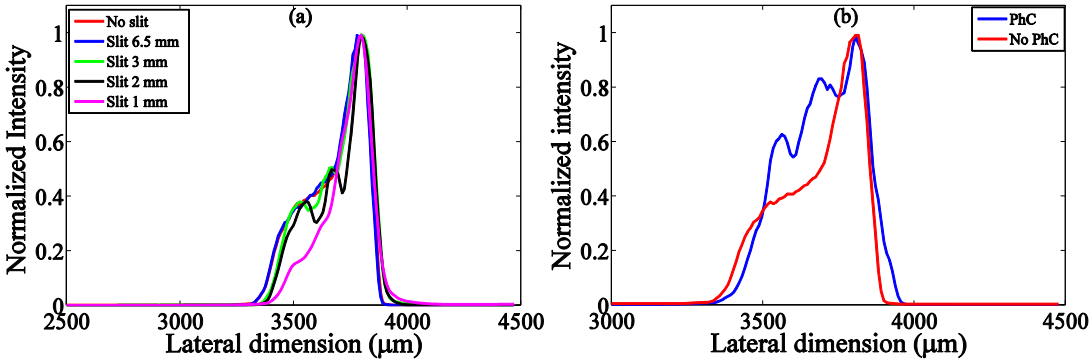

Fig. 4.26: Effect of slit/PhC on the near field profile (a) with intracavity slit (b) with PhC.

Initially, when the slit was wide open, the profile remains unaltered. The asymmetric shape of the emitted radiation in the near field is related to our particular laser and is not related to any filtering effect in the extended cavity. The effect of the slit is observed in figure 4.26 (a) and the effect of PhC was recorded as seen in figure 4.26 (b). In the case of intracavity slit, the filter acts on the beam laterally and the change is negligible when slit is wide open. As the slit is closed, the modification of the near field profile is clearly observed, with some oscillations appearing at aperture values between 2 and 3 mm, reflecting the changes in the energy distribution between the lasing modes in the far-field. As the slit is further increased, to values of 1 mm the drastic reduction of the far-field modes results in a well-observable smoothing of the emitted near-field profile reflecting the filtering effect of the slit. For the case of PhC filter case, the whole beam is focused inside the structure, which modifies the central part of the beam. Oscillations are observed in the near field profile consistent with those obtained for the slit at intermediate apertures.

Chapter 5

Intracavity Spatial Filtering

After demonstrating the possibility to achieve brightness enhancement in broad area edge emitting lasers by spatial filtering in an extended cavity configuration using intracavity slit and PhC for a single reflectivity of the feedback mirror and at a fixed pump current, we present in this chapter a detailed experimental and numerical study of the PhC spatial filtering performance and discuss about the effect of increasing the reflectivity of feedback on the output power and far field profile.

We first explore, in section 5.2, the spatial filtering using intracavity slit in the far field plane discussing the results obtained with different pump currents and changing the reflectivity of feedback mirror. The beam quality factor and brightness will be determined with and without the slit placed inside the cavity and the experimental results obtained by intracavity slit will be compared with numerical results obtained from the numerical model outlined in chapter 3.

In section 5.3, the results of spatial filtering using PhC in the same extended cavity configuration will be discussed under identical conditions. The action of PhC is numerically simulated for a single reflectivity of the feedback mirror. In the last part of this chapter, we numerically optimize the filtering function of the PhC.

5.1. Effect of reflectivity of feedback mirror

Since the fraction of laser output that returns back depends on the reflectivity of the feedback mirror, in this section we investigate the effect of changing the reflectivity of the feedback mirror on the output power and far field profile. By increasing the reflectivity, the photon density inside the cavity increases and the number of transverse modes increases leading to a change in the far field profile. We used three different reflective mirrors (4%, 6%, and 8%). The result of the spatial filtering using a 4% reflectivity mirror was discussed in the last chapter. We limited the reflectivity to 8% to avoid the possibility of causing catastrophic optical mirror damage (COMD) to the laser facet [122].

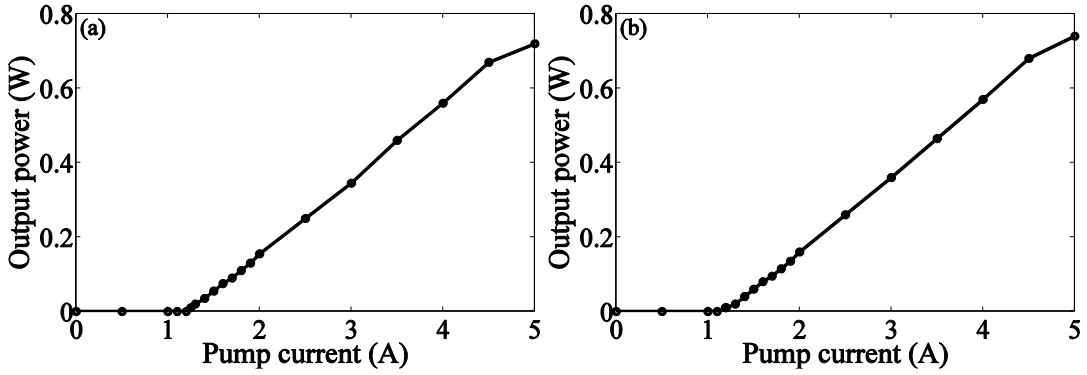

Fig. 5.1: The effect of changing the reflectivity of feedback mirror on output power. (a) for 6 % reflective mirror (b) for 8 % reflective mirror.

The threshold current for the case of a 4% reflectivity mirror is 1.3 A, whereas with 8% reflectivity it drops to 1.2 A. The output optical power depends on the mirror reflectivity, being 0.31 W, 0.34 W, and 0.36 W at 3 A (2.3 I_{th}) for reflectivities of 4%, 6%, and 8% respectively. The maximum current applied to laser is 5 A. The L-I curve for 4% mirror in pulsed mode is shown in fig. 4.10 (a). By changing the reflectivity, we observe a negligible change in the output spectrum. The L-I curve for 6% and 8% reflectivity is shown in fig. 5.1 (a, b). The far field profile for both reflectivity is shown in figure 5.2.

The far-field profiles are broadened by the increase of injection pump current and with the mirror's reflectivity. The width (FWHM) of the far-field profiles estimated from the figure gives a value of 44 mrad (Fig. 5.2 (a)), 71 mrad (Fig. 5.2 (b)), 55 mrad (Fig. 5.2 (c)) and 84 mrad (Fig. 5.2 (d)). From these values we see that the increase of injection current from 2 to 5 A increases the bandwidth by a factor of roughly 1.55 in both cases, while an enhancement of roughly 1.25 is observed by the increase in the reflectivity of the feedback mirrors.

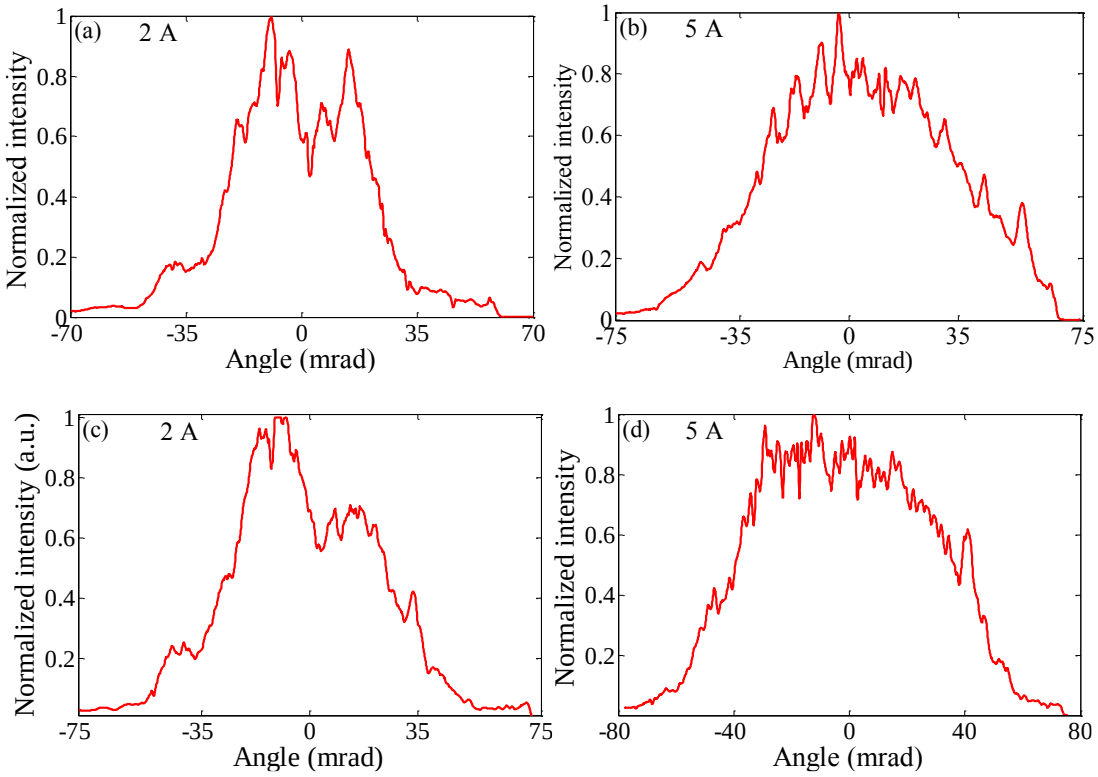

Fig. 5.2: The far field profile with increasing pump current from 2 A to 5 A for two different reflectivity of feedback mirror. The figure (a, b) for 6 % reflective mirror and (c, d) for 8 % reflective mirror.

.

5.2. Spatial filtering using slit

5.2.1. Experimental result using slit

The effect of the injection current on the emitted brightness by the action of the intracavity slit, placed in the plane C as shown in figure 4.15, was tested by repeating the measurements performed with the 4% reflectivity mirrors at different injection currents above the lasing threshold. By reducing the slit width in steps of 0.5 mm, the output optical power, and corresponding M^2 factor was measured for each case. The transmitted power for each slit width is plotted in figure 5.3 (a) and the corresponding M_x^2 factor is shown in figure 5.3 (b). As the slit width decreases, the M_x^2 also decreases. Based on the M_x^2 factor and transmitted power, we calculate the brightness of the beam. The absolute and relative (with respect to the unfiltered beam) brightness map as a function of the aperture width and pump current is shown in figure 5.3 (c, d). The relative brightness map indicates a maximum enhancement in the brightness observed close to the region of 3A injection current and 3 mrad of slit aperture. From this plot, a maximum relative enhancement factor of 2 is observed.

A close inspection of the dependencies of the M^2 factor and emitted power as a function of the slit width suggest some basic trends. The reduction of M^2 factor with slit width tends to be linear as the injection current is increased while it tends to decrease more strongly as we close the slit for injection currents close to the laser threshold.

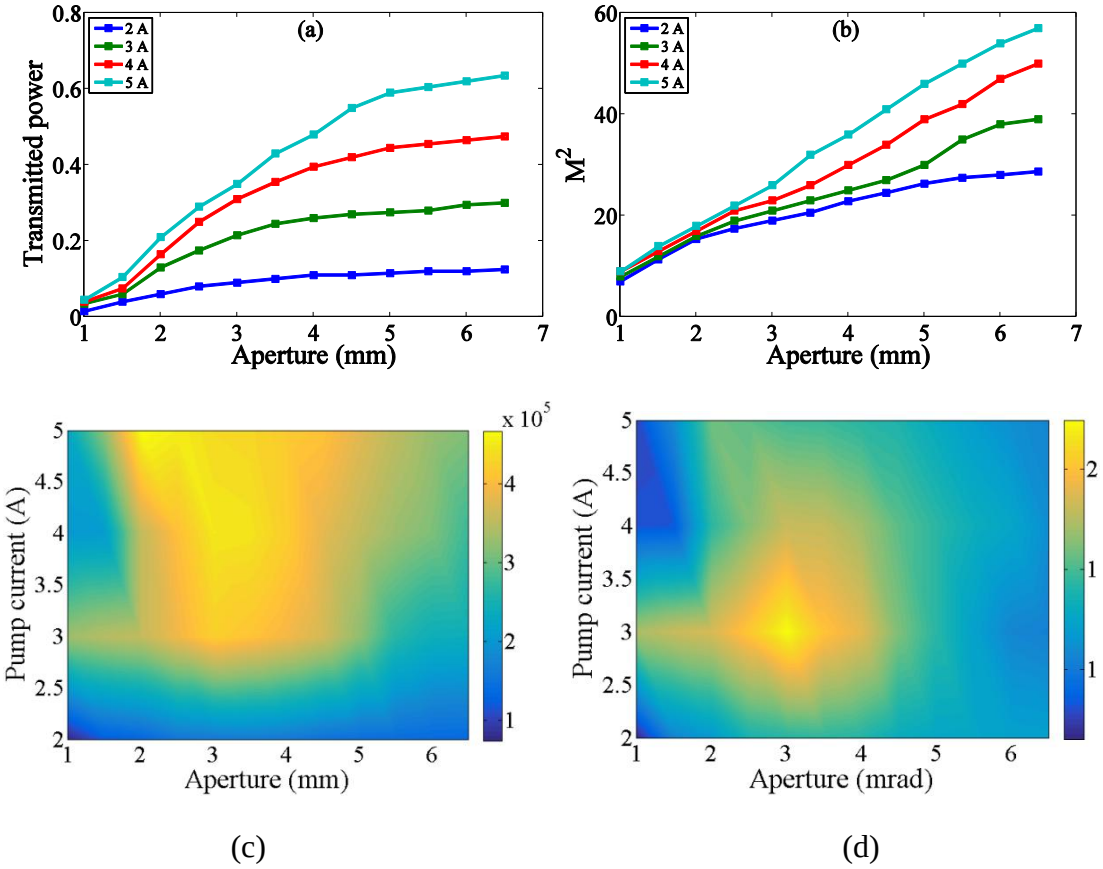

Fig. 5.3: For 4% reflective mirror, the plots: (a) transmitted power, (b) M^2 as a function of slit width. The absolute brightness map (c) and relative brightness map (d).

The same procedure was repeated changing the reflectivity of the feedback mirror from 4 % to 6 %, the rest of the experimental setup remaining the same. The output powers, as expected, increase slightly by 20 mW with increasing the reflectivity of the feedback mirror. The M_x^2 also increase following increase in number of photons inside the cavity. The M_x^2 and the transmitted power measured under these conditions are shown in fig. 5.4 (a, b). From these measurements, the calculated values of the brightness show identical trends to those outlined in the previous case: a continuous increase of the absolute brightness with the pump current and the appearance of an optimum region for relative brightness enhancement close to the region found previously. The maximum enhancement achieved is 2.2.

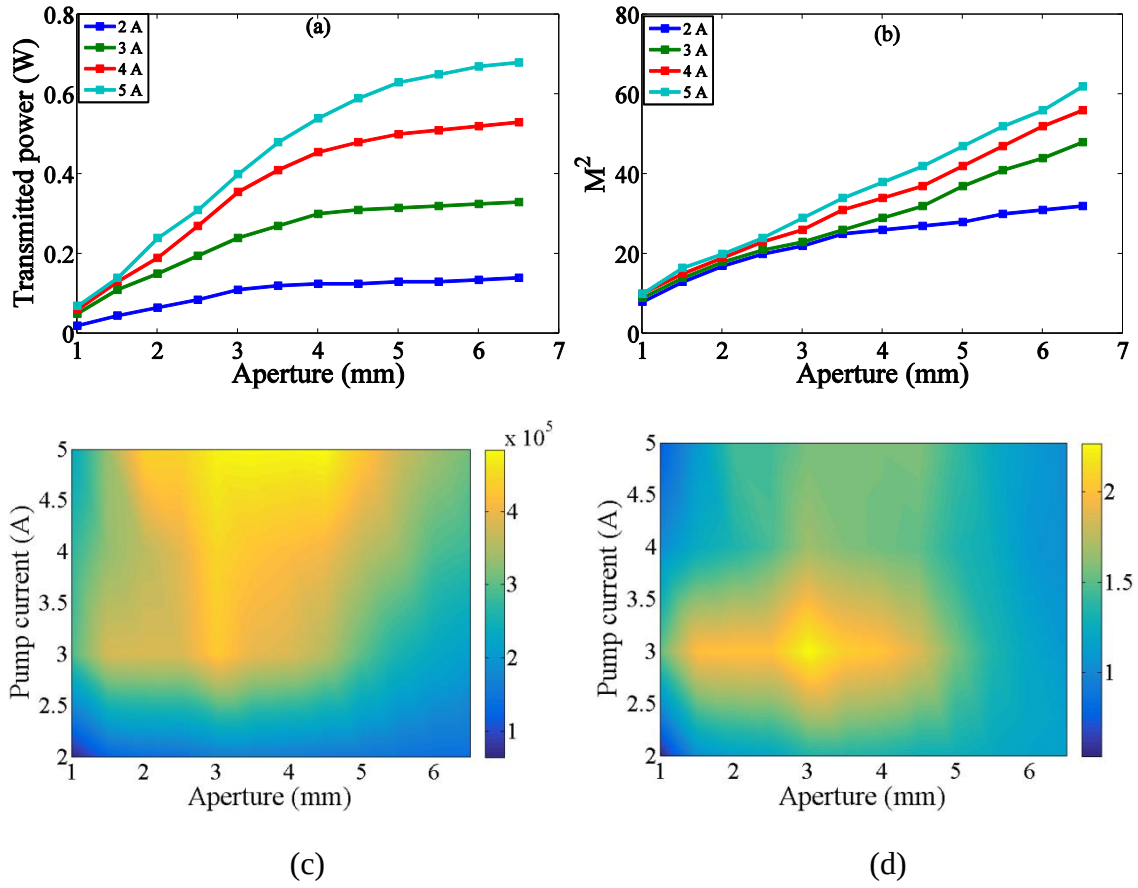

Fig. 5.4: For 6% reflective mirror, the plots: (a) transmitted power, (b) M^2 as a function of slit width. The absolute brightness map (c) and relative brightness map (d).

Here we change the reflectivity to 8%. Similar trend was observed with increase in reflectivity to 8 %. At this point, we stop further increasing the reflectivity of feedback mirror due to possibility of COMD. The transmitted power increases with pump current and decreases by closing the slit width. The M_x^2 increases further with increase in output power. The plot of M_x^2 and transmitted power is shown in fig. 5.5 (a, b). At maximum pump current, the output power is increased by roughly around 20 mW whereas M_x^2 increases from 62 to 65. The calculated absolute and relative brightness is shown in fig. 5.5 (c, d). The maximum enhancement in the brightness (relative brightness) is by factor of 2 times and located at around 3 A pump current and slit width of 3 mm.

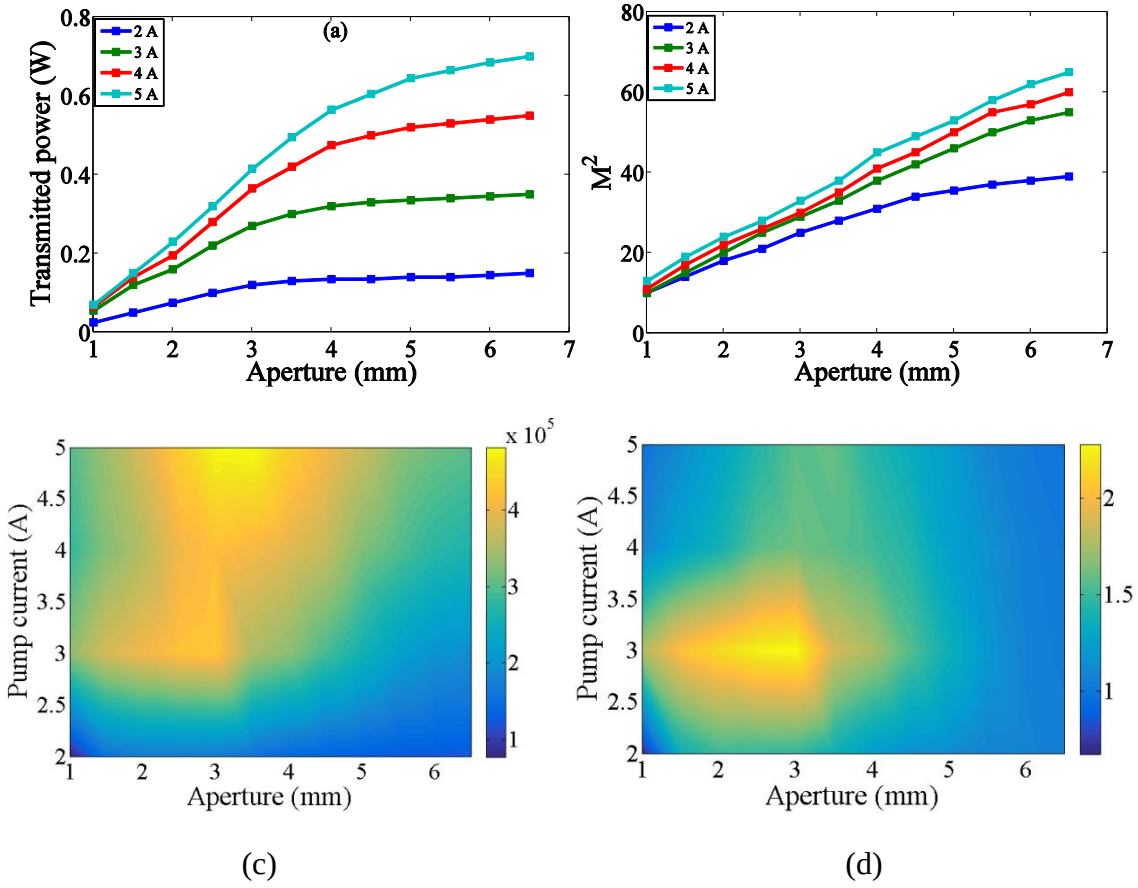

Fig. 5.5: For 8% reflective mirror, the plots: (a) transmitted power, (b) M^2 as a function of slit width. The absolute brightness map (c) and relative brightness map (d).

The detailed characterization of the laser behavior under changing conditions has shown that there exists a set of parameters for optimum brightness enhancement under conditions of slit filtering inside the cavity. The decrease of the slit width gives rise to a reduction of the M^2 factor accompanied by a reduction of the emitted power. Since these two effects act in opposite directions to give the final brightness emitted by the laser, it is not surprising that the most optimum region appears somewhere in between the extreme situations. A too closed slit gives rise to a too large power decrease, which cannot be compensated by the reduction in the beam divergence caused by the disappearance of the high diverging modes form the laser far-field profile. On the other side, a slit too open is affecting very slightly the far-field and hence modifying the output properties of the emitted beam. From this study, we can conclude that the region of maximum relative brightness enhancement is not changed by the increase in the reflectivity of the laser cavity mirror.

5.2.2. Numerical simulation of spatial filtering using slit

The action of spatial filtering using intracavity slit is numerically evaluated for single case of 4 % reflective feedback mirror. The numerical model of laser is already discussed in section 3.3 of chapter 3. The slit is introduced as transverse wave number cut-off filter in the Fourier space. The cut-off wave number that simulate the slit goes from 0.25 μm^{-1} to 0.5 μm^{-1}, which corresponds to aperture values from 70 to 10 mrad.

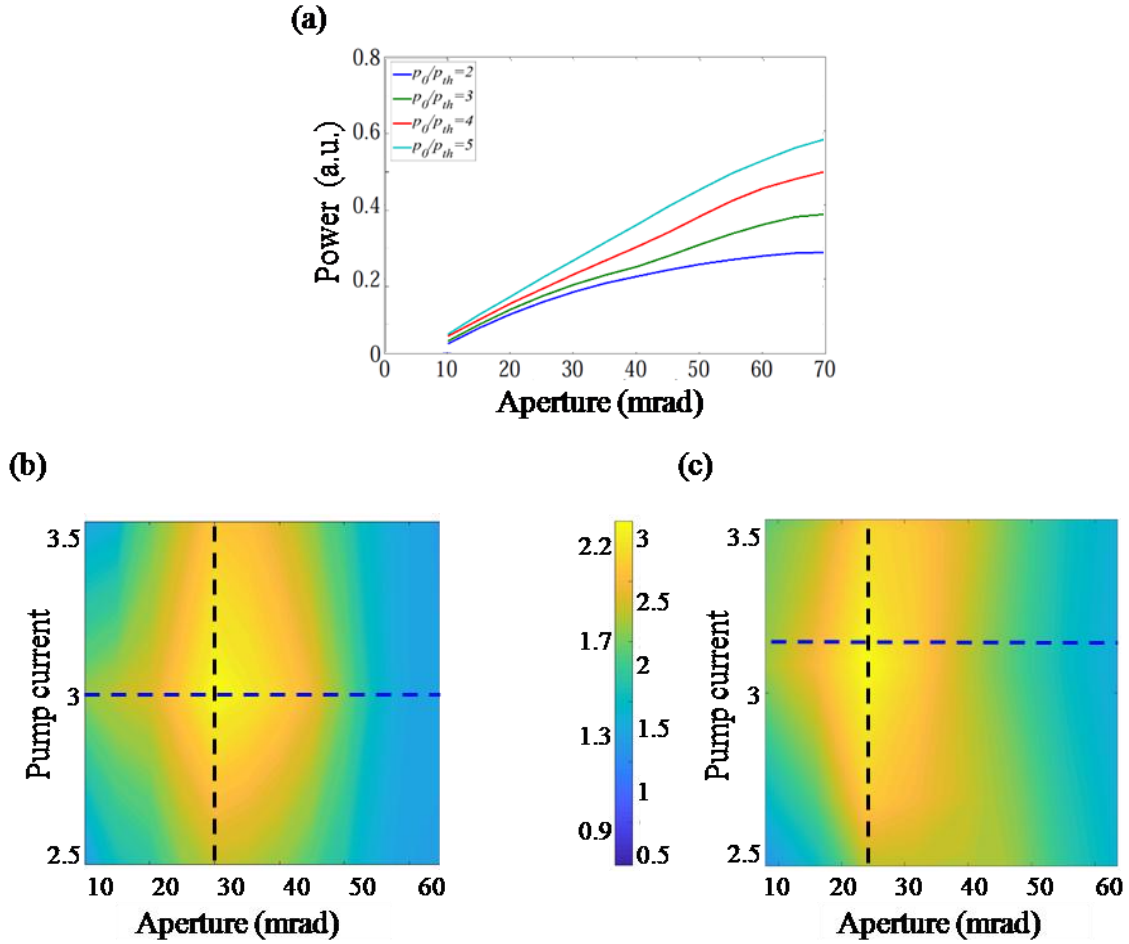

Fig. 5.6: (a) Numerical results for transmitted power versus aperture. The relative brightness for (b) experimental and (c) numerical results.

Figure 5.6 (a) shows the dependence of the transmitted output power as a function of the width of the variable slit from different pumping currents expressed normalized to the threshold current. The maximum power is recorded with no slit inside the extended cavity, decreasing as the width of the slit is reduced. Similar trend is observed in the experimental results shown in figure 5.3 (a). By increasing the pump current, the changes in the beam are better distinguished in the far-field, while the near field always presents some modulated profile. The simulated output profiles are obtained by

averaging thousands of integration round-trips. Even though experimental and simulated far-fields show some discrepancies, these could be attributed to the model simplification [123]. The M^2-factor can be numerically evaluated from the width of the near-field and far-field simulated profiles. As we increase the pump current, the output optical power increases along with the M^2-factor due to the excitation of more spatial modes. The effect of the slit was evaluated by calculating the increase in brightness of the output beam.

Results show that the absolute brightness continues to increase when pump current is increased, however, the relative brightness decreases after an optimum value is achieved. The comparison of experimental and numerical relative brightness map is shown in figure 5.6 (b, c) for the 4% reflective mirror. The experimental and numerical results show good agreement with the same tendency. The maximum relative brightness is of the order of 2.2 in both cases and occurs at similar apertures, around 25 mrad and for a pump current close to 3. Similar results were observed by changing the reflectivity of the laser cavity mirrors from 4% to 8%. These results confirm the validity of the model to be used for the simulations with the photonic crystals filtering.

5.3. Photonic crystal spatial filtering

5.3.1. Experimental result

In this section, we used another PhC (sample 2) with different geometry factor and chirp inscribed using Bessel beam. The PhC is also chirped structure with Q value ranging from $1.10 \leq Q \leq 1.60$ and transverse period $d_x = 3\ \mu m$ and number of period equal to 60. The photograph of the fabricated sample and the microscope image is shown in fig. 5.7.

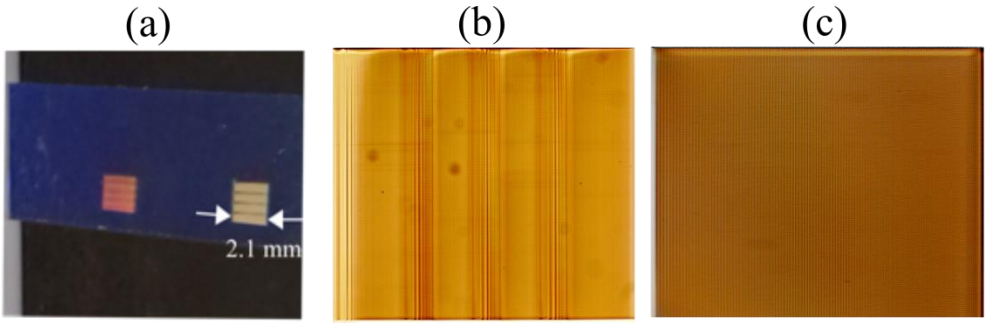

Fig. 5.7: (a) Photograph of fabricated chirped structure (b) microscope image of the structure (c) magnified view.

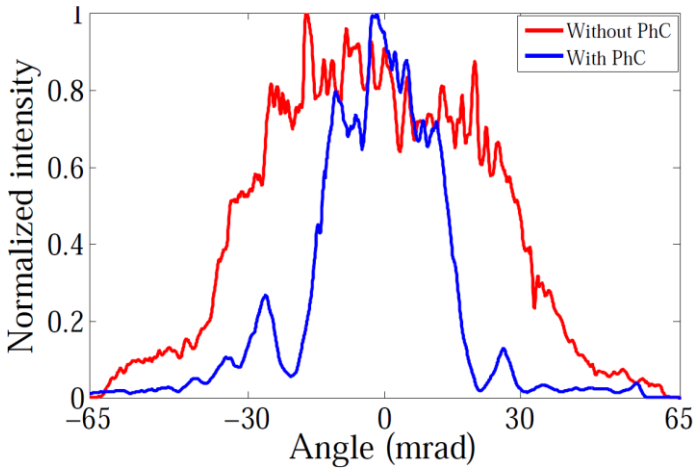

Fig. 5.8: The effect of PhC spatial filtering on the far field profile of the laser.

The filtering performance of this PhC was tested as usual by introducing the PhC inside the resonator according to the setup shown in Fig. 4.21.The filtering effect is explored by varying the laser pump current and reflectivity of the feedback mirror as we did with the slit configuration. The far field profiles with and without PhC are shown in fig. 5.8. where the change in the transmittance function introduced by the filter is clearly evidenced. Fig. 5.9 resumes our observed results of the filtering action of the PhC as a function of the injection current.

The dependence of the transmitted power as a function of the injection current (Fig. 5.9 (a)) manifests the effect of the PhC showing that the linear increase observed in the unfiltered case gives rise to an initial linear increase, which stabilizes at larger currents. Regarding the M^2-factor measurement, resumed in Fig.5.9 (b), it is considerably reduced with the introduction of PhC at all pump currents the induced variation increasing at larger pumps. The corresponding values for the total and relative brightness are presented in Fig. 5.9 (c) and (d) respectively. The linear increase of the absolute brightness of the unfiltered laser beam corresponds to our previous observations. However, the introduction of the PhC filter gives rise to a saturation in the transmitted brightness for larger pumps (see figure 5.9 (c)). The relative brightness, evaluated as the ratio of brightness of unfiltered beam to the brightness of the filtered beam, is shown in figure 5.9 (d). The maximum enhancement is found to be of the order of 1.3, occurring at a pump current of 3 A. The fact that at higher pump currents no further enhancement is seen could be due to thermal effects inside the cavity, which restrict the filtering of higher order modes.

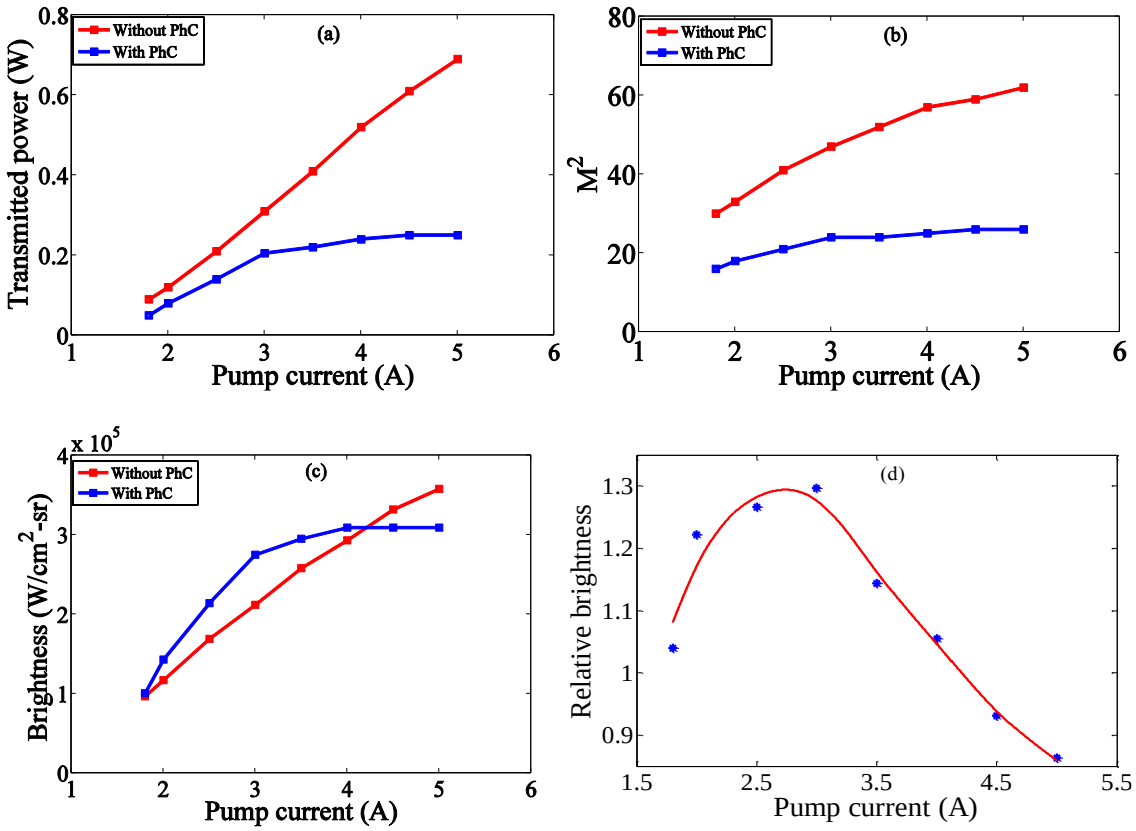

Fig. 5.9: Shows the result of filtering for 4 % reflective of feedback mirror. The effect of pump current on (a) Transmitted power (b) M^2 factor (c) absolute brightness (d) relative brightness.

The measurements were repeated with the same crystal changing the reflectivity of the feedback mirror to 6% and 8%. The resume of our results in both configurations are shown in Fig. 5.10 and 5.11 respectively. From these measurements, we can conclude that the general qualitative trends observed are quite similar irrespective of the value of the reflectivity of the mirror.

For the case of using a 6 % reflectivity mirror, the dependence of the output power as a function of the injection current shows that the linear increase of power of the laser without any PhC is not followed by the filtered emission, which saturates at large injection current values. The M_x^2 factor increases with increase in pump current, but the reduction factor depends on the injection current being more significant at large injection currents. These trends can be observed in Figure 5.10 (a, b). The absolute brightness, calculated based on these measured values, increases linearly with the pump current for the unfiltered laser while reaches a saturation after 4 A pump current with the PhC filtering. The maximum enhancement in the brightness is slightly above 1.3 times.

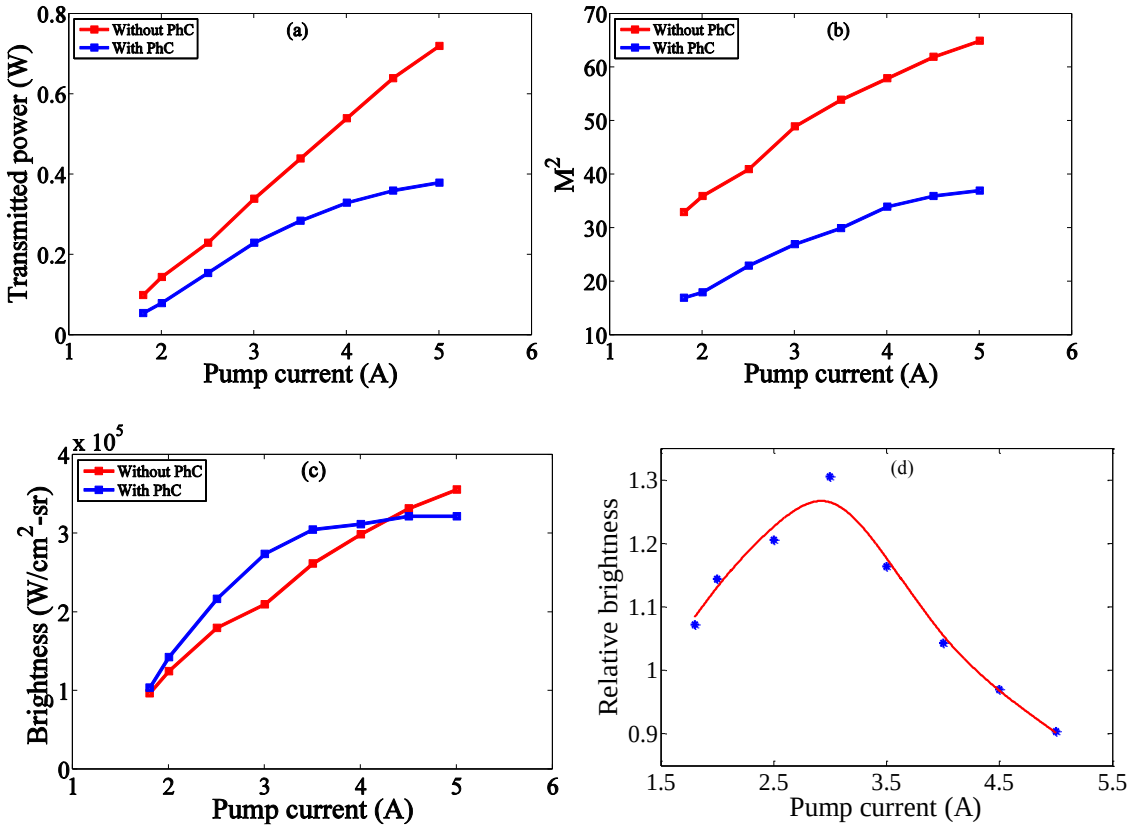

Fig. 5.10: Shows the result of filtering for 6 % reflective of feedback mirror. The effect of pump current on (a) Transmitted power (b) M^2 factor (c) absolute brightness (d) relative brightness.

In the same way, we continue PhC spatial filtering with 8 % reflective feedback mirror. The behavior of the system manifests identical trends as those observed in the previous scenarios. The results for 8% reflective mirror are shown in figure 5.11. In this case the absolute brightness continues to increase without PhC and with PhC it starts to saturate at 3.5 A. The maximum enhancement in brightness is slightly less than 1.3 times.

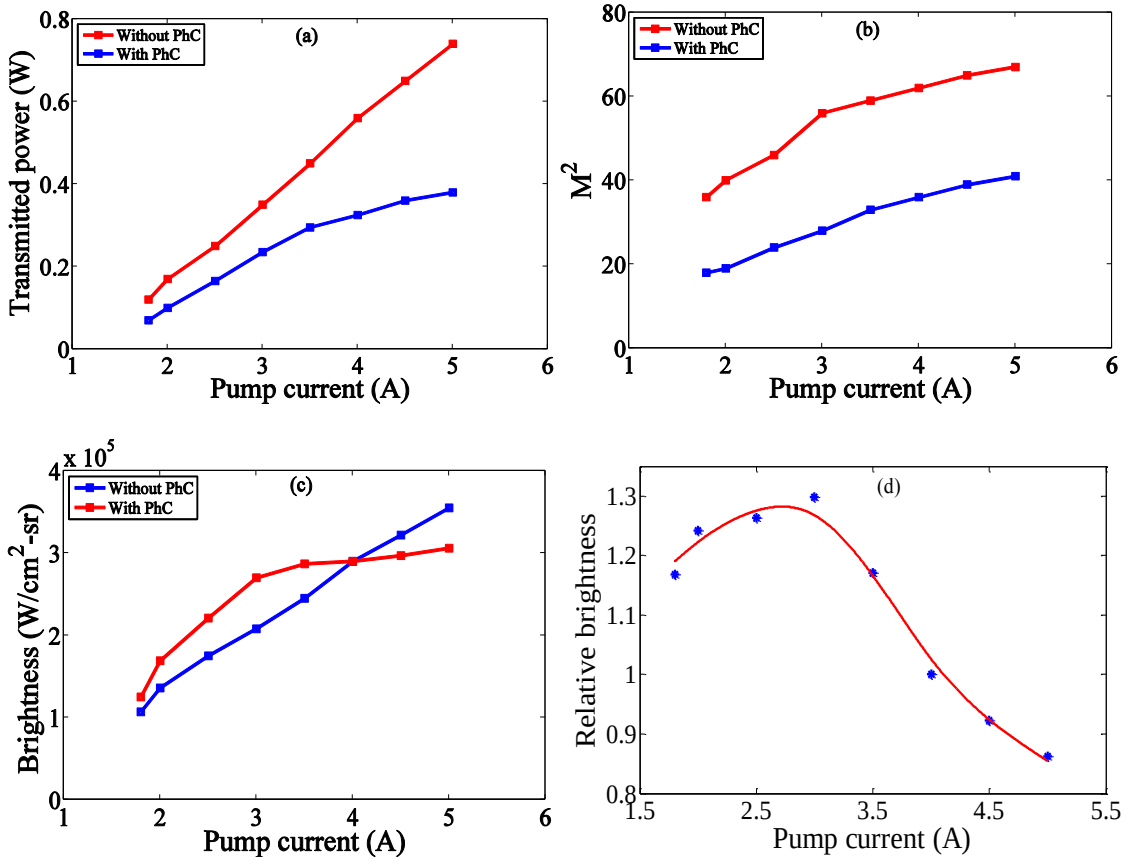

Fig. 5.11: Shows the result of PhC spatial filtering for 8 % reflective of feedback mirror. The effect of pump current on (a) Transmitted power (b) M^2 factor (c) absolute brightness (d) relative brightness.

The effect of the change in feedback reflectivity can be analyzed by plotting all the results in a common plot. The transmitted power with and without PhC is plotted for all three different reflectivity values in figure 5.12 (a). As expected, the 8% mirror has slightly higher transmitted power compared to 4 % and 6 % reflective mirrors. However, the reduction in the emitted power when filtered by the PhC shows a stronger reduction for the 4% reflectivity mirror. The reinjection of energy into the lower frequency modes by the action of the filtering seems to be larger, hence, as the reflectivity of the cavity is increased. Similarly, the M^2 value shows similar behavior and it decreases for all three cases of reflectivity with the introduction of PhC, again showing a stronger decrease for the 4% reflectivity condition. The absolute brightness continues to increase with increase in the reflectivity of the feedback mirror while the behavior in the filtered case is barely dependent on the mirror's reflectivity. The relative brightness shows a maximum around 1.3 at 3 A and a drop after a certain pump current value for all the cases. From these measurements, we can conclude that the general qualitative trends observed are quite similar irrespective of the value of the reflectivity of the mirror.

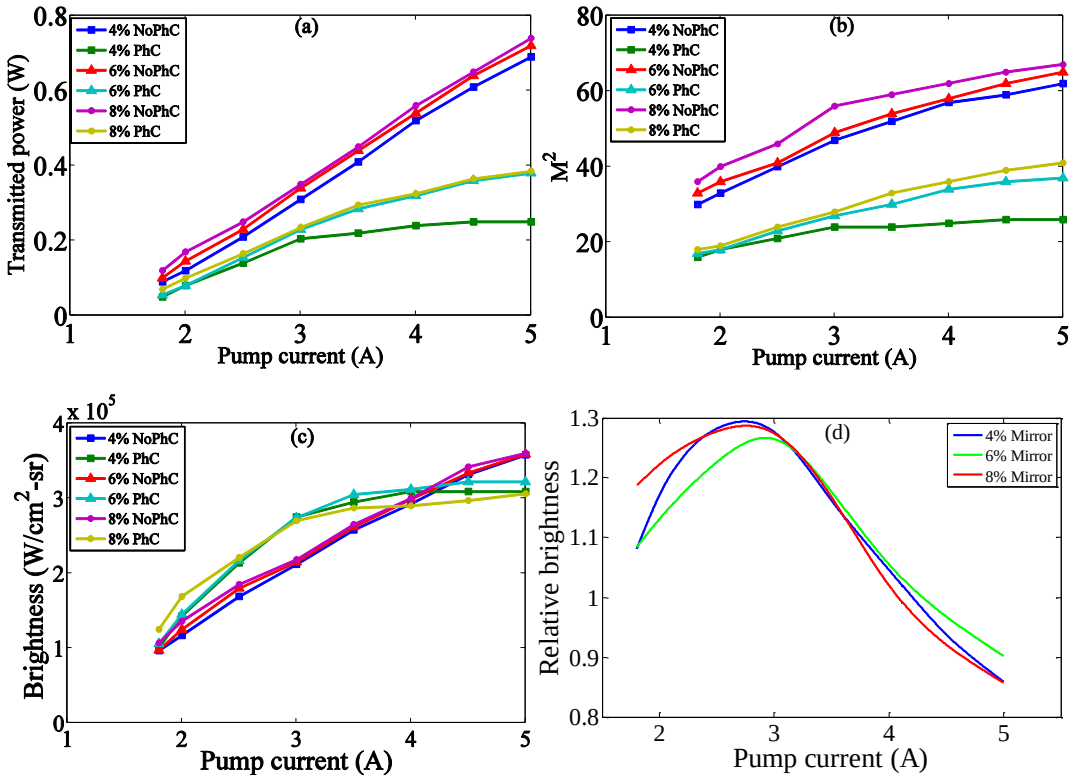

Fig. 5.12: Shows the combined result of PhC spatial filtering for all three reflectivity of feedback mirror (a) Transmitted power (b) M^2 factor (c) absolute brightness (d) relative brightness.

5.3.2. Numerical simulation of spatial filtering using PhC

In this section, the experimentally obtained results were compared with the numerical simulation. The PhC was introduced in the model as a transmission function acting in the near field plane, as discussed in chapter 3 from sample 2.

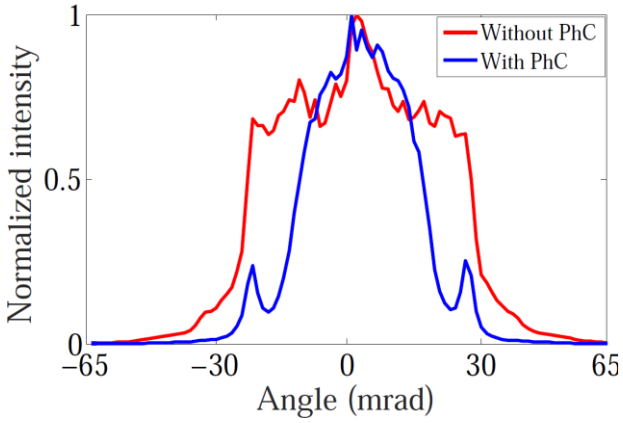

Fig. 5.13: The far field profile with and without PhC. The blue curve shows the effect of PhC.

The numerical simulation of the far field distribution with and without PhC is depicted in figure 5.13. showing a close correspondence between experimental (see figure 5.8) and numerical (see figure 5.13) far field profiles, cut-off angles and divergence angles. For comparison purpose, we will consider only the results of spatial filtering with 4 % reflective feedback mirror, since as we have seen, the general trends are identical in the other configurations. The output power, M_x^2 factor, absolute and relative brightness were analyzed as a function of the injection current in the numerics to establish a comparison with the experiments. To compare the numerical and the experimental results, the latter were normalized to the threshold current.

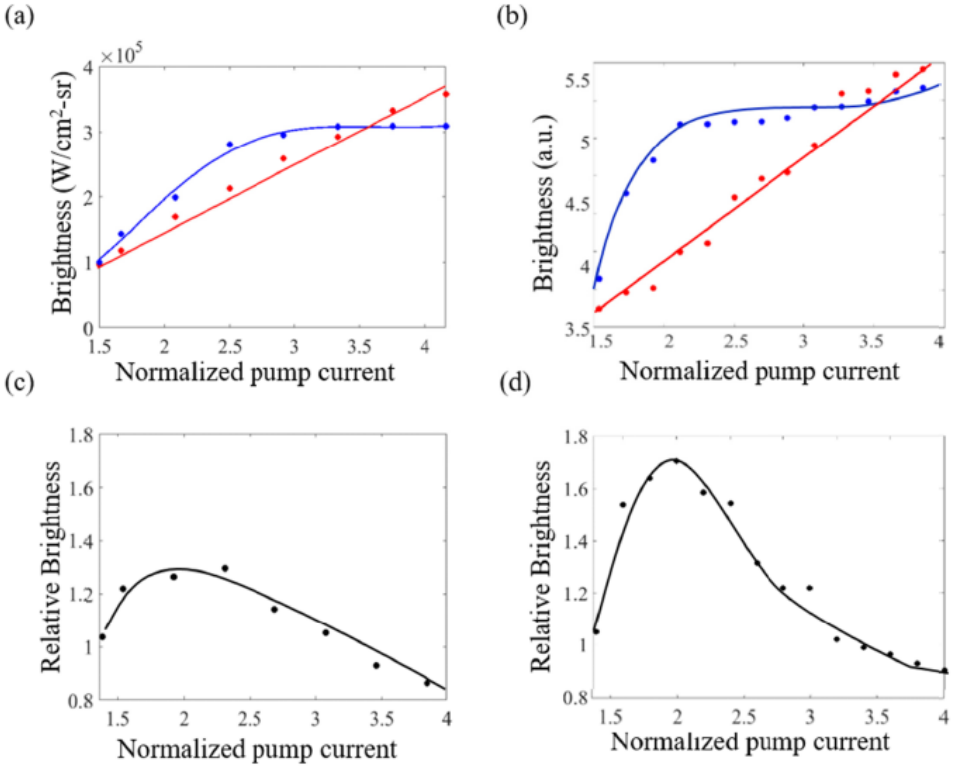

Fig. 5.14: The comparison of experimental and numerical brightness as function of pump current. The red line corresponds to brightness without PhC and blue line corresponds to brightness with PhC. The experimental/numerical (a/b) result for absolute brightness and the experimental/numerical (c/d) result for relative brightness.

The results obtained are resumed in Figure 5.13. The experimental (Fig. 5.14 (a)) and numerical (Fig. 5.14 (b)) results for the absolute brightness show a continuous increase with increasing pump current and a stabilization plateau at larger pump currents after the introduction of PhC. The plot of relative brightness (figure 5.14 (c)) shows a maximum enhancement of 30% located at normalized pump current of 2.3 for the experimental case, while in the numerical case (figure 5.14 (d)), the maximum enhancement of 70% is located at normalized pump current 2. Both numerical and experimental results show good agreement regarding the dependence on the injection

current, although the large value of brightness enhancement predicted by the model was not achieved in the experiments.

5.4. Numerical optimization of filtering

The numerical analysis of the filtering in the extended cavity configuration performed with our simplified model showed a good agreement with the experimental results, both in the slit and in the PhC filtering scenarios, indicating that the model is capable of capturing the essential elements of the interaction. As a further step, we can use the model to analyze other situations where the effect of the filtering could be optimized. In this section, we discuss the results of brightness enhancement obtained by optimizing the filtering function of the PhC.

As we have seen in the previous discussions, the brightness enhancement obtained with intracavity slit were higher compared to those obtained using the PhC. This is due to the fact that the slit provides an extremely convenient transmission function due to the total extinction of the higher-order spatial modes while the central modes experience no losses. Since the goal of the thesis is to study the possibility of using PhC as filtering elements, to pave the way for a future possibility of implementing an integrated monolithic compact device with improved spatial beam quality, we will concentrate in the analysis of the possibilities of increasing the performance of the PhCs.

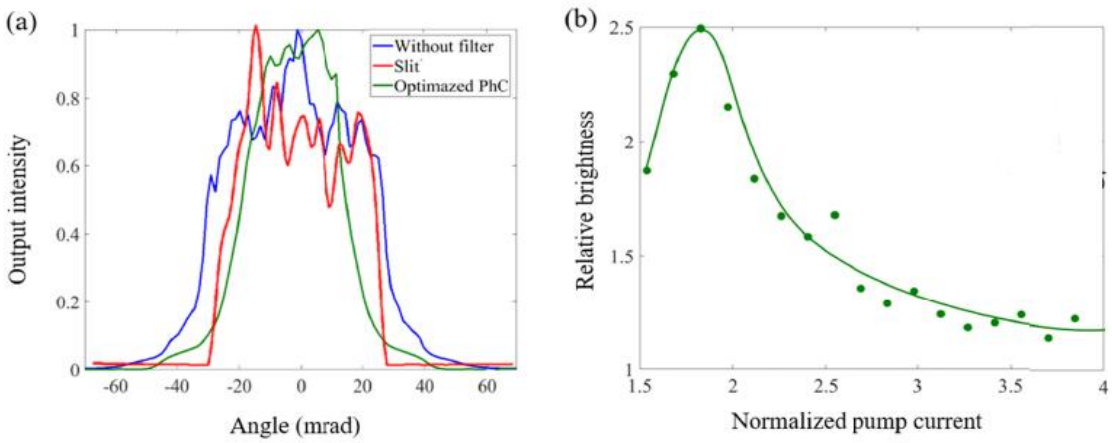

Fig. 5.15: (a) Far field profile of direct beam (blue), slit (red) and optimized PhC (green). The figure on right hand side (b) shows the relative brightness as function of normalized pump current.

The filtering function used so far was obtained from the experimental measurement of the fabricated samples. As a first step, we searched for a numerically optimized filtering function which could be later introduced as spatial filter in the model. The PhC was

optimized by adjusting the geometry factor (Q), chirp (dQ) and number of longitudinal periods (N_p) to obtain a transmission function approaching that of slit. The method by which this transmission function is obtained is the same as illustrated in figure 3.9. The optimization was performed by defining the relative brightness as the parameter of interest so we plotted it for different pump currents. The relative brightness could be enhanced by a factor of 2.5 times at normalized pump current around 2 [124] as seen in figure 5.15. The parameters used to obtain the optimized transmission function are Q =1.14, dQ = 0.25 and N_p = 73. The other parameters of numerical simulation are not changed.

The efficiency of the spatial filtering using PhCs can be further increased by modifying the filtering scheme. The geometry used in our experiments, and whose performance we have already demonstrated, is that placing the PhC at the front facet between the cavity mirror and output facet as shown schematically in fig. 5.16 (b). Other possible configurations that could be tested include geometries in which the PhC could be placed either at the rear facet (fig. 5.16 (a)) or placed at both facets (rear and front) as shown in fig. 5.16 (c).

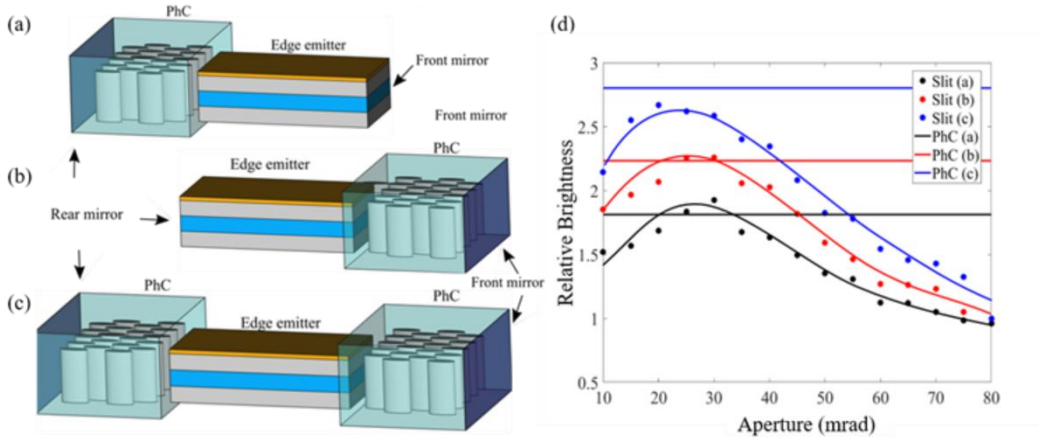

Fig. 5.16: Scheme of an integrated compact cavity configuration, with the filtering element (in the figures a PhC) at: (a) rear facet, (b) front facet, and (c) both facets. (d) Optimized filtering performance as compared to the slit.

The numerical simulations corresponding to these different geometries are resumed in Figure 5.16 (b). From this figure, we can observe that schemes with spatial filtering at the rear mirror always show smaller relative brightness than those with spatial filtering at the front mirror, while simultaneous filtering at both mirrors achieves the highest relative brightness. Slightly smaller values are attained for the optimized PhC located at the front and rear mirror while simultaneous PhCs at both mirrors reaches the maximum relative brightness enhancement even higher than the slit case. These results indicate the way to achieve a better optimization of our filtering scheme, even if new ways to

implement this geometry experimentally must be conceived and analyzed in detail to check its availability.

In this chapter, we demonstrated the spatial filtering effect in broad area laser using PhC and intracavity by exploring the effect of pump current and reflectivity of feedback mirror. The maximum enhancement in the brightness was by factor of 2 for intracavity slit and factor of 1.3 for PhC. The action of intracavity slit and PhC was numerically simulated by considering simple numerical model of BAS laser and transmission function of the PhC. The experimental and numerical results agree very well. At the end of the chapter, we show that the filtering efficiency can be further improved by numerically optimizing the filtering function of the PhC. An improvement in the relative brightness of the beam is observed. By using different filtering configuration, the brightness enhancement can be further increased. From the experimental results we clearly see that the results achieved with variable slit shows higher enhancement in the brightness of the beam compare to PhC. The PhC have edge over intracavity slit due to its compact size, which can fit inside the micro-optical device or into the resonator of microlaser. This will help to miniaturize the device. In this thesis we have not demonstrate monolithic integration due to technological problem, but it shows the potential for such integration in near the future.

Chapter 6

Spatial Filtering in Longer Cavity Laser

The active length of a semiconductor chip determines the output power from a diode laser, where longer cavities permit extracting higher output powers [125]. The standard diode laser bar, giving output powers of the order of hundreds of watt, has typical cavity lengths of 2-4 mm. This laser finds application in material processing. With increase in output power, the beam quality along the slow axis deteriorates and some filtering mechanisms, as the ones we are discussing on this thesis, could be useful to increase the quality of the laser output beam.

The previous discussions (experiment and numerical) so far were concentrated on spatial filtering in BAS laser considering cavity lengths of 1.5 mm and transverse widths of 400 μm. In addition, the front facet of the laser was low-AR coated, requiring external feedback mirror to start the lasing action. Here we consider another BAS laser with longer cavity length, shorter transverse width, and increased output power. In this last chapter, we demonstrate spatial filtering in longer cavity BAS laser using intracavity slit and PhC. Only the experimental results will be discussed in this chapter.

6.1. Experimental setup of longer cavity laser

The laser has a transverse width of 100 µm along the slow axis and an active cavity length of 4 mm. The front facet of the emitter has a 4 % reflectivity, while the coating on the other facets gives a reflectivity of 95 %. Contrary to our previous system, this BAS emitter shows laser emission on its own without any external feedback mirror. The possibility to use the PhC filter directly at the output of the laser, performing a single-pass transmission filtering, could be tested to get an improved spatial profile. However, as we said earlier, the single pass scheme does not bring any enhancement in the brightness. Therefore, we will use the same idea of intracavity filtering approach, by placing an external mirror and allowing for multiple passes of the radiation acting on the PhC or filtering scheme. To test this PhC placed in the near field, we have followed the same technique of extended cavity used with the previous laser. The scheme of extended cavity arrangement is as shown in fig. 6.1. The experimental configuration remains the same, except the front facet, which now has a reflectivity of 4%.

The cavity is characterized by measuring its output power, spectrum, and profile in the near field and far field plane with and without external feedback mirror.

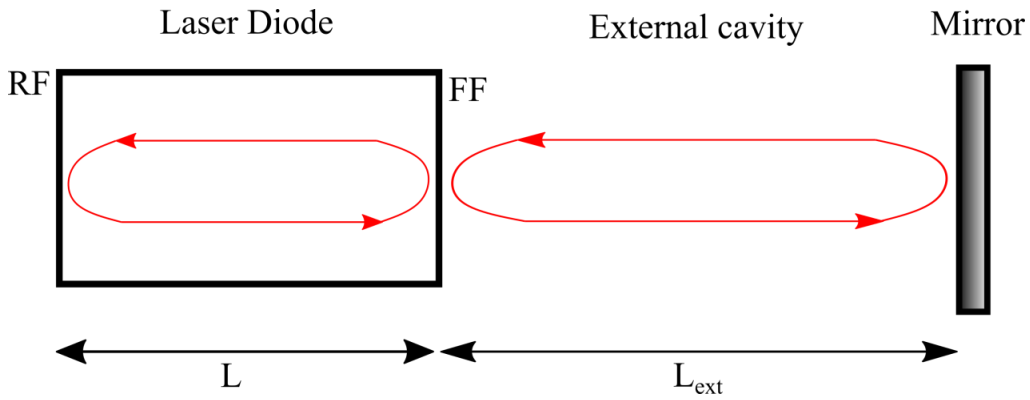

Fig. 6.1: Schematic of external cavity laser. RF denotes rear facets and FF denotes front facets.

Since the front facet of this laser is 4% coated, it does not require an external feedback mirror to lase, but to employ the intracavity spatial filtering we built the extended cavity. The direct emission as observed on IR card at distance of around 8 cm from the laser is shown in Figure 6.2. We see that the size of the beam is quite small compared to the previously discussed emitter (see fig. 4.7). Due to the smaller size of the beam, we used smaller dimension lenses to build the cavity, allowing for more compact external cavity and reduced aberration effects by the lenses. The cylindrical lens with length of 60 mm, height of 30 mm and focal length of 50.79 mm were used.

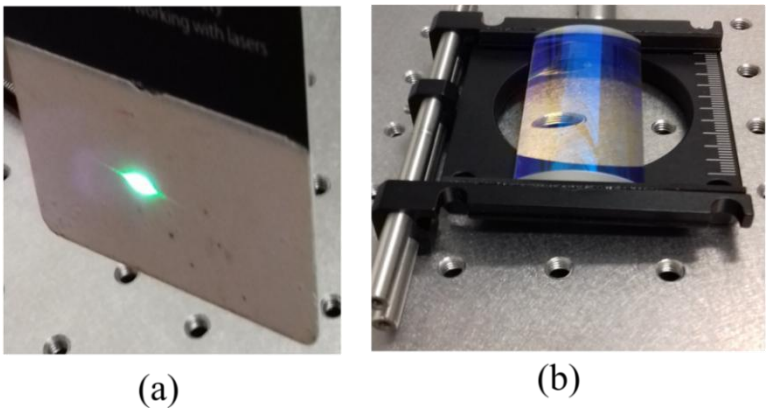

Fig. 6.2: (a) Output beam on IR card and (b) cylindrical lens used.

The experimental setup remains similar as discussed in chapter four except that the BAS emitter has 4% coating on front facet.

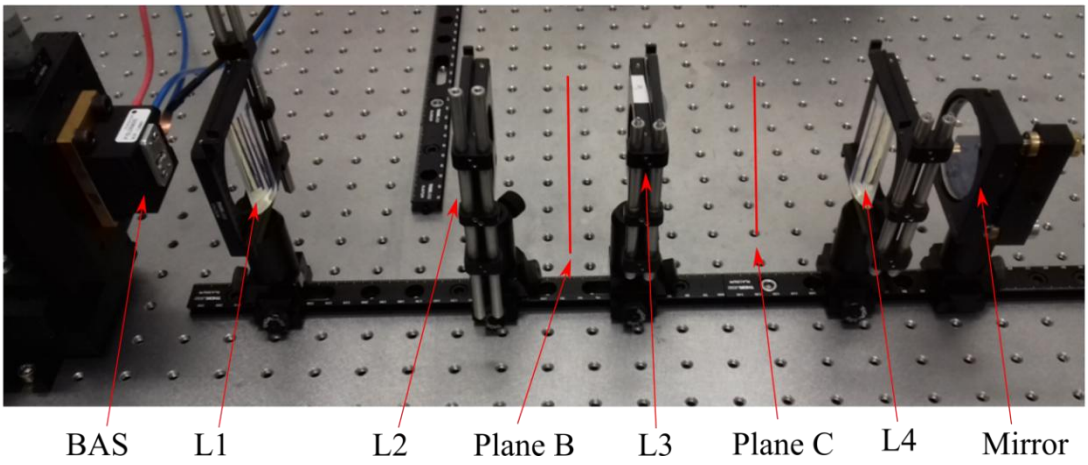

Fig. 6.3: Experimental setup of extended cavity using longer cavity laser. L1-L4 are cylindrical lenses.

We first characterized the cavity by measuring the output power and profile with and without feedback. The L-I curve is shown in fig. 6.4 (a). The threshold current without any feedback is 0.63 A and it reduces to 0.57 A with introduction of feedback mirror. The output power is measured in pulsed mode with same duty cycle, pulse width and repetition rate as discussed in chapter 4. In the continuous wave (CW) mode, the output power is close to 10 W, where as in pulsed mode it close to 2.5 W.

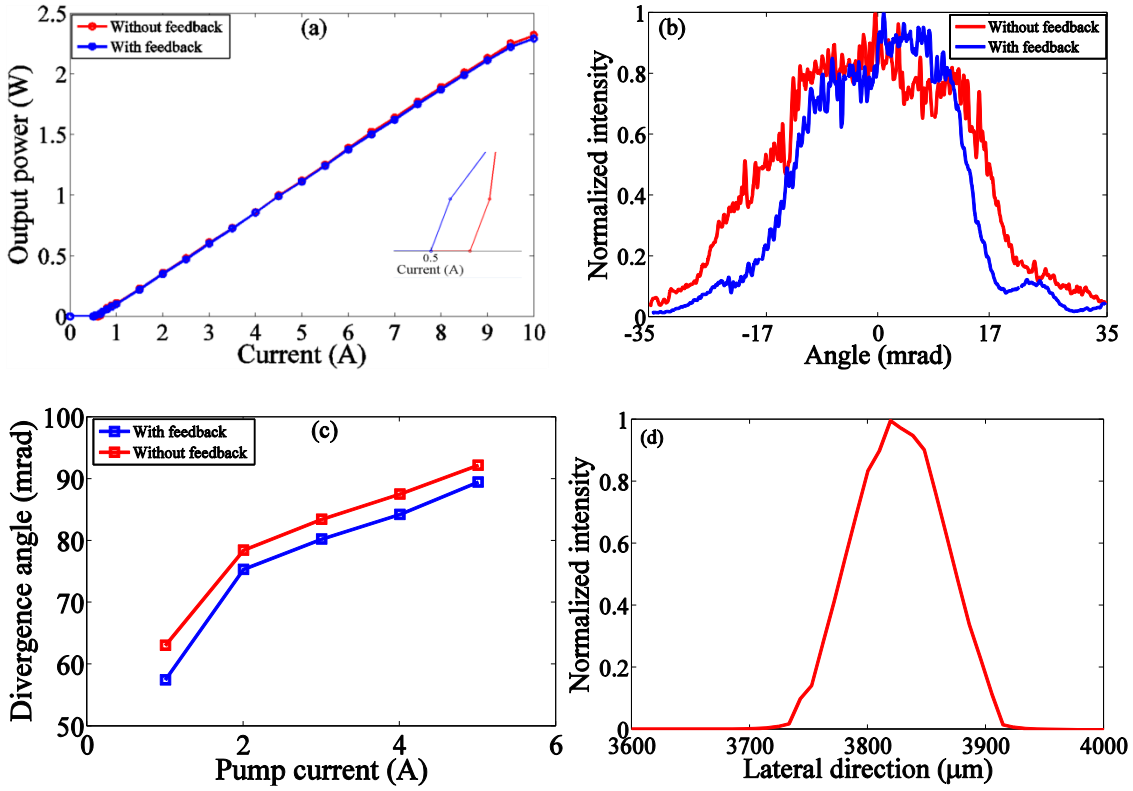

Fig. 6.4: (a) L-I curve (b) far field profile (c) divergence angle (d) near field.

The far field profile is measured with and without feedback mirror. The profile was recorded at 1 A pump current. We observed slight reduction in the far field profile when feedback mirror was introduced as shown in fig. 6.4 (b). This acts as spatial filter eliminating some higher order modes. The same is observed with increasing the pump current. The reduction in the divergence angle with and without feedback mirror for different pump current values is plotted in fig. 6.4 (c). The near field profile is shown in figure 6.4 (d).

6.2. Spatial filtering using variable slit

The experimental setup of intracavity slit remains identical as the one discussed in section 4.3.1. The variable width slit is placed in the far field plane (plane C shown in figure 6.3). The working principle of slit is already explained in section 4.4.1. The output radiation is focused using 100 mm focal length plano-convex lens, measuring the beam diameter at different position along propagation distance and fitting the data with beam waist equation. Based on these measurements, the beam quality factor (M_x^2) was calculated. The corresponding brightness is calculated using formula (21). The M_x^2 values initially changes slowly for all pump current when the aperture was wide open

and after certain values it starts to decrease as seen in figure 6.5 (a). By closing the slit, the M_x^2 reduces and the beam quality increases. The corresponding brightness values for different pump current are plotted in figure 6.5 (b). The brightness value increases reaches maximum value and after it decrease again. A comparison of the results obtained with this laser and with the previous results of chapters 4 and 5 shows that the dependence of the M^2 factor with the slit width is not decreasing linearly as shown in the previous discussions. In particular, for larger values of the aperture, a constant value of M^2 is measured indicating that the aperture has no effect on the beam for these values. This is consistent with the reduced angular bandwidth of the beam in the far-field, indicating that at these values of the slit width, no cutting of the far-field modes is obtained.

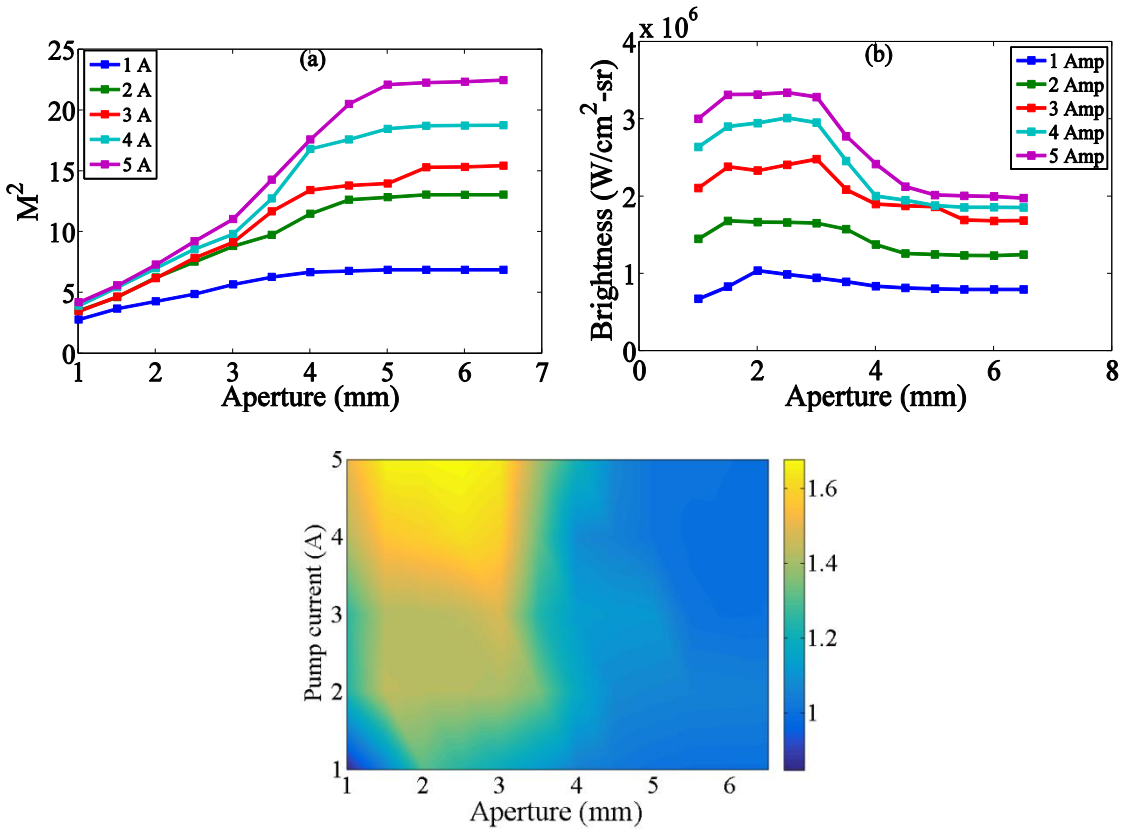

(c)

Fig. 6.5: Shows the results of improvement in the (a) beam quality factor (M_x^2) and (b) absolute brightness of beam and (c) relative brightness map.

6.3. Photonic crystal spatial filtering

The photonic crystal (PhC) works only in the near field plane and it is place in plane B as shown in fig. 4.20. The PhC works by deflecting the higher angular component from beam.

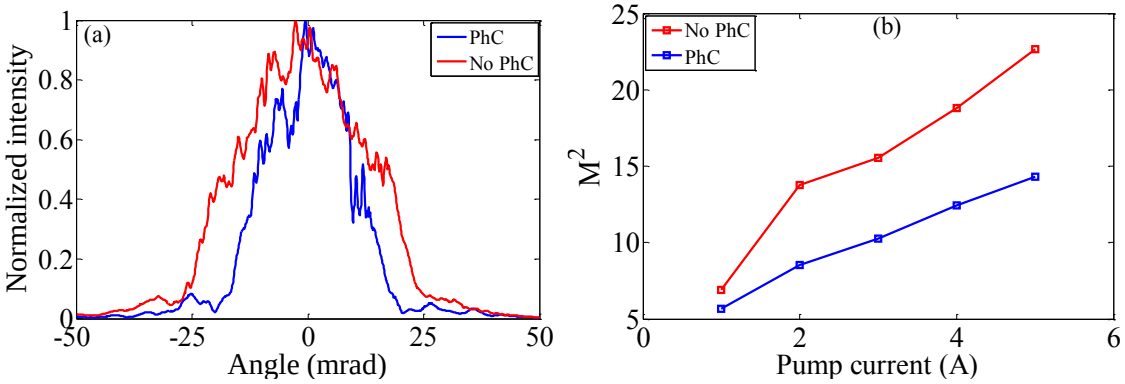

Fig. 6.6: (a) The effect of PhC can be observed on the far field profile, (b) The reduction of M^2 for different pump current when the PhC were introduced inside the cavity, (c) brightness of the beam.

The far field profile with and without PhC is shown in fig. 6.6 (a). A clear difference is seen in the reduction of far field divergence angle. We calculated the M_x^2 for both beam and observed reduction as shown in fig. 6.6 (b).

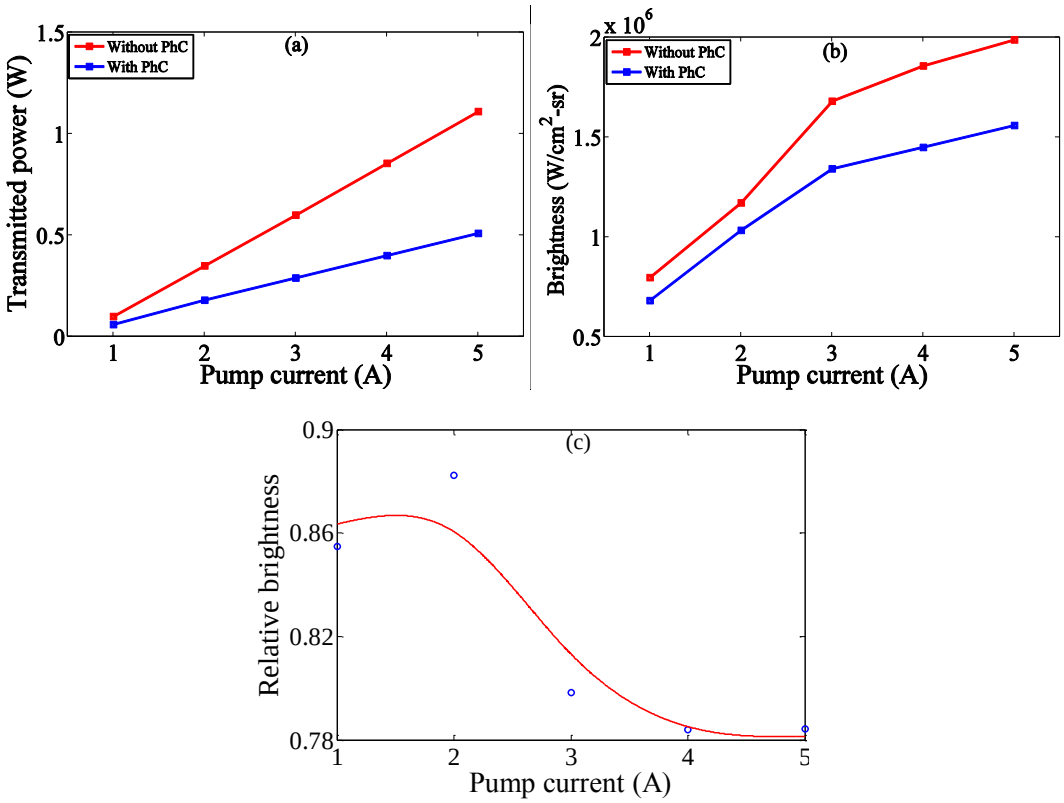

Fig. 6.7: (a) The transmitted power through the PhC, (b) the corresponding absolute brightness and (c) relative brightness.

The results of spatial filtering in longer cavity length BAS shows improvement in the beam quality factor (M_x^2) and reduction of the far-field bandwidth. However, we do not

observe any enhancement in the brightness due to the significant amount of loss in the optical power.

In this chapter, we demonstrate beam quality improvement in longer cavity length BAS laser using the slit filtering configuration. We studied the effect of external feedback in these lasers using an external mirror providing a 4% reflectivity, showing a reduction of both the threshold current and the far field divergence angle. To study the filtering effect in this laser, we used the extended cavity configuration. We tested the action of the intracavity variable slit in the far field plane and the effect of the PhC on the beam profile. Using PhC, the M_x^2 of the beam improves, but we do not see any enhancement in the brightness. This could be due to large loss in the optical power along with the removal of higher order modes. The brightness could be further increased by using optimized PhC configurations as those studied in the previous chapter.

Chapter 7

Conclusion and future work

7.1. Conclusions

In this chapter, we will summarize the main results that we have presented in this PhD thesis together with some possible directions, which could be followed in a future work.

The main objective of this thesis was to demonstrate the possibility to improve the beam quality of high-power edge emitting broad area semiconductor lasers by the use of intra-cavity spatial filtering based on photonic crystals. These kinds of lasers suffer from poor beam quality due to the multi-mode emission in the transverse direction the, so called, slow axis. The main motivation, hence, is the possibility to perform a spatial filtering in this laser to decrease its divergence and increase the brightness of the beam. For this purpose, we consider single emitter broad area laser having large beam quality factor (M^2) along the slow axis. The conventional spatial filtering schemes, acting in the far-field are not adequate to be implemented in a monolithic integration scheme which would help to miniaturize the size of the device. Some of the techniques proposed up to now didn't satisfy the criterion of brightness enhancement. The brightness emitted by a laser corresponds to the power emitted per unit area and unit solid angle and can be used to define the spatial quality of a beam. In this thesis, we tested experimentally the possibility to use photonic crystals to filter the large-order transverse modes from the laser to reduce its divergence and increase its brightness.

The role of the photonic crystal is to deflect the high-order modes out of the propagation direction. By applying this filtering inside the laser cavity, the energy lost by these modes can be coupled to other lower-order modes modifying the emission characteristics of the laser and decreasing its divergence and consequently its M^2-factor.

The typical values of M^2-factors for these kinds of lasers can exceed 50 in the slow axis being close to 1 in the fast axis instead. These differences give rise to high asymmetric beams with elliptical shape. Moreover, the larger the M^2-factor the larger will be the size of the spot that can be achieved using tight focusing optics. This fact makes more difficult the coupling of the laser output into optical fibers limiting their performance and their use for certain applications.

The proposals of spatial filtering out of the laser cavity reported in the literature didn't achieve the increase in brightness desired due to the power loss resulting from the filtering process. The advantage of the use of photonic crystals is that they operate in the near field and, hence, could be mounted, for instance, at the output facet of the semiconductor material leading to a very compact device. Some preliminary numerical simulation results published recently [104] reported the possibility of beam quality improvement by the use of photonic crystals. The first difficulty found in the realization of this idea is that a monolithic integration does not give the possibility to test different filters and, at the same time, its implementation is a very challenging task from the technological pint of view. Our approach to solve this problem was to take profit of the possibility to change the reflectivity of one of the semiconductor material facets by placing anti-reflection coating to construct and extended laser cavity allowing to test experimentally different filtering possibilities.

The use of photonic crystals and its spatial dispersion effects to achieve spatial filtering has been discussed extensively in the literature during the last 10 years. The use of photonic crystals allows to deflect (either in reflection or transmission configurations) the radiation incident on them whose wave vector belongs to a certain angular range. Depending if the propagation of the diffracted components goes in the backward or forward direction, this can be classified into Bragg or Laue regime. The PhC used in our experiment operates in the Laue regime. The advantage of spatial filtering in Laue regime is that it does not require longitudinal periods shorter than the wavelength of light, allowing for an easier fabrication process. At the same time, since 1D PhC are not suitable to achieve filtering at angles smaller than 1º, the use of 2D photonic crystals was selected, following the results obtained in the spatial filtering with photonic crystals in recent publications [71, 82-83].

The fabrication of crystals using femtosecond laser beam offers advantages in terms of low heat dissipation and fabrication control. The first PhCs used in the experimental work were fabricated by direct laser writing technique using femtosecond laser beam with Gaussian profiles but an improvement of the filtering results was achieved using Bessel beams to inscribe the PhC on N-BK7 glass substrate. The advantage of Bessel beam over the more conventional Gaussian beam technique is that the use of Bessel beams allows the fabrication of longer length PhCs, which results in a better filtering performance. The introduction of chirp in the longitudinal direction allowed to control

the width of the filtering region for an optimum operation. Two different PhCs were fabricated with different geometry factor, chirp, and number of longitudinal periods.

The optimum parameters for the PhCs were selected by performing a simulation of the single pass transmission function through PhC, using a numerical model based in a split step method, which calculates the scattering on a phase mask corresponding to the refractive index modulated layers and the diffractive propagation between the layers. We investigated the filtering performance by varying the chirp and number of longitudinal periods.

The extended cavity configuration designed and mounted for the experimental study of the filtering by PhCs is the main contribution of this thesis. It consists of a double 4*f* system providing a way to obtain conjugated planes of the output facet of the semiconductor material. The advantages of the extended cavity scheme are that it allows placing the PhC setup inside our laser cavity acting in the near-field plane and test the operation of different PhCs and, at the same time, gives the possibility to compare the filtering results with those using a confocal filtering technique using a slit in the far-field.

The setup was characterized by measuring output power, spectrum, and near-field and far-field laser profiles. The M^2-factor measurement was implemented in our setup from the measurement of the beam waist radius and beam divergence angle. The first demonstration of spatial filtering was obtained using the intracavity slit configuration in the far field domain and a feedback mirror of 4% reflectivity. The measurement of the output power and M^2 factor allows to obtain the brightness of the beam. The action of the slit width reduction results in a reduction of the beam divergence by the elimination of the higher-order transverse modes. However, the reduction in M^2 factor is not always related to an increase of the brightness due to the unavoidable power loss by the filtering action. Our measurements show that for the slit case an increase of the brightness proportional to the injection current is observed. The improvement in the beam quality can be quantified by calculating the brightness enhancement factor, which gives the ratio between the brightness of the filtered beam to that of the unfiltered case. Our measurements demonstrated an enhancement factor of 2 in the case of slit filtering. The best performance is obtained at slit widths values where the two opposite trends of divergence reduction and power loss provide the optimum operation.

The measurement of the relative brightness enhancement replacing the slit by the PhC reported a maximum enhancement in brightness by factor of 1.5. This result constitutes the first demonstration of brightness enhancement by the use of photonic crystals and is one of the main results of this thesis. Even if the improvement obtained with the PhC does not perform better than the slit, it gives a very promising result in our goal of achieving efficient beam quality improvement in a compact configuration. The

reduction of the far-field mode constant results in a slight change of the near-field profile, which gets smoother as the filtering action is increased.

After the demonstration of the possibility of beam quality improvement by PhC filtering was achieved, the search for the optimum operation conditions was performed by studying the dependence of the relative brightness on the reflectivity of the feedback mirror and the value of the pump current. We used three different reflectivities (4%, 6%, and 8%) of the feedback mirror while the pump current was varied from 2 A to 5 A. The maximum brightness enhancement obtained was two for the intracavity slit and 1.3 for the PhC. The change of reflectivity of the feedback mirror didn't report a substantial change in the filtering action of the system. This fact confirms the possibility to use the studied filtering in these systems irrespective of the value of the reflectivity of their output facet.

We numerically simulated the action of the slit and of the PhC by considering a simple numerical model for the BAS laser. The model includes spatial-temporal evolution of field propagation and carriers. The numerical simulation of spatial filtering using PhC is achieved by using the transmission function obtained from the data of experimental measurement. This filtering function was introduced in the laser model to simulate the filtering action. The results obtained with our numerical simulation shows good agreement with the experimental ones both considering the slit and the PhC filtering. The use of this model allowed us to further explore the spatial filtering using PhC by numerically optimizing the filtering function. The results indicate that the brightness can be further enhanced by a factor of 2.5. By changing the intracavity configuration, and placing the PhC filter on both mirrors, brightness enhancement has been achieved.

Additionally, we demonstrated the spatial filtering in the longer cavity length laser having 4% reflective coating on the front facet. The study of spatial filtering was performed for single reflectivity (4%) of feedback mirror. We demonstrate beam quality improvement by decrease in M_x^2 value and increase in brightness using intracavity slit; however, no increase in brightness was observed using the PhC filtering, due to the large loss in optical power. At higher pump currents, the thermal effect inside the laser cavity dominates preventing the filtering of higher order modes.

Concluding, we have demonstrated spatial filtering in broad area semiconductor laser using a PhC spatial filter in extended cavity configuration, which mimics the compact cavity configuration. The main result was a reduction of the beam divergence and the brightness enhancement of the emitted radiation. Comparison with the conventional confocal filtering technique shows that by using PhCs filtering, one can achieve results approaching the same values of spatial beam quality improvement. This is the first test to demonstrate the working principle of spatial filtering in Broad Area Laser with single emitter with output power of the order of 1W. The same principle can be applied to high power diode laser bars. The added advantage of the use of PhCs filtering comparing

with the conventional technique is that it offers the possibility of integration of the PhC into the BAS leading to a serious breakthrough in regimes of high-power emission. We showed the beam quality improvement by decreasing the M^2 values and increasing the brightness of the beam. In addition, the experimental results were compared with the numerical simulation and both are in agreement. We also explored the possibility of improvement in spatial filtering using PhC when placed on both side of the mirror. By employing PhC at both ends of BAS, the brightness can be further enhanced. This thesis does not demonstrate such integration due to limited technologies, however, it shows the potential for such integration in near future, by proving the physical principles.

7.2. Future work

The work we presented here offers some possibilities for improvement in the future:

1) The implementation of the compact cavity configuration could be the possible future work in which the PhC will be placed directly between the front facet and cavity mirror.

2) Continuing with compact cavity configuration, some preliminary numerical results have showed that by changing the intracavity filtering scheme in which PhC placed at both facets of the laser can further improve the filtering efficiency.

3) Fabrication of new Bessel beam PhC based on the results obtained by numerical optimization of the filtering function.

4) The beam characterization requires frequent M^2measurement, which is time consuming. We can automatize the process by scanning the beam profile using optical fiber along both axes with high precision motors. The advantage of using optical fiber that it can handle high optical power from laser bar or stacks.

5) It is also interesting to couple spatially filtered radiation into low numerical aperture optical fiber.

6) In future, we would like to see the effect of PhC spatial filter fabricated by physical vapor deposition technique.

References

[1] V. V. Popovichev, E. I. Davydova, A. A. Marmalyuk, A. V. Simakov, M. B. Uspenskii, A. A. Chel'nyi, A. P. Bogatov, A. E. Drakin, S. A. Plisyuk and A. A. Stratonnikov, "High-power single-transverse-mode ridge optical waveguide semiconductor lasers", Quantum Electronics, 32, 12 (2002).

[2] S. Zhouping, L. Qihong, D. Jingxing, Z. Jun, Wei Runrong, "Beam quality improvement of laser diode array by using off-axis external cavity", Optics express 12, 11776 (2007).

[3] M. Chi, N.-S. Bøgh, B. Thestrup and P. M. Petersen, "Improvement of the beam quality of a broad-area diode laser using double feedback from two external mirrors," Applied Physics Letter, 85, 1107-1109 (2004).

[4] E. Samsøe, P. E. Andersen, S. A-Engels, P. M. Petersen, "Improvement of spatial and temporal coherence of a broad area laser diode using an external-cavity design with double grating feedback," Opt. Express 12, 609 (2004).

[5] S. Yiou, F. Balembois, and P. Georges, "Improvement of the spatial beam quality of laser sources with an intracavity Bragg grating", Optics Letter 28, 4, (2003).

[6] X. Gao, Y. Zheng, H. Kan and K. Shinoda, "Effective suppression of beam divergence for high-power laser diode bar by an external-cavity technique", Optics Letters, 29, 4 (2004).

[7] J. P. Leidner and J. R. Marciante, "Beam Quality Improvement in Broad-Area Semiconductor Lasers via Evanescent Spatial Filtering", IEEE Journal of Quantum Electronics, 48, 1269 – 1274 (2012).

[8]**.** M. Mikulla, A. Schmitt, P. Chazan, A. Wetzel, M. Waither, R. Kiefer, W. Pletschen, J. Braunstein, and G. Weimann, "Improved Beam Quality for High Power Tapered Laser Diodes with LMG (Low Modal Gain)-Epitaxial Layer Structures", Proc. SPIE 3284 pp 72-79, (1998).

[9] R. Herrero, M. Botey, M. Radziunas, K. Staliunas, "Beam shaping in spatially modulated broad-area semiconductor amplifiers", Optics letters 37, 24, (2012).

[10] R. N. Hall, G. E. Fenner, J. D. Kingsley, T. J. Soltys, and R. O. Carlson, "Coherent light emission from GaAs junction" Physical Review Letter, 9, 9 (1962).

References

[11] Holonyak, Jr., N. and S. F. Bevacqua, Coherent (visible) light emission from $Ga(As_{1-x}P_x)$ junctions, Applied Physics Letter, 1, 82–83, 1962.

[12] Nathan, M. I., W. P. Dumke, G. Burns, F. H. Dill, Jr., and G. Lasher, Stimulated emission of radiation from GaAs p-n junctions, Applied Physics Letter, 1, 62–64, 1962.

[13] T. H. Maiman, Nature, 187, 493–494 (1960).

[14] L. Li, "The advances and characteristics of high-power diode laser materials processing", Optics and Lasers in Engineering, 34, 231-253 (2000).

[15] André Müller, Sebastian Marschall, Ole Bjarlin Jensen, Jörg Fricke, Hans Wenzel, Bernd Sumpf, and Peter E. Andersen, "Diode laser based light sources for biomedical applications", Laser Photonics Rev. 7, No. 5, 605–627 (2013).

[16] D. Botez and G. Herskowitz, "Components for Optical Communications Systems: A Review", Proceedings of the IEEE, VOL. 68, NO. 6, JUNE 1980.

[17] W. Koechner, *Solid-State Laser Engineering* (Springer, Berlin).

[18] M. C. Teich, B. E. A. Saleh, *Fundamentals of Photonics.* Wiley, New York.

[19] P. Y. Yu and M. Cardona, *Fundamentals of Semiconductors,* Springer-Verlag, Berlin, 1996.

[20] R. Diehl, *High-power diode laser, fundamentals, technology, applications*, Springer-Verlag, Berlin (2000).

[21] P**.** Basu, *Semiconductor Laser Theory*. 10.1201/b18634, (2015).

[22] C. Fabry and A. Pérot, "Théorie et applications d'une nouvelle méthode de spectroscopie interférentielle," Ann. de Chim. et de Phys. 16(7), 115–144 (1899).

[23]. P. Ressel, G. Erbert, U. Zeimer, K. Häusler, G. Beister, B. Sumpf, A. Klehr, and G. Trankle, "Novel Passivation Process for the Mirror Facets of Al-Free Active-Region High-Power Semiconductor Diode Lasers," *IEEE Photonics Technology Letters*, vol. 17, no. 5, May 2005.

[24]. P.V. Bhore, A.P. Shah, M.R. Gokhale, S. Ghosh, A. Bhattacharya, B.M Arora, "Effect of facets coating on the laser diode characteristics", Indian Journal of Engineering and Material Science, Vol. 11, pp 438-440, Oct 2004.

[25] L. Goldberg, H. F. Taylor, A. Dandridge, J. F. Weller, and R. O. Miles, "Spectral characteristics of semiconductor lasers with optical feedback," *IEEE J. Quantum Electron*, vol. QE-18, pp. 555–563, 1982

[26] D. Botez, L.J. Mawst, A. Bhattacharya, J. Lopez, J. Li, T.F. Kuech, V.P. lakovlev, G.I. Suruceanu, A. Caliman and A.V. Syrbu, "66% CW wallplug efficiency from Al-free 0.98pm-emitting diode lasers", Electronics Letters, 32, 21 (1996).

[27] M. Kanskar, M. Nesnidal, S. Meassick, A. Goulakov, E. Stiers, Z. Dai, T. Earles D. Forbes, D. Hansen, P. Corbett, L. Zhang, T. Goodnough, L. LeClair, N. Holehouse D. Botez and L.J. Mawst, "Performance and Reliability of ARROW Single Mode & 100μm Laser Diode and the Use of NAM in Al-free Lasers", Proc. SPIE, Optoelectronics 2003, Novel in plane Semiconductor Lasers II, 2003, 4995, pp 196-208.

[28] J. R. Marciante, G. P. Agrawal, "Nonlinear mechanisms of filamentation in broad-area semiconductor lasers", Journal of Quantum Electronics, 32, 590–596 (1996).

[29] T. Numai, *Fundamentals of semiconductor laser*, Springer Series in Optical Sciences, Volume 93. ISBN 978-0-387-40836-1. (Springer-Verlag New York, Inc., 2004).

[30] A. Baranov and E. Tournie, *Semiconductor Lasers: Fundamentals and Applications*, Sawston, U.K.: Woodhead Publishing, 2013.

[31] S. Haiyin, *A Practical Guide to Handling Laser Diode Beams*, 10.1007/978-94-017-9783-2. (2015).

[32] H. Wenzel, F. Bugge, M. Dallmer, F. Dittmar, J. Fricke, K.H. Hasler, and G. Erbert, "Fundamental-Lateral Mode Stabilized High-Power Ridge-Waveguide Lasers with a low beam divergence," IEEE Photonics Technology Letters 20, 214 – 216 (2008).

[33] K. Paschke, B. Sumpf, F. Dittmar, G. Erbert, Member, IEEE, J. Fricke, A. Knauer, S. Schwertfeger, H. Wenzel, and G. Tränkle, "Nearly-diffraction limited 980nm tapered diode lasers with an output power of 6.7 W", IEEE 19th International Semiconductor Laser Conference, Conference Digest (2004.)

[34] K. J. Paschke, S. Einfeldt, A. Ginolas, K. Hausler, P. Ressel, B. Sumpf, H. Wenzel, and G. Erbert, "15 W Reliable Operation of 96 - μm Aperture Broad-Area Diode Lasers Emitting at 980 nm," in CLEO/QELS 2008 Conference Digest p. CMN4 (2008).

[35] M. Kanskar, T. Earles, T. J. Goodnough, E. Stiers, D. Botez and L. J. Mawst, "73% CW power conversion efficiency at 50 W from 970 nm diode laser bars", Electronics Letters, 41, 5 (2005).

[36] S. Gawali, D. Gailevičius, G. Garre-Werner, V. Purlys, C. Cojocaru, J. Trull, J. Montiel-Ponsoda, and K. Staliunas, "Photonic Crystal Spatial Filtering in Broad Aperture Diode laser", Appl. Physics Letters, 115, 141104 (2019).

[37] P. Crump, G. Blume, K. Paschke, R. Staske, A. Pietrzak, U. Zeimer, S. Einfeldt, A. Ginolas, F. Bugge, K. Häusler, P. Ressel, H. Wenzel, G. Erbert, "20W continuous wave reliable operation of 980 nm broad-area single emitter diode lasers with an aperture of 96μm," in SPIE proceedings High-Power diode laser technology application VII, vol. 7198, no. 14, p. 9, 2009.

[38] H. Liu, X. Liu, L. Xiong, and W. Zhao, *Packaging of High Power Semiconductor Lasers*, Springer, 2014.

[39] H. Li, I. Chyr, X. Jin, F. Reinhardt, T. Towe, D. Brown, T. Nguyen, M. Berube, T. Truchan, D. Hu, R. Miller, R. Srinivasan, T. Crum, E. Wolak, R. Bullock, J. Mott, and J. Harrison, ">700W continuous-wave output power from single laser diode bar," Electron. Lett. 43(1), 27–28 (2007).

[40] R. Pandey, D. Merchena, D. Stapletona, S. Patterson, "Advancements in high-power diode laser stacks for defense applications", SPIE Proceedings Vol. 8381 (2012).

[41] T. Y. Fan, "Laser Beam Combining for High-Power, High-Radiance Sources", IEEE Journal of Selected Topics in Quantum Electronics, VOL. 11, NO. 3, (2005).

[42] A. E. Siegmann, "New developments in laser resonators," *Proc. SPIE,* vol. 1224, pp. 2–14, 1990.

[43] International Organization for Standardization. (2005). Lasers and laser-related equipment — Test methods for laser beam widths, divergence angles and beam propagation ratios — Part 1: Stigmatic and simple astigmatic beams (ISO 11146-1:2005).

[44] A. Forbes, L. Burger, and L. Igor Anatolievich "Modelling laser brightness from cross Porro prism resonators", Laser beam shaping VII. Proc. SPIE2006; 6290(62900):M2– 8.

References

[45] B. Sumpf, K.-H Hasler, P. Adamiec, F. Bugge, F. Dittmar, J. Fricke, H. Wenzel, M. Zorn, G. Erbert, and G. Tränkle, “High-Brightness Quantum Well Tapered Lasers”, IEEE Journal of selected topics in quantum electronics, 15, 3 (2009).

[46] J. W. S. Rayleigh (1888), "On the remarkable phenomenon of crystalline reflexion described by Prof. Stokes"265, doi:10.1080/14786448808628259.

[47] V. P. Bykov (1972), "Spontaneous Emission in a Periodic Structure", Soviet Journal of Experimental and Theoretical Physics, 35: 269– 273.

[48] V. P. Bykov (1975), "Spontaneous emission from a medium with a band spectrum", Quantum Electronics, 4 (7): 861–871.

[49] K. Ohtaka (1979), "Energy band of photons and low-energy photon diffraction", Physical Review B, 19 (10): 5057–5067.

[50] E. Yablonovitch, “Inhibited spontaneous emission in solid-state physics and electronics”, Physical Review Letters 58, 2059 (1987).

[51] S. John, “Strong localization of photons in certain disordered dielectric super lattices”, Physical Review Letters 58, 2486 (1987).

[52] S. Foteinopoulou, E. N. Economou, and C. M. Soukoulis, “Refraction in media with a negative refractive index,” Phys. Rev. Lett. 90, 107402 (2003).

[53] M. F. Yanik, W. Suh, Z. Wang, and S. Fan, “Stopping light in a waveguide with an all-optical analog of electromagnetically induced transparency,” Phys. Rev. Lett. 93, 233903 (2004).

[54] K. Hirose, Y. Liang, Y. Kurosaka, A. Watanabe, T. Sugiyama and S. Noda “Watt-class high-power, high-beam-quality photonic-crystal lasers”, Nature Photonics, 8, 406–411 (2014).

[55] D. A. Mazurenko, R. Kerst, J. I. Dijkhuis, A. V. Akimov, V. G. Golubev, D. A. Kurdyukov, A. B. Pevtsov, and A. V. Selkin, “Ultrafast optical switching in three-dimensional photonic crystals”, Physical review letter, 91, 213903 (2001).

[56]. J. D. Joannopoulos, R.D. Meade, J.N. Winn, and S. Johnson, Photonic crystals Molding the flow of light (Princeton Univ. Press, 1995).

References

[57] C.-R. Yang, Y.-S. Hsieh, G.-Y. Hwang, and Y.-D. Lee, "Photoablation characteristics of novel polyimides synthesized for high-aspect-ratio excimer laser liga process", Journal of Micromechanics and Microengineering 14, 480 (2004).

[58] C. Kraeh, A. Popsecu, M. Schieber, H. Hedler, T. Bieniek, G. Wielgoszewski, M. Moczała, and J. Finley, "Fabrication of high aspect ratio microtube arrays for 2D photonic crystals", Materials Research Express 1, 026201 (2014).

[59] A. Ovsianikov, J. Viertl, B. Chichkov, M. Oubaha, B. MacCraith, I. Sakellari, A. Giakoumaki, D. Gray, M. Vamvakaki, M. Farsari, and C. Fotakis, "Ultra-low shrinkage hybrid photosensitive material for two-photon polymerization microfabrication", ACS Nano 2, 2257 (2008).

[60] K. Staliunas and R. Herrero, "Nondiffractive propagation of light in photonic crystals", Phys. Rev. E 73, 016601.

[61] T Lu, W. Peng, S. Zhu and D. Zhang, "Bio-inspired fabrication of stimuli responsive photonic crystals with hierarchical structures and their applications", Nanotechnology 27, 122001(2016).

[62] J. W. Galusha, L. R. Richey, M. R. Jorgensen, J. S. Gardner, and M. H. Bartl, "Study of natural photonic crystals in beetle scales and their conversion into inorganic structures via a sol-gel bio-templating route", Journal of Materials Chemistry 20, 1277 (2010).

[63] D. W. Lee. Iridescent blue plants. American Scientist 85, 56 (1997).

[64] A. E. Seago, P. Brady, J-P. Vigneron and T. D. Schultz, "Gold bugs and beyond: a review of iridescence and structural colour mechanisms in beetles (Coleoptera)", J. R. Soc. Interface (2009) 6, S165–S184.

[65] K. Michielsen, H. De Raedt, and D. G. Stavenga, "Reflectivity of the gyroid biophotonic crystals in the ventral wing scales of the Green Hairstreak butterfly, Callophrys rubi", J. R. Soc. Interface (2010) 7, 765–771.

[66] E. Yablonovitch, T. J. Gmitter, and K. M. Leung, "Photonic band structure: The face-centered-cubic case employing nonspherical atoms", Physical Review Letters 67, 2295 (1991).

References

[67] R. F. Cregan, B. J. Mangan, J. C. Knight, T. A. Birks, P. S. J. Russell, P. J. Roberts, and D. C. Allan, "Single-mode photonic band gap guidance of light in air", Science 285, 1537 (1999).

[68] A. Frölich, J. Fischer, T. Zebrowski, K. Busch, and M. Wegener, "Titania woodpiles with complete three-dimensional photonic bandgaps in the visible", Advanced Materials 25, 3588 (2013).

[69] E. Yablonovitch, "Photonic band-gap structures", Journal of the Optical Society of America B 10, 283 (1993).

[70] K. M. Ho, C. T. Chan, and C. M. Soukoulis, "Existence of a photonic gap in periodic dielectric structures", Physical Review Letters 65, 3152 (1990).

[71] L. Maigyte and K. Staliunas, "Spatial filtering with photonic crystals", Applied Physics Reviews 2, 011102 (2015).

[72] R. Wang, J. Dong, and D. Y. Xing, "Defect studies in a one-dimensional photonic band gap structure", physica status solidi (b) 200, 529 (1997).

[73] Z. Lu, S. Shi, J. Murakowski, G. Schneider, C. Schuetz, and D. Prather, "Experimental Demonstration of Self-Collimation inside a Three Dimensional Photonic Crystal", Phys. Rev. Lett. 96**,** 17, 173902 (2006).

[74] H. Kosaka, T. Kawashima, A. Tomita, M. Notomi, T. Tamamura, T. Sato, and S. Kawakami, "Self-collimating phenomena in photonic crystals", Applied Physics Letter, 74, 1212 (1999).

[75] H. Kosaka, T. Kawashima, A. Tomita, M. Notomi, T. Tamamura, T. Sato, and S. Kawakami, "Superprism phenomena in photonic crystals", Phys. Rev. B **58**(16), R10096–R10099 (1998).

[76] J. B. Pendry, "Negative Refraction Makes a Perfect Lens", Phys. Rev. Lett. **85**(18), 3966–3969 (2000).

[77]. Z. Luo, Z. Tang, Y. Xiang, H. Luo, and S. Wen, "Polarization-independent low-pass spatial filters based on one-dimensional photonic crystals containing negative-index materials" Applied physics B 94, 641 (2009).

References

[78]. Evrim Colak, Atilla Ozgur Cakmak, Andriy E. Serebryannikov, and Ekmel Ozbay "Spatial filtering using dielectric photonic crystals at beam-type excitation", J. Applied Physics, 108, 113106 (2010).

[79] Z. Tang, D. Fan, S. Wen, Y. Ye, and C. Zhao, "Low-pass spatial filtering using a two-dimensional self-collimating photonic crystal, Chinese Optics Letters, Vol. 5, pp. 211, (2007).

[80] M. Campbell, D. N. Sharp, M. T. Harrison, R. G. Denning, and A. J. Turberfield, ''Fabrication of photonic crystals for the visible spectrum by holographic lithography,'' *Nature (London)* 404, 53–56, 2000.

[81] L.Grineviciute, C. Babayigit, D. Gailevičius, E. Bor, M. Turduev, V. Purlys, T. Tolenis, H. Kurt, K. Staliunas, "Angular filtering by Bragg photonic microstructures fabricated by physical vapor deposition", Applied Surface Science 481, 353–359 (2019).

[82]. L. Maigyte, T. Gertus, M. Peckus, J. Trull, C. Cojocaru, V. Sirutkaitis, and K. Staliunas, "Signatures of light-beam spatial filtering in a three-dimensional photonic crystal", Phys. Rev. A 82, 043819.

[83] V. Purlys, L. Maigyte, D. Gailevičius, M. Peckus, M. Malinauskas, and K. Staliunas, "Spatial filtering of light by chirped photonic crystals," Phys. Rev. A 87, 033805 (2013).

[84] V. Purlys, L. Maigyte, D. Gailevičius, M. Peckus, M. Malinauskas, R. Gadonas, and K. Staliunas, "Spatial filtering by axisymmetric photonic microstructures," Optics Letter, 39, 929 (2014).

[85] K. M. Davis, K. Miura, N. Sugimoto, and K. Hirao, "Writing waveguides in glass with a femtosecond laser", Optics Letters, 21, 1729 (1996).

[86] R. Panepucci, B. Kim, V. Almeida, and M. Jones, "Photonic crystals in polymers by direct electron-beam lithography presenting a photonic band gap", Journal of Vacuum Science & Technology B 22, 3348 (2004).

[87] K-H Choi, J Huh, Y. Cui, K. Trivedi, W. Hu, B-K. Ju and J-B. Lee, "One-Step Combined-Nanolithography-and-Photolithography for 2D Photonic Crystal TM Polarizer", Micromachines, 5, 228-238 (2014).

References

[88] M. Campbell, D. N. Sharp, M. T. Harrison, R. G. Denning, and A. J. Turberfield, "Fabrication of photonic crystals for the visible spectrum by holographic lithography," Nature 404, 53 (2000).

[89] M. Deubel, G. Freymann, M. Wegner, S. Pereira, K. Busch, and C. M. Soukoulis, "Direct laser writing of three-dimensional photonic-crystal templates for telecommunications," Nature 3, 444 (2004).

[90] M. Qi, E. Lidorikis, P. T. Rakich, S. G. Johnson, J. D. Joannopoulos, E.P. Ippen, and H. I. Smith, "A three-dimensional optical photonic crystal with designed point defects," Nature 429, 538 (2004).

[91] K. Busch, S. Lolkes, R. B. Wehrspohn, and H. Foll, Photonic Crystals: Advances in Design, Fabrication, and Characterization (Wiley, New York, 2006).

[92] R.W. Boyd, Nonlinear Optics, Academic Press, 2008.

[93] K. Sugiokax and Y. Cheng, "Femtosecond laser 3D Micromachining for Microfluidic and Optofluidic Applications," Springer Briefs in Applied Sciences and Technology, Springer, 2014.

[94] S. Juodkazis, V. Mizeikis and H. Misawa, "Three-dimensional microfabrication of materials by femtosecond lasers for photonics applications", *J. Appl. Phys.* 106 051101.

[95] R. Stoian, M. K. Bhuyan, G. Zhang, G. Cheng, R. Meyer, and F. Courvoisier, "Ultrafast Bessel beams: Advanced tools for laser materials processing," Adv. Opt. Technol. **7**, 165–174 (2018).

[96] J. Durnin, J. J. Miceli, and J. H. Eberly, "Diffraction-free beams", Phys. Rev. Lett. 58, 1499–1501 (1987).

[97]. A. Marcinkevicius, S. Juodkazis, S. Matsuo, V. Mizeikis, and H. Misawa, "Application of Bessel Beams for Microfabrication of Dielectrics by Femtosecond Laser," Japan. J. Appl. Phys. 40, L1197–L1199 (2001).

[98]. J. Amako, D. Sawaki, and E. Fujii, "Microstructuring transparent materials by use of non-diffracting ultrashort pulse beams generated by diffractive optics," J. Opt. Soc. Am. B, 20, 2562 (2003).

[99]. M. Mikutis, T. Kudrius, G. Šlekys, D. Paipulas, and S. Juodkazis, "High 90% efficiency Bragg gratings formed in fused silica by femtosecond Gauss-Bessel laser beams," Opt. Mater. Express, 3, 1862 (2013).

References

[100]. A. Inyushov, P. Safronova, I. Trushnikov, A. Sarkyt, and V. Shandarov, "Formation of Photonic Structures in Photorefractive Lithium Niobate by 1D and 2D Bessel-like Optical Fields," J. Phys. Conf. Ser. 867, 012023 (2017).

[101] D. Gailevičius, V. Purlys, and K. Staliunas, "Photonic crystal spatial filters fabricated by femtoseconds pulsed Bessel beam", Optics Letters, 44, 20 (2019).

[102] K. Liao, W. Wang, X. Mei, J. Cui, M. Li, and X. Li, "An analytical model to predict the sizes of modified layer in glass with femtosecond Bessel beam", Optik 185, 232–241 (2019).

[103] M. Peckus, R. Rogalskis, M. Andrulevicius, T. Tamulevicius, A. Guobiene, V. Jarutis, V. Sirutkaitis, and K. Staliunas, "Resonators with manipulated diffraction due to two- and three-dimensional intracavity photonic crystals", Physical Review A 79, 033806 (2009).

[104] C. Brée, D. Gailevicius, V. Purlys, G. G. Werner, K. Staliunas, A. Rathsfeld, G. Schmidt, M. Radziunas, "Chirped photonic crystal for spatially filtered optical feedback to a broad-area laser" Journal of Optics, 20, 9 (2018).

[105] R. Lang and K. Kobayashi. External optical feedback effects on semiconductor injection laser properties. IEEE J. of Quantum Electronics, 16:347–355, 1980.

[106]. G. P. Agrawal, "Fast-Fourier-transform based beam-propagation model for stripe-geometry semiconductor lasers: Inclusion of axial effects," J. Appl. Phys. 56, 3100 (1984).

[107] E. A. Ultanir, D. Michaelis, F. Lederer, and G. I. Stegeman, "Stable spatial solitons in semiconductor optical amplifiers", Optics Letter 28, 251 (2003).

[108]. M. Radziunas, J. Fuhrmann, A. Zeghuzi, H.J. Wünsche, T. Koprucki, C. Brée, H. Wenzel & U. Bandelow, "Efficient coupling of dynamic electro-optical and heat-transport models for high-power broad-area semiconductor lasers", *Optical and Quantum Electronics*, *51*(3), 69 (2019).

[109]. J. Medina, R. Herrero, M. Botey, K. Staliunas, "Stabilized narrow-beam emission from broad-area semiconductor lasers", Phys. Rev. A 101 (033833) 2020

[110]. J.M. Buldú , F. Rogister , J. Trull , C. Serrat , M.C. Torrent , Claudio R. Mirasso and J. Garcia-Ojalvo, "Dynamics of power distribution in multimode semiconductor lasers with optical feedback", Proc. SPIE, 4646, Physics and Simulation of Optoelectronic Devices X, (2002).

[111] A. E. Siegmann, G. Nemes, and J. Serna, "How to (Maybe) Measure Laser Beam Quality," in *DPSS (Diode Pumped Solid State) Lasers: Applications and Issues*. Optical Society of America, 1998.

[112] A. E. Siegmann, M. W. Sasnett, and T. F. Johnston, Jr., "Choice of Clip Levels for Beam Width Measurements Using Knife-Edge Techniques", IEEE Journal of Quantum Electronics, 21, 4, April 1991.

[113] Y. Champagne: Second-Moment Approach to the Time-Averaged Spatial Characterization of Multiple-Transverse-Mode Laser Beams, J. Opt. Soc. Am. A, 12, 1707–1714 (1995).

[114] N. Reng and B. Eppich, "Definition and measurements of high power laser beam parameters", Optical and Quantum Electronics, vol. 24, pp. 973–992, 1992.

[115] Thomas F. Johnston, "Beam propagation M^2 measurement made as easy as it gets: the four-cuts method", Applied Optics, 37 (21), 1998.

[116] G. Arisholm, R. Paschotta, and T. Südmeyer, "Limits to the power scalability of high-gain optical parametric oscillators and amplifiers", J. Opt. Soc. Am. B 21 (3), 578 (2004).

[117] P. P. Mondal and A. Diaspro, Fundamentals of Fluorescence Microscopy: Exploring Life with Light, Springer, New York, 2014.

[118] D. Gailevicius, V. Koliadenko, V. Purlys, M. Peckus, V. Taranenko, K. Staliunas, Photonic Crystal Microchip Laser, Scientific. Report. 6, 34173 (2016).

[119] O. Hess, S. W. Koch, and J. V. Moloney, "Filamentation and beam propagation in broad-area semiconductor lasers", IEEE J. Quantum Electron, 31, 35–43 (1995).

[120] J. R. Marciante, and G. P. Agrawal, "Nonlinear mechanism of filamentation in broad area semiconductor lasers", IEEE J. Quantum Electron, 32, 590–596 (1996).

[121] O. Hess, and T. Kuhn, "Spatio-temporal dynamics of semiconductor lasers: Theory, modeling and analysis", Progress in Quantum Electronics, 20, 85–179 (1996).

[122] B. Leonhäuser, H. Kissel, A. Unger, B. Köhler, J. Biesenbach, "Feedback-induced catastrophic optical mirror damage (COMD) on 976nm broad area single emitters with different AR reflectivity", Proc. SPIE 8965, 896506 (2014).

[123] C. Holly, S. Hengesbach, M. Traub, and D. Hoffmann, "Simulation of spectral stabilization of high-power broad-area edge emitting semi-conductor lasers," Opt. Express, 21, 15553–15567 (2013).

[124] S. Gawali, J. Medina, D. Gailevicius, V. Purlys, G. Garre-Werner, C. Cojocaru, J. Trull, M. Botey, R. Herrero, J. Montiel-Ponsoda, and K. Staliunas, "Spatial filtering in edge-emitting lasers by intracavity chirped photonic crystals", JOSA B, 37,10 (2020)

References

[125] V. Gapontsev, N. Mozhegov, P. Trubenko, A. Komissarov, I. Berishev, O. Raisky, N. Strouglov, V. Chuyanov, G. Kuang, O. Maksimov, A. Ovtchinnikov, “High-brightness fiber coupled pumps”. Proc. SPIE 7198, 719800 (1–9) (2009).

Publications

Journal articles

1) **S. Gawali**, D. Gailevičius, G. Garre-Werner, V. Purlys, C. Cojocaru, J. Trull, J. Montiel-Ponsoda, and K. Staliunas, "Photonic crystal spatial filtering in broad aperture diode laser", Applied Physics Letter 115, 141104 (2019).

2) **S. Gawali**, J. Medina, D. Gailevičius, V. Purlys, G. Garre-Werner, C. Cojocaru, J. Trull, M. Botey, R. Herrero, J. Montiel-Ponsoda, and K. Staliunas, "Spatial Filtering in Edge Emitting Lasers by Intracavity Chirped Photonic Crystals", Journal of America Society of America B, 37, 10 (2020)

Conference proceeding

1) **S.Gawali**, D. Gailevičius, V. Purlys, C. Cojocaru, J. Trull and K. Staliunas, "Spatial filtering in broad area semiconductor laser using photonic crystal", SPIE Photonics Europe 2020, Proc. of SPIE Vol. 11356 113560R1.

Appendix

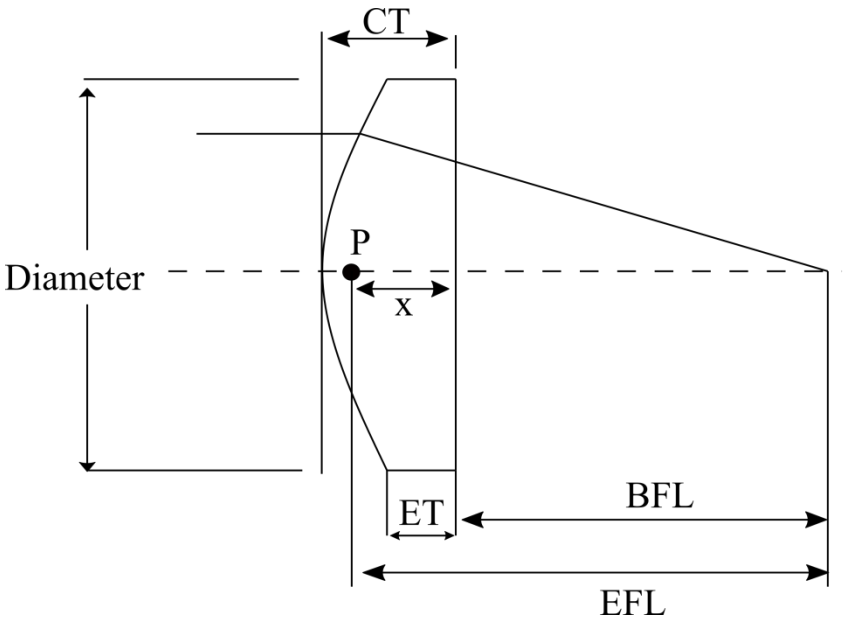

The focal length of lens can be calculated using following equation:

$$f = R/(n-1)$$

Where n is the refractive index and R is the radius of curvature.

At 970 nm, the refractive index is 1.5079 for N-Bk7 glass. The radius of curvature of the lens is 26.4 mm. From above formula, the calculated focal length will be 51.97 mm.